UNIVERSITÀ DEGLI STUDI ROMA TRE
Facoltà di scienze Matematiche, Fisiche e Naturali
Dipartimento di Matematica e Fisica

Doctoral School in Physics (XXIX Cycle)

Theoretical description and reconstruction of neutrino interactions, and systematic uncertainties of long-baseline oscillation experiments

Candidate:

Erica Vagnoni

Thesis advisors:

Dr. Davide Meloni
Prof. Omar Benhar

Coordinator:

Prof. Roberto Raimondi

Thesis submitted in 2016

Thesis not yet defended.

Ai miei genitori

L'intima natura delle cose
ama nascondersi.

Eraclito

Contents

Introduction **1**

1 Neutrino physics **5**
1.1 Neutrino mass and mixing 6
1.2 Neutrino oscillations 8
1.3 Experimental status 13

2 Neutrino-nucleon interactions **17**
2.1 Cross Section formalism 17
2.2 Quasi-elastic channel 21
2.3 Resonance production 23
2.4 Deep inelastic scattering 26

3 Neutrino-nucleus interactions **35**
3.1 The Impulse Approximation 35
3.2 The Spectral Function 39
3.3 Neutrino-Carbon cross section 44

4 Neutrino energy reconstruction **49**
4.1 Reconstruction methods 50
4.2 Event generation 52
4.3 Considered detector effects 54
4.4 Migration matrices 55

5 Oscillation analysis **61**
5.1 Impact of detector effects in disappearance experiments 62
5.2 Impact of missing energy on the extraction of the CP-violating phase 67
5.3 Impact of $2p2h$ uncertainties 70

Conclusions **77**

Acknowledgments **81**

Appendices **83**
A Notation 83
B Leptonic Tensor 85

C Structure Functions for the Δ-resonance 87
D Kinematic formulas 89
E Migration Matrices 91
F χ^2 analysis 95
G Gaussian smearing 97

Bibliography **101**

Introduction

In the course of the last two decades, neutrino oscillations have been firmly established, and their studies are now entering the era of precision. Neutrino experiments are based on the observation of neutrino-nucleus interactions, but neutrino event rates strongly depend, in a non trivial way, on the largely unknown neutrino energy. Because neutrinos are neutral particles, their energy needs to be reconstructed from the observation of the charged final states produced during the interactions. Furthermore, neutrino cross sections are very small, of the order of 10^{-38} cm^2 for energies around 1 GeV. Therefore, to increase neutrino event rate, huge detectors consisting of nuclear targets must be used, and the problem arises of understanding the nuclear response to weak interactions. The study of neutrino interactions has always been an important topic [1], however in modern oscillation experiments a high level of accuracy is required, and cross section uncertainty is widely acknowledged as one of the major sources of systematic errors. For this reason, there have been many efforts over the years to understand neutrino-nucleus interactions, see for instance Refs. [2, 3] as recent reviews.

In this Thesis we analyze charged-current neutrino-nucleus interactions in all three interaction channels which are relevant for neutrino energies between few hundreds MeV and few GeV: quasi-elastic scattering, resonance production and deep inelastic scattering. The unified treatment of the nuclear response that we have used is based on the *Impulse Approximation*. This scheme can be applied when the momentum transferred $\mathbf{q}$ is such that the spatial resolution of the probe, $\lambda \sim 1/|\mathbf{q}|$, is smaller than the average distance between nucleons. Under these conditions, it is possible to consider the interaction of the probe with a single nucleon, while the residual system acts as a "spectator". The neutrino-nucleus cross section can then be expressed as the incoherent sum of the elementary processes off *bound* and *moving* nucleons. The main advantage of this approximation is the possibility to consider the particles produced at the interaction vertex and the residual system as two systems evolving independently of one another. In such formalism, the nuclear dynamics is incorporated in the spectral function, trivially related to the imaginary part of the two-point Green's function. It describes the probability of removing a nucleon from the nuclear target, leaving the residual system with a given excitation energy.

The use of a realistic description of nuclear dynamics is a fundamental ingredient of modern neutrino event generators. To have most sensitive results, neutrino experiments rely on Monte Carlo event generators to compare the observed signal to the predicted one. However, generators are dependent on the underlying nuclear physics. For example, the charged-current quasi-elastic interaction was considered theoretically well understood in terms of single-nucleon knock-out, but very recent results have shown that processes involving more than one nucleon excited to the continuum play a non-negligible role, at the

required level of accuracy.

At energies where quasi-elastic scattering dominates, the energy distribution of charged-current events can be experimentally determined from the kinematics of the outgoing charged lepton, as measured by large Cherenkov detectors filled with water or mineral oil. This kinematic reconstruction applies to quasi-elastic events, identified by the absence of pions in the final state. However, if a pion is produced and absorbed in the nuclear medium, or if it escapes detection, the event is erroneously reconstructed as quasi-elastic.

Assuming that the physics model in the event generator provides an accurate description of the underlying physics, the reconstruction of the neutrino flux is also subject to the assumed detector capabilities. Their correct estimation represents another source of systematic uncertainty that needs to be kept under control. Furthermore, in order to provide a more precise reconstruction, calorimeters measuring the energy deposited by the final-state particles have been proposed, as an alternative to Cherenkov detectors for ongoing and future experiments. The calorimetric technique thus rests on the ability of fully reconstructing the final state, which largely depends on the detector design and performance. Nuclear effects also play a role, as they may lead to a sizable amount of missing energy, hindering the reconstruction of neutrino energy.

The Thesis deals with the above issues in the following way.

Chapter 1 briefly outlines the physics of neutrino masses and mixings. Non vanishing neutrino masses entail a description of flavor eigenstates as a linear combination of mass eigenstates. This misalignment implies neutrino oscillations between different flavors, unambiguously and extensively confirmed by experiments. We review the current mass-mixing phenomenology and the prospects for both precision and discovery physics, including e.g. CP violation in the neutrino sector.

To achieve accurate measurements in neutrino oscillation searches, it is important to reduce systematic uncertainties, related to neutrino interactions. In this light, Chapter 2 is devoted to the discussion of the elementary neutrino-nucleon cross section in the quasi-elastic, resonance production and deep inelastic sectors, which is a prerequisite for the study of the neutrino-nucleus interactions.

In Chapter 3 we derive the cross section for scattering processes off nuclei within the impulse approximation scheme, which is based on the *Spectral Function* formalism. We report the results obtained for the double differential cross section, the Q^2-distribution and total cross section of ν_μ-carbon scattering computed within this approach. The main achievement consists in the evaluation of the cross section in the regions of resonance production and deep inelastic scattering, carried out for a wide range of neutrino energies (up to 20 GeV)[1].

The second half of the Thesis (Chapters 4 and 5) contains original work that has led to

[1] E. Vagnoni, O. Benhar and D. Meloni. *Inelastic Neutrino-Nucleus Interactions within the Spectral Function Formalism.* `arXiv:1701.01718` (2017). Submitted to Physical Review Letters.

publications[2,3,4]. Besides neutrino cross section systematics, we analyze the problem of neutrino energy reconstruction from the produced final state with high accuracy, which is a formidable experimental task. In Chapter 4, we consider two different approaches for the energy reconstruction, one based on the calorimetric method and the other on the reconstruction of the lepton kinematics. The simulated energy reconstruction of neutrino events, which are generated with a state-of-the-art Monte Carlo, allowed us to produce migration matrices, describing the probability that the reconstructed energy is different from the true one.

Chapter 5 is devoted to three phenomenological studies of the extraction of the oscillation parameters in long-baseline experiments. In the first analysis, we discuss the effects of neutrino energy reconstruction techniques on the evaluation of the mass-mixing parameters in the $\nu_\mu \to \nu_\mu$ disappearance channel[2]. In the second analysis, we investigate the level of accuracy required in the evaluation of the so-called missing energy, to avoid sizable bias in the determination of the CP-violating phase[3]. Finally, we analyze the impact of the model used to describe multi-nucleon mechanisms in a disappearance experiment[4].

We conclude the Thesis by summarizing the main findings and the prospects for future work.

[2] A. Ankowski, O. Benhar, P. Coloma, P. Huber, C.-M. Jen, C. Mariani, D. Meloni and E. Vagnoni. *Comparison of the calorimetric and kinematic methods of neutrino energy reconstruction in disappearance experiments.* Phys. Rev. D **92**, 073014 (2015).

[3] A. Ankowski, P. Coloma, P. Huber, C. Mariani and E. Vagnoni. *Missing energy and the measurement of the CP-violating phase in neutrino oscillations.* Phys. Rev. D **92**, 091301 (2015).

[4] A. Ankowski, O. Benhar, C. Mariani and E. Vagnoni. *Effect of the* $2p2h$ *cross-section uncertainties on an analysis of neutrino oscillations.* Phys. Rev. D **93**, 113004 (2016).

Chapter 1

Neutrino physics

In this Chapter we will introduce general aspects of neutrino physics, summarizing what is known from experiments.
In the Standard Model (SM) of particle physics, electroweak interactions are described by the local symmetry group $SU(2)_L \times U(1)_Y$, where L and Y denote the left-handed chirality and the hypercharge, respectively. The considered gauge group uniquely defines the interactions and the number of vector gauge bosons. The gauge group is broken down to $U(1)_{em}$ through a non-zero vacuum-expectation-value of the Higgs doublet. After the electroweak symmetry breaking there are three massive gauge bosons ($W^{\pm}$ and Z) and a massless gauge boson (γ), see e.g. the textbooks [4, 5, 6, 7].
In the SM, fermions can be accommodated in appropriate representations of the symmetry group and they are divided in two different categories, quarks and leptons. The leptonic sector is defined by three neutrinos existing in three different flavors ν_e, ν_μ and ν_τ, belonging to the isospin doublet with defined chirality (*left-handed*, LH) together with the corresponding charged leptons e, μ and τ. The six quarks are accommodated in the three generations as (u, d), (c, s) and (t, b), with their left-handed chiral components as well. The *right-handed* (RH) components of the fermions are assumed to be singlets under the weak isospin group.
The Lagrangian describing electroweak interactions in the SM is (see, e.g., Ref. [4])

$$\mathscr{L}_{\text{int}} = eJ^{\mu}_{em}A_{\mu} - \frac{g}{2\sqrt{2}}(J^{\mu}_{\text{CC}}W^{\dagger}_{\mu} + \text{h.c.}) - \frac{g}{2\cos\theta_W}J^{\mu}_{\text{NC}}Z_{\mu} \ , \tag{1.1}$$

and it is defined in terms of three different kinds of currents: the electromagnetic current J^{μ}_{em}, the weak charged current J^{μ}_{CC} and the weak neutral current J^{μ}_{NC}, respectively coupled to the photon field A_μ, to the charged bosons fields W and to the neutral boson field Z. The currents for the first generation of leptons and quarks are given by

$$J^{\mu}_{em} = -\,\overline{e}\gamma^{\mu}e + \frac{2}{3}\overline{u}\gamma^{\mu}u - \frac{1}{3}\overline{d}\gamma^{\mu}d \ , \tag{1.2}$$

$$J^{\mu}_{CC} = \overline{\nu}_e\gamma^{\mu}(1-\gamma_5)e + \overline{u}\gamma^{\mu}(1-\gamma_5)d \ , \tag{1.3}$$

$$J^{\mu}_{NC} = \overline{\nu}_e\gamma^{\mu}(1-\gamma_5)\overline{\nu}_e - \overline{e}\gamma^{\mu}(1-\gamma_5)e + \overline{u}\gamma^{\mu}(1-\gamma_5)u - \overline{d}\gamma^{\mu}(1-\gamma_5)d - 2\sin\theta_W J^{\mu}_{em} \ . \tag{1.4}$$

In the SM neutrinos are supposed to be massless, but experimental evidence from oscillation experiments tells us that neutrinos have a mass, orders of magnitude smaller than the

electron mass. The most stringent upper bounds on neutrino masses are set by ^{3}H β-decay experiments, at the level of $\sim$2 eV [8].

1.1 Neutrino mass and mixing

Massive neutrino can be accommodated in the SM, considering neutrino as a *Dirac* or *Majorana* particle, but we limit ourselves to the first case only; see e.g. Refs. [9, 10].
Dirac neutrino masses can be generated by the same Higgs mechanism that gives masses to quarks and charged leptons in the SM. A minimal extension of the SM is needed, by introducing right-handed neutrino components, ν_R. Right-handed neutrinos are also called *sterile*, because they do not participate in weak interactions, being singlets.
The introduction of three right-handed neutrinos and of Yukawa couplings between neutrinos and the Higgs field leads to a Lagrangian mass term in the leptonic sector which, after spontaneous symmetry breaking, is

$$\mathscr{L}_{mass} = -\frac{v}{\sqrt{2}} \sum_{\alpha,\beta=e,\mu,\tau} (\overline{\nu}_{\alpha L} Y^{\nu}_{\alpha\beta} \nu_{\beta R} + \text{h.c.}) - \frac{v}{\sqrt{2}} \sum_{\alpha,\beta=e,\mu,\tau} (\overline{\ell}_{\alpha L} Y^{\ell}_{\alpha\beta} \ell_{\beta R} + \text{h.c.}) \ , \tag{1.5}$$

where ℓ_α represents the charged lepton fields, v is the vacuum expectation value of the Higgs field and Y^ν and Y^ℓ are the Yukawa couplings for neutrinos and charged leptons, respectively accommodated in 3×3 matrices. Chiral states are introduced via chiral projectors $\mathscr{P}_{L,R}$ as

$$\nu_L = \mathscr{P}_L \nu = \frac{1-\gamma_5}{2}\nu \ , \quad \nu_R = \mathscr{P}_R \nu = \frac{1+\gamma_5}{2}\nu \ . \tag{1.6}$$

In general, the $Y^{\nu,\ell}$ matrices need to be diagonalized to find the mass eigenstates. The diagonalization can be performed with a biunitary transformation, namely

$$U_L^{\nu\dagger} Y^\nu U_R^\nu = Y'^\nu \quad \text{with} \quad Y'^\nu_{ij} = y'^\nu_i \delta_{ij} \ , \tag{1.7}$$

$$U_L^{\ell\,\dagger} Y^\ell U_R^\ell = Y'^\ell \quad \text{with} \quad Y'^\ell_{\alpha\beta} = y'^\ell_\alpha \delta_{\alpha\beta} \ . \tag{1.8}$$

This allows to define the LH and RH components of the fields with definite mass as

$$\nu_{kL} = \sum_{\beta=e,\mu,\tau} (U_L^{\nu\dagger})_{k\beta} \nu_{\beta L} \ , \quad \nu_{kR} = \sum_{\beta=e,\mu,\tau} (U_R^{\nu\dagger})_{k\beta} \nu_{\beta R} \ , \tag{1.9}$$

$$\ell'_{\alpha L} = \sum_{\beta=e,\mu,\tau} (U_L^{\ell\,\dagger})_{\alpha\beta} \ell_{\beta L} \ , \quad \ell'_{\alpha R} = \sum_{\beta=e,\mu,\tau} (U_R^{\ell\,\dagger})_{\alpha\beta} \ell_{\beta R} \ , \tag{1.10}$$

leading to the mass term

$$\mathscr{L}_{mass} = -\sum_{k=1,2,3} \frac{v y'^\nu_k}{\sqrt{2}} (\overline{\nu}_{kL}\nu_{kR} + \text{h.c.}) - \sum_{\alpha=e,\mu,\tau} \frac{v y'^\ell_\alpha}{\sqrt{2}} (\overline{\ell}'_{\alpha L}\ell'_{\alpha R} + \text{h.c.}) = \tag{1.11}$$

$$= -\sum_{k=1,2,3} \frac{v y'^\nu_k}{\sqrt{2}} \overline{\nu}_k \nu_k - \sum_{\alpha=e,\mu,\tau} \frac{v y'^\ell_\alpha}{\sqrt{2}} \overline{\ell}'_\alpha \ell'_\alpha \ , \tag{1.12}$$

with

$$\nu_k = \nu_{kL} + \nu_{kR} \ , \tag{1.13}$$
$$\ell'_\alpha = \ell'_{\alpha L} + \ell'_{\alpha R} \ . \tag{1.14}$$

The mixing has important consequences in neutrino interactions. From Eq. (1.3), the leptonic charged current interaction can be written in terms of mass eigenstates

$$J^\mu_{CC} = \sum_{k=1,2,3} \sum_{\alpha=e,\mu,\tau} \overline{\nu}_{kL} \gamma^\mu (U_L^{\nu\dagger} U_L^\ell)_{k\alpha} \ell'_{\alpha L} \ , \tag{1.15}$$

where the matrix

$$\mathbf{U} = U_L^{\ell\,\dagger} U_L^\nu \ , \tag{1.16}$$

is also known as Pontecorvo-Maki-Nakagawa-Sakata (PMNS) matrix. It is conventional to define the left-handed neutrino fields in flavor space as

$$\nu_{\alpha L} = \sum_k \mathbf{U}_{\alpha k} \nu_{kL} \ , \tag{1.17}$$

expressing the mixing between neutrino flavor and mass fields.
The unitary mixing matrix $\mathbf{U}$, can be parametrized in terms of three mixing angles and one phase[1]. A useful and generally adopted parametrization, similar to that used for the CKM (Cabibbo-Kobayashi-Maskawa) matrix, is given by [9, 10]

$$\mathbf{U} = \begin{pmatrix} c_{12}c_{13} & s_{12}c_{13} & s_{13}e^{-i\delta} \\ -s_{12}c_{23} - c_{12}s_{23}s_{13}e^{i\delta} & c_{12}c_{23} - s_{12}s_{23}s_{13}e^{i\delta} & s_{23}c_{13} \\ s_{12}s_{23} - c_{12}c_{23}s_{13}e^{i\delta} & -c_{12}s_{23} - s_{12}c_{23}s_{13}e^{i\delta} & c_{23}c_{13} \end{pmatrix} \tag{1.18}$$

where $c_{ij} = \cos(\theta_{ij})$ and $s_{ij} = \sin(\theta_{ij})$, with θ_{ij} the mixing angles ($0 \leq \theta_{ij} \leq \pi/2$). δ is the Dirac CP-violating phase ($0 \leq \delta < 2\pi$).

As a final remark, it is important to mention that it is possible to introduce also Majorana neutrino mass terms [11]. In this case the right-handed neutrino state is identified with the left-handed antineutrino state, and the mixing is realized with the same matrix as in Eq. (1.18), multiplied by an additional diagonal matrix on the right hand side, U^M, given by

$$U^M = \begin{pmatrix} 1 & 0 & 0 \\ 0 & e^{i\lambda_{21}} & 0 \\ 0 & 0 & e^{i\lambda_{31}} \end{pmatrix} \tag{1.19}$$

where λ_{21} and λ_{31} are the so-called Majorana CP-violating phases [9, 10].

[1] In the general case of unitary matrix $N \times N$, the number of independent parameters are

$$\frac{1}{2}N(N-1) \quad \text{angles} \ ,$$

$$\frac{1}{2}(N-1)(N-2) \quad \text{phases} \ .$$

1.2 Neutrino oscillations

The phenomenon of neutrino flavor oscillations appears because of the misalignment of the flavor and mass eigenstates. The field operator $\overline{\nu}_{kL}$, appearing in the leptonic charged current in Eq. (1.15), contains the creation operators of neutrino states with definite masses m_k, with weights given by $\mathbf{U}^*_{\alpha k}$. Thus, the relation between mass and interaction eigenstates is realized by [9]

$$|\nu_\alpha\rangle = \sum_{k=1}^{3} \mathbf{U}^*_{\alpha k} |\nu_k\rangle \ , \qquad \alpha = e, \mu, \tau \ . \tag{1.20}$$

Massive neutrinos are the eigenstates of the free Hamiltonian

$$\mathscr{H}|\nu_k\rangle = E_k|\nu_k\rangle \ , \tag{1.21}$$

where the energy eigenvalues are given by $E_k = \sqrt{|\mathbf{p}|^2 + m_k^2}$. From the Schrödinger equation

$$i\frac{\mathrm{d}}{\mathrm{d}t}|\nu_k(t)\rangle = \mathscr{H}|\nu_k(t)\rangle \ , \tag{1.22}$$

we can consider the evolution of the state as a plane wave, according to

$$|\nu_k(t)\rangle = e^{-iE_k t}|\nu_k\rangle \ , \tag{1.23}$$

that applied to Eq. (1.20), gives the relation for the time evolution of flavor states

$$|\nu_\alpha(t)\rangle = \sum_k \mathbf{U}^*_{\alpha k} e^{-iE_k t}|\nu_k\rangle \ , \tag{1.24}$$

where E_k is the energy of the massive neutrino and $|\nu_\alpha\rangle$ is such that $|\nu_\alpha(t=0)\rangle = |\nu_\alpha\rangle$. Using Eq. (1.20) to express the mass eigenstate as a combination of flavor eigenstates, Eq. (1.24) becomes

$$|\nu_\alpha(t)\rangle = \sum_{\beta=e,\mu,\tau} \sum_k \mathbf{U}^*_{\alpha k} e^{-iE_k t} \mathbf{U}_{\beta k} |\nu_\beta\rangle \ . \tag{1.25}$$

From the previous equation we can see that the state with defined flavor at $t = 0$, becomes a superposition of different flavor states at a time t, due to the neutrino mixing described by the non diagonal matrix $\mathbf{U}$.
The amplitude of the transition process, from a state ν_α to a state ν_β, is given by

$$A_{\nu_\alpha \to \nu_\beta}(t) \equiv \langle \nu_\beta | \nu_\alpha(t)\rangle = \sum_k \mathbf{U}^*_{\alpha k} \mathbf{U}_{\beta k} e^{-iE_k t} \ , \tag{1.26}$$

from which we can evaluate the transition probability

$$P_{\nu_\alpha \to \nu_\beta}(t) = \left| A_{\nu_\alpha \to \nu_\beta}(t) \right|^2 = \sum_{k,j} \mathbf{U}^*_{\alpha k} \mathbf{U}_{\beta k} \mathbf{U}_{\alpha j} \mathbf{U}^*_{\beta j} e^{-i(E_k - E_j)t} \ . \tag{1.27}$$

For ultra-relativistic neutrinos, the energy eigenvalues E_k can be written as[2]

$$E_k \simeq |\mathbf{p}| + \frac{m_k^2}{2|\mathbf{p}|} \ . \tag{1.28}$$

In such a limit we have

$$E_k - E_j \simeq \frac{\Delta m_{kj}^2}{2E} \ , \tag{1.29}$$

where we used $E \simeq |\mathbf{p}|$ and $\Delta m_{kj}^2 \equiv m_k^2 - m_j^2$ is the squared mass difference.
Thus the oscillation probability can be written as

$$P_{\nu_\alpha \to \nu_\beta}(t, E) = \sum_{k,j} \mathbf{U}_{\alpha k}^* \mathbf{U}_{\beta k} \mathbf{U}_{\alpha j} \mathbf{U}_{\beta j}^* \exp\left(- i \frac{\Delta m_{kj}^2 t}{2E} \right) . \tag{1.30}$$

In neutrino oscillation experiments, the known quantity is the distance, L, travelled by neutrinos from the source to the interaction point. For ultra-relativistic neutrinos we can consider the approximation $t = L$, thus

$$P_{\nu_\alpha \to \nu_\beta}(L, E) = \sum_{k,j} \mathbf{U}_{\alpha k}^* \mathbf{U}_{\beta k} \mathbf{U}_{\alpha j} \mathbf{U}_{\beta j}^* \exp\left(- i \frac{\Delta m_{kj}^2 L}{2E} \right) . \tag{1.31}$$

The oscillation probabilities for $\alpha \neq \beta$ (flavor appearance channel) are usually called *transition probabilities*, whereas the oscillation probabilities for $\alpha = \beta$ (flavor disappearance channel) are usually called *survival probabilities*. In the disappearance channel we have

$$P_{\nu_\alpha \to \nu_\alpha}(L, E) = 1 - 4 \sum_{k>j} |\mathbf{U}_{\alpha k}|^2 |\mathbf{U}_{\alpha j}|^2 \sin^2 \left(\frac{\Delta m_{kj}^2 L}{4E} \right) . \tag{1.32}$$

For antineutrinos, the oscillation probability has the same structure, but with the replacement $\mathbf{U} \to \mathbf{U}^*$.
From Eq. (1.31) it is possible to notice that the oscillation phase depends on the neutrino energy, on the distance travelled by the neutrino, and on the squared mass difference. Furthermore, the oscillation depends on the parameters defining the mixing matrix, through the product

$$\mathbf{U}_{\alpha k}^* \mathbf{U}_{\beta k} \mathbf{U}_{\alpha j} \mathbf{U}_{\beta j}^* \ , \tag{1.33}$$

which is invariant for phase transformations, such as

$$\mathbf{U}_{\alpha k} \longrightarrow e^{i\psi_\alpha} \mathbf{U}_{\alpha k} e^{i\phi_k} \ . \tag{1.34}$$

In the case of Majorana neutrinos

$$\mathbf{U}_{\alpha k} = U_{\alpha k}^D e^{i\lambda_k} \ , \tag{1.35}$$

[2]It is possible to write the neutrino energy as

$$E_k = \sqrt{|\mathbf{p}|^2 + m_k^2} = |\mathbf{p}| \sqrt{\left(1 + \frac{m_k^2}{|\mathbf{p}|^2}\right)} \simeq |\mathbf{p}| \left(1 + \frac{m_k^2}{2|\mathbf{p}|^2}\right) ,$$

having considered the first order expansion in the small ratio $(m_k/|\mathbf{p}|)^2$.

and Eq. (1.33) shows that oscillation probabilities are independent on the Majorana phases, which can thus be neglected.
From the unitarity of $\mathbf{U}$, the oscillation probabilities satisfy the following relations

$$\sum_{\beta} P_{\nu_\alpha \to \nu_\beta}(L,E) = 1 \ , \tag{1.36}$$

$$\sum_{\alpha} P_{\nu_\alpha \to \nu_\beta}(L,E) = 1 \ . \tag{1.37}$$

It is useful to rewrite the oscillation probability in Eq. (1.31) splitting the real and the imaginary part, such as [9]

$$\begin{aligned} P_{\nu_\alpha \to \nu_\beta}(L,E) =& \delta_{\alpha\beta} - 4 \sum_{k>j} \mathrm{Re}[\mathbf{U}^*_{\alpha k}\mathbf{U}_{\beta k}\mathbf{U}_{\alpha j}\mathbf{U}^*_{\beta j}] \sin^2\left(\frac{\Delta m^2_{kj} L}{4E}\right) + \\ & + 2 \sum_{k>j} \mathrm{Im}[\mathbf{U}^*_{\alpha k}\mathbf{U}_{\beta k}\mathbf{U}_{\alpha j}\mathbf{U}^*_{\beta j}] \sin\left(\frac{\Delta m^2_{kj} L}{2E}\right) \ , \end{aligned} \tag{1.38}$$

and for antineutrinos

$$\begin{aligned} P_{\overline{\nu}_\alpha \to \overline{\nu}_\beta}(L,E) =& \delta_{\alpha\beta} - 4 \sum_{k>j} \mathrm{Re}[\mathbf{U}^*_{\alpha k}\mathbf{U}_{\beta k}\mathbf{U}_{\alpha j}\mathbf{U}^*_{\beta j}] \sin^2\left(\frac{\Delta m^2_{kj} L}{4E}\right) + \\ & - 2 \sum_{k>j} \mathrm{Im}[\mathbf{U}^*_{\alpha k}\mathbf{U}_{\beta k}\mathbf{U}_{\alpha j}\mathbf{U}^*_{\beta j}] \sin\left(\frac{\Delta m^2_{kj} L}{2E}\right) \ , \end{aligned} \tag{1.39}$$

thus Eqs. (1.38) and (1.39) differ for the sign of the imaginary (CP-violating) part. The CP-conserving part, $P^{CP}_{\nu_\alpha \to \nu_\beta}(L,E)$, is then given by

$$P^{CP}_{\nu_\alpha \to \nu_\beta}(L,E) = P^{CP}_{\overline{\nu}_\alpha \to \overline{\nu}_\beta}(L,E) = \delta_{\alpha\beta} - 4 \sum_{k>j} \mathrm{Re}[\mathbf{U}^*_{\alpha k}\mathbf{U}_{\beta k}\mathbf{U}_{\alpha j}\mathbf{U}^*_{\beta j}] \sin^2\left(\frac{\Delta m^2_{kj} L}{4E}\right) \ , \tag{1.40}$$

whereas the CP-violating terms, $P^{\not{CP}}_{\nu_\alpha \to \nu_\beta}(L,E)$, are

$$P^{\not{CP}}_{\nu_\alpha \to \nu_\beta}(L,E) = -P^{\not{CP}}_{\overline{\nu}_\alpha \to \overline{\nu}_\beta}(L,E) = 2 \sum_{k>j} \mathrm{Im}[\mathbf{U}^*_{\alpha k}\mathbf{U}_{\beta k}\mathbf{U}_{\alpha j}\mathbf{U}^*_{\beta j}] \sin\left(\frac{\Delta m^2_{kj} L}{2E}\right) \ . \tag{1.41}$$

In principle, CP violation in neutrino oscillations can be studied by looking at neutrino-antineutrino asymmetries

$$A^{CP}_{\alpha\beta} \equiv P_{\nu_\alpha \to \nu_\beta}(L,E) - P_{\overline{\nu}_\alpha \to \overline{\nu}_\beta}(L,E) = 4 \sum_{k>j} \mathrm{Im}[\mathbf{U}^*_{\alpha k}\mathbf{U}_{\beta k}\mathbf{U}_{\alpha j}\mathbf{U}^*_{\beta j}] \sin\left(\frac{\Delta m^2_{kj} L}{2E}\right) \ , \tag{1.42}$$

which are nonzero only for $\alpha \neq \beta$ (appearance channels).

The CP-violating term introduced above is proportional to the Jarlskog invariant J [12] which, in the standard parameterization of Eq. (1.18), is given by

$$J = \frac{1}{8} \sin 2\theta_{12} \sin 2\theta_{23} \sin 2\theta_{13} \cos\theta_{13} \sin\delta \ . \tag{1.43}$$

Thus the general conditions for non-vanishing CP violation are: $\theta_{ij} \neq 0, \pi/2$ and $\delta \neq 0, \pi$ (and obviously $\Delta m^2_{kj} \neq 0$).
So far we have only considered oscillations in vacuum. In order to introduce matter effects, we briefly consider a simpler scenario with only two flavor states ν_α and ν_β, mixed with two massive fields ν_1 and ν_2 via a matrix

$$\mathbf{U} = \begin{pmatrix} \cos\theta & \sin\theta \\ -\sin\theta & \cos\theta \end{pmatrix} \ . \tag{1.44}$$

The oscillation probability assumes then a simple form

$$P_{\nu_\alpha \to \nu_\beta}(L, E) = \sin^2(2\theta) \sin^2\left(\frac{\Delta m^2 L}{4E}\right) \ . \tag{1.45}$$

The previous picture is modified if neutrinos propagate in matter due to coherent forward scattering on electrons and nucleons [13, 14]. In fact only electron neutrinos interact with electrons in the medium in the charged current (CC) channel, and they feel an interaction potential given by

$$V_{CC} = \sqrt{2} G_F n_e \ , \tag{1.46}$$

where G_F is the Fermi constant, and n_e is the electron number density. Muon and tau neutrinos do not experience such CC forward scattering effect, since charged muons and taus are not present in ordinary matter. On the other hand, neutrinos of all flavors can interact in the neutral current (NC) channel with neutrons, protons, and electrons. The net NC contribution is due to neutrons, since the electron and proton contributions cancel each other. The total NC effective potential is

$$V_{NC} = \frac{\sqrt{2}}{2} G_F n_n \ , \tag{1.47}$$

where n_n is the number density of neutrons. The signs of Eqs. (1.46) and (1.47) are the opposite if antineutrinos are considered. Thus, the effective matter potential to be added to the vacuum hamiltonian, can be written as [9]

$$V_\alpha = V_{CC} \delta_{\alpha e} + V_{NC} \ . \tag{1.48}$$

Notice that the common term due to NC interactions appears as a diagonal entry proportional to the identity in the hamiltonian, and therefore it does not contribute to the flavor state evolution.
In the simplest case of the two-neutrino mixing traveling through matter with constant density, the presence of the effective potential leads to an effective mixing angle given by [13, 14]

$$\tan 2\theta_M = \frac{\tan 2\theta}{1 - \dfrac{2EV_{CC}}{\Delta m^2 \cos 2\theta}} \ , \tag{1.49}$$

and to an effective squared mass difference

$$\Delta m^2_M = \sqrt{(\Delta m^2 \cos 2\theta - 2EV_{CC})^2 + (\Delta m^2 \sin 2\theta)^2} \ . \tag{1.50}$$

Equation (1.49) shows a resonant behavior when $\Delta m^2 \cos 2\theta = 2\sqrt{2} G_F E n_e$, called "resonance condition", leading to $\theta_M = \pi/4$ irrespective to the value of the mixing angle θ in the vacuum. The two-flavor probability for the oscillation in matter has the form [13]

$$P^M_{\nu_\alpha \to \nu_\beta}(L, E) = \sin^2 2\theta_M \sin^2 \frac{\Delta m^2_M}{4E} L \ . \tag{1.51}$$

In the most general case of three neutrinos, the $\nu_e \to \nu_\mu$ and $\overline{\nu}_e \to \overline{\nu}_\mu$ oscillations differ for the sign of δ ($\delta \to -\delta$) and for the sign of the potential ($n_e \to -n_e$), see for instance Ref. [15]. Thus neutrino-antineutrino asymmetry is induced both by genuine CP violation and by matter effects, and this can induce a fake CP-violating effect even if the CP phase δ is 0 or π. This requires an accurate control of matter effects in order to disentangle the genuine CP-violating effect due to a possible Dirac phase $\delta \neq 0, \pi$.

It is beyond the scope of this thesis to discuss all the transition probabilities in the different channels, but we present only those which are useful for the studies presented in Chapter 5, characterized by experimental setups with the ratios $L/E \lesssim 10^3$ km/GeV and by nearly constant matter density (in the Earth's crust).

We consider the appearance channels $\nu_\mu \to \nu_e$ and $\overline{\nu}_\mu \to \overline{\nu}_e$, whose oscillation probabilities in matter with constant density can be obtained by expanding to second order in the small parameters $\sin\theta_{13}$ and $\alpha = \Delta m^2_{21}/\Delta m^2_{31}$ [15, 16]

$$\begin{aligned} P_{\nu_\mu \to \nu_e}(L, E, \delta, V_{CC}) =& \alpha^2 \sin^2 2\theta_{12} \cos^2\theta_{23} \frac{\sin^2 A\Delta}{A^2} + 4 \sin^2\theta_{13} \sin^2\theta_{23} \frac{\sin^2(A-1)\Delta}{(A-1)^2} + \\ &+ 2\alpha \sin\theta_{13} \sin 2\theta_{12} \sin 2\theta_{23} \cos(\Delta + \delta) \frac{\sin A\Delta}{A} \frac{\sin(A-1)\Delta}{A-1} \end{aligned} \tag{1.52}$$

$$P_{\overline{\nu}_\mu \to \overline{\nu}_e}(L, E, \delta, V_{CC}) = P_{\nu_\mu \to \nu_e}(L, E, -\delta, -V_{CC}) \ , \tag{1.53}$$

where

$$\Delta \equiv \frac{\Delta m^2_{31} L}{4E} \ , \tag{1.54}$$

$$A \equiv \frac{V_{CC} L}{2\Delta} \ . \tag{1.55}$$

In the disappearance channel, oscillation probabilities of $\nu_\mu \to \nu_\mu$ and $\overline{\nu}_\mu \to \overline{\nu}_\mu$ can be approximated as

$$
\begin{aligned}
P_{\nu_\mu\to\nu_\mu}(L,E,\delta,V_{CC}) =& 1-\sin^2 2\theta_{23}\sin^2\Delta+\alpha\cos^2\theta_{12}\sin^2 2\theta_{23}\Delta\sin 2\Delta+ \\
&-\alpha^2\sin^2 2\theta_{12}\cos^2\theta_{23}\frac{\sin^2 A\Delta}{A^2}-\alpha^2\cos^4\theta_{12}\sin^2 2\theta_{23}\Delta^2\cos 2\Delta+ \\
&+\frac{\alpha^2}{2A}\sin^2 2\theta_{12}\sin^2 2\theta_{23}\left(\sin\Delta\frac{\sin A\Delta}{A}\cos(A-1)\Delta-\frac{\Delta}{2}\sin 2\Delta\right)+ \\
&-4\sin^2\theta_{13}\sin^2\theta_{23}\frac{\sin^2(A-1)\Delta}{(A-1)^2}+ \\
&-\frac{2}{A-1}\sin^2\theta_{13}\sin^2 2\theta_{23}\left(\sin\Delta\cos A\Delta\frac{\sin(A-1)\Delta}{A-1}-\frac{A}{2}\Delta\sin 2\Delta\right)+ \\
&-2\alpha\sin\theta_{13}\sin 2\theta_{12}\sin 2\theta_{23}\cos\delta\cos\Delta\frac{\sin A\Delta}{A}\frac{\sin(A-1)\Delta}{A-1}+ \\
&+\frac{2\alpha}{A-1}\sin\theta_{13}\sin 2\theta_{12}\sin 2\theta_{23}\cos 2\theta_{23}\cos\delta\sin\Delta\times \\
&\times\left(A\sin\Delta-\frac{\sin A\Delta}{A}\cos(A-1)\Delta\right)\,,
\end{aligned}
\tag{1.56}
$$

$$
P_{\overline{\nu}_\mu\to\overline{\nu}_\mu}(L,E,\delta,V_{CC}) = P_{\nu_\mu\to\nu_\mu}(L,E,-\delta,-V_{CC})\ . \tag{1.57}
$$

Notice that in the limit $A\to 0$ (vanishing electron density n_e) it is possible to recover the oscillation probabilities in vacuum. For a comprehensive discussion of neutrino oscillations in vacuum and in matter see, for instance, Ref. [9].

1.3 Experimental status

As we saw in the previous section, the oscillation probability in Eq. (1.31) depends on the oscillation phase

$$
\phi_{kj}=\frac{\Delta m^2_{kj}L}{2E}\ , \tag{1.58}
$$

whose value (ideally of order unity) can be useful to classify neutrino experiments sensitive to different values of the squared mass differences, depending on their typical L/E ratio [7, 9, 10]. We can thus distinguish:

- **Long-Baseline** accelerator experiments, which use neutrinos produced by the decay of pions and kaons initially produced by a proton beam hitting a target. These experiments, using neutrino beams over large distances of hundred of km ($L=\mathcal{O}(100-1000)$ km), are characterized by the ratio $L/E\lesssim 10^3$ km/GeV, thus sensitive to $\Delta m^2\gtrsim 10^{-3}$ eV^2.

- **Short-Baseline** accelerator experiments, which are similar to the long-baseline experiments except for the fact that their baselines are much shorter, $L=\mathcal{O}(100)$ m. This class of experiments is sensitive to $\Delta m^2\gtrsim 1$ eV^2.

- **Short-Baseline** & **Long-Baseline** reactor experiments, which use fluxes of electron antineutrinos produced in nuclear reactors by β^- decays. In this case the ratios are $L/E\lesssim 10$ m/MeV and $L/E\lesssim 10^3$ m/MeV, respectively.

- **Atmospheric neutrino** experiments which mainly measure the flux of ν_μ and ν_e that result from cosmic rays colliding with the upper layers of the atmosphere. In this case $L/E \lesssim 10^4$ km/GeV, thus sensitive to $\Delta m^2 \gtrsim 10^{-4}$ eV^2.
- **Solar neutrino** experiments which detect neutrinos generated in the core of the Sun by the thermonuclear reactions. In this case $L/E \lesssim 10^{12}$ m/MeV, thus sensitive to $\Delta m^2 \gtrsim 10^{-12}$ eV^2.

Over the past 40 years many efforts have been performed in order to search for mass-mixing properties of neutrinos [7, 9, 10]. The pioneering results obtained by the radiochemical Homestake experiment with Cl [17], showing a deficit of electron neutrinos coming from the Sun (*solar neutrino problem*) compared to the number predicted by the *Standard Solar Model*, provided a first evidence of oscillations. The same deficit was confirmed by other experiments like SAGE [18], GALLEX [19], GNO [20], with radiochemical measurements on ^{71}Ge. The Kamiokande experiment in Japan [21], using neutrino-electron scattering in a water-Cherenkov detector, gave the first direct evidence that neutrinos come from the direction of the Sun. The long-baseline reactor experiment KamLAND [22] observed a reduction around 40% compared to the predicted flux for electron anti-neutrinos, consistent with solar results. More recently, the SNO experiment [23] using heavy-water detector, measured the ^{8}B solar neutrino flux via charged- and neutral-current interactions and found a direct evidence for solar ν_e disappearance. In the last few years important results have been obtained by the Borexino detector in the Gran Sasso laboratory [24], providing a measurement of the energy profile of the survival probability for solar neutrinos. All the solar neutrino and KamLAND disappearance data can be accommodated in a simple scenario of two-neutrino mixing with $\Delta m^2_{sol} \equiv \Delta m^2_{21} = 7.6 \times 10^{-5} eV^2$ and $\sin^2\theta_{sol} \equiv \sin^2\theta_{12} = 0.32$.

Many important results were independently achieved in the study of atmospheric neutrinos, generated by the interaction of cosmic rays with the upper atmosphere in a wide range of energies.

Super-Kamiokande [25], tracking events with Cherenkov light emitted by charged leptons produced by neutrino interactions, was able to distinguish muon and electron neutrino events and observed a deficit of ν_μ. Muon neutrino disappearance was also strongly confirmed by the long-baseline accelerator experiments K2K [26], MINOS [27] and T2K [28]. The results obtained from atmospheric neutrinos allowed to evaluate the so-called atmospheric oscillations parameters, that is $|\Delta m^2_{atm}| = 2.4 \times 10^{-3} eV^2$ and $\sin^2 2\theta_{atm} \equiv \sin^2 2\theta_{23} = 1$.

For appearance experiments, evidence of ν_τ from $\nu_\mu \to \nu_\tau$ was established by OPERA [29], while $\nu_\mu \to \nu_e$ was observed by T2K [30] and MINOS [31].

In 2012, experimental results on $\overline{\nu}_e$ from Daya Bay [32], Double Chooz [33] and RENO [34], gave a strong evidence of a non-zero value for θ_{13}: $\sin^2\theta_{13} \simeq 0.02$.

The current best-fit values and allowed ranges for the oscillation parameters are summarized in Tab. 1.1, and they are reported with errors at 1σ and also the values at 3σ for both orderings, as explained below. The reported values are obtained from the global analysis of Ref. [35].

Notice that in oscillation experiments it is possible to evaluate three different squared mass differences, but only two are independent, and the experimental results are compatible with two possible orderings:

- *Normal Ordering* (NO), in which the pattern assumed is $m_1 < m_2 < m_3$, and is such that

$$\Delta m^2_{atm} \equiv \Delta m^2_{31} > 0 \ ,$$

- *Inverted Ordering* (IO), such that $m_3 < m_1 < m_2$, which means

$$\Delta m^2_{atm} \equiv \Delta m^2_{32} < 0 \ .$$

Even if neutrino masses and mixing have been largely established, there are still several unknowns that need to be addressed by current and future experiments:

- the nature of neutrinos (Dirac *vs* Majorana),
- the absolute mass scale,
- the value of the Dirac CP-violating phase,
- the sign of Δm^2_{atm},
- high precision determinations of the oscillation parameters.

	Normal Ordering		**Inverted Ordering**	
Parameter	**Best Fit**	**3σ Range**	**Best Fit**	**3σ Range**
$\sin^2\theta_{12}/10^{-1}$	$3.08^{+0.13}_{-0.12}$	2.73 ÷ 3.48	$3.08^{+0.13}_{-0.12}$	2.73 ÷ 3.48
$\sin^2\theta_{13}/10^{-2}$	$2.163^{+0.074}_{-0.074}$	1.938 ÷ 2.388	$2.175^{+0.075}_{-0.074}$	1.950 ÷ 2.396
$\sin^2\theta_{23}/10^{-1}$	$4.40^{+0.23}_{-0.19}$	3.88 ÷ 6.30	$5.84^{+0.18}_{-0.22}$	3.98 ÷ 6.32
δ	$5.04^{+0.66}_{-0.89}$	0 ÷ 2π	$4.69^{+0.68}_{-0.79}$	0 ÷ 2π
$\Delta m^2_{21}/10^{-5}$ [eV^2]	$7.49^{+0.19}_{-0.17}$	7.02 ÷ 8.08	$7.49^{+0.19}_{-0.17}$	7.02 ÷ 8.09
$\Delta m^2_{3\ell}/10^{-3}$ [eV^2]	$+2.526^{+0.039}_{-0.037}$	+2.413 ÷ +2.645	$-2.518^{+0.038}_{-0.037}$	-2.643 ÷ -2.406

Table 1.1: Value of the oscillation parameters obtained from a global analysis from Ref. [35]. For the squared mass difference in the last line, $\ell = 1$ in the Normal Ordering and $\ell = 2$ in the Inverted Ordering.

Information on the absolute neutrino mass scale can be obtained by β-decay experiments and by cosmological data. The neutrino nature can be probed by experiments searching for neutrino-less double-β decay (for a recent review see, for instance, Ref. [36]), whereas the Dirac phase δ is currently being tested by the T2K [37] and NOνA [38] experiments, although with limited sensitivity which can be improved by future long-baseline accelerator experiments.

The interpretation of such a large amount of neutrino oscillation data led to a growing interest in the study of neutrino cross sections, that represent one of the most important ingredients, as well as a source of systematic uncertainties in neutrino experiments. In the past decade, several experimental programs have studied neutrino scattering off different

nuclei. Different experiments have measured the total or differential cross section for neutrino and anti-neutrino scattering. At neutrino energies where the quasi-elastic interaction gives the major contribution, the double differential cross section on carbon has been reported for the first time by MiniBooNE [39, 40, 41, 42], and most recently by T2K [43] and MINERνA [44].
The MINERνA experiment provided measurements of neutrino cross section on different nuclear targets such as Carbon, Iron and Lead [44, 45, 46, 47, 48]. At higher energies, the inclusive cross section is dominated by inelastic scattering, and data have been reported for example by NOMAD [49], SciBooNE [50] and MINOS [51].
Since future experiments like DUNE [52] will use liquid-argon detectors in order to achieve great sensitivity for the study of the oscillation parameters, Argon has been recently studied as nuclear target using the ArgoNeuT detector [53], which reported the measurements of the flux-averaged cross section for muon neutrino and antineutrino.
For a review of current and ongoing measurements of neutrino cross section, see for instance Ref. [10].

Chapter 2

Neutrino-nucleon interactions

In this Chapter we describe the general formalism for the elementary cross section of charged-current (CC) neutrino-nucleon interaction. The cross section is basically determined by the contraction of the leptonic tensor, which is completely defined by the lepton kinematics, and the hadronic tensor, which contains information on strong interaction dynamics and describes the nucleon response. In particular, we focus on the determination of the structure functions, used for the parameterization of the hadronic tensor, in three different channels: quasi-elastic scattering (QE), resonance production (also beyond the Δ region) and deep inelastic scattering (DIS). We also derive an explicit expression of the leptonic tensor.

2.1 Cross Section formalism

Consider the neutrino-nucleon scattering process via charged current

$$\nu(k) + N(p) \to \ell(k') + X(p') \ , \tag{2.1}$$

where the four-momenta are defined as[1]

$$k = (E_\nu, \mathbf{k}) \ , \tag{2.2}$$
$$k' = (E_\ell, \mathbf{k}') \ , \tag{2.3}$$
$$p = (E_p, \mathbf{p}) \ , \tag{2.4}$$
$$p' = (E_{p'}, \mathbf{p}') \ . \tag{2.5}$$

First, we introduce the normalization used for one-fermion states

$$\langle p|p'\rangle = 2E(2\pi)^3\delta^{(3)}(\mathbf{p} - \mathbf{p}') \ . \tag{2.6}$$

Using Dirac's spinors (plane-wave solutions of the Dirac equation describing a single particle state with positive energy E) the normalization conditions are

$$u^\dagger(p,r)u(p,s) = 2E\delta_{rs} \ , \tag{2.7}$$
$$\overline{u}(p,r)u(p,s) = 2m\delta_{rs} \ , \tag{2.8}$$

[1] See Appendix A for the notation.

and the completeness relation reads

$$\sum_s u(p,s)\overline{u}(p,s) = \not{p} + m \ . \tag{2.9}$$

The general formula for the cross section is

$$\begin{aligned} \mathrm{d}\sigma = & \frac{1}{v_{rel}} \frac{1}{2E_p} \frac{1}{2E_\nu} \frac{1}{2E_\ell} \frac{\mathrm{d}^3k'}{(2\pi)^3} \frac{1}{2E_{p'}} \frac{\mathrm{d}^3p'}{(2\pi)^3} (2\pi)^4 \delta^{(4)}(p' + k' - p - k) \times \\ & \times \mathscr{C}^2 \sum_{s_i \ s_f} [\overline{u}_\ell(k')\gamma_\mu(1-\gamma_5)u_\nu(k)][\overline{u}_\nu(k)\gamma_\nu(1-\gamma_5)u_\ell(k')] \times \\ & \times \sum_{\sigma_i \ \sigma_f} \langle N(p)|J^\mu|X(p')\rangle\langle X(p')|J^\nu|N(p)\rangle \ , \end{aligned} \tag{2.10}$$

where we used explicitly the normalization of the states involved in the reaction mechanism. The coefficient $\mathscr{C}$ depends on the reaction mechanism taken into account, and for neutrino CC interaction is given by

$$\mathscr{C} = \frac{G_F|V_{ud}|}{\sqrt{2}} \tag{2.11}$$

where G_F is the Fermi constant and $|V_{ud}|$ is the absolute value of the CKM matrix element for the coupling of the quarks u and d. The general expression for v_{rel} is

$$v_{rel} = \frac{[(k\cdot p)^2 - m_\nu^2 M^2]^{1/2}}{E_\nu E_p} \simeq \frac{[(k\cdot p)^2]^{1/2}}{E_\nu E_p} \simeq 1 \ , \tag{2.12}$$

where we have neglected the neutrino mass m_ν and considered the nucleon at rest with mass M. The next step is to consider that

$$\mathrm{d}^3k' = |\mathbf{k}'|^2 \mathrm{d}k' \mathrm{d}\Omega_\ell = |\mathbf{k}'| E_\ell \mathrm{d}E_\ell \mathrm{d}\Omega_\ell \ , \tag{2.13}$$

where Ω_ℓ is the solid angle of the outgoing lepton. The sums in Eq. (2.10) include an averaging and a sum over the spins of the particles in the initial and final state, respectively. Thus, the double differential cross section for neutrino-nucleon scattering is

$$\begin{aligned} \frac{\mathrm{d}^2\sigma_{\nu N}}{\mathrm{d}E_\ell \mathrm{d}\Omega_\ell} = & \frac{1}{16\pi^2} \frac{|\mathbf{k}'|}{|\mathbf{k}|} \frac{G_F^2|V_{ud}|^2}{2} \times \\ & \times \sum_{s_i \ s_f} [\overline{u}_\ell(k')\gamma_\mu(1-\gamma_5)u_\nu(k)][\overline{u}_\nu(k)\gamma_\nu(1-\gamma_5)u_\ell(k')] \times \\ \times \sum_{\sigma_i \ \sigma_f} \frac{1}{2E_p} \frac{1}{2E_{p'}} \int & \mathrm{d}^3p' \langle N(p)|J^\mu|X(p')\rangle\langle X(p')|J^\nu|N(p)\rangle \delta^{(4)}(p' + k' - p - k) \ . \end{aligned} \tag{2.14}$$

We define the leptonic tensor as

$$L_{\mu\nu} = \sum_{s_i s_f} [\overline{u}_\ell(k')\gamma_\mu(1-\gamma_5)u_\nu(k)][\overline{u}_\nu(k)\gamma_\nu(1-\gamma_5)u_\ell(k')] = \tag{2.15}$$
$$= \mathrm{Tr}[\not{k}'\gamma_\mu(1-\gamma_5)\not{k}\gamma_\nu(1-\gamma 5)] =$$
$$= 8[k_\mu k'_\nu + k'_\mu k_\nu - g_{\mu\nu} k\cdot k' - i\varepsilon_{\mu\nu\alpha\beta}k'^\beta k^\alpha] \ ,$$

where all lepton masses are neglected, $g_{\mu\nu}$ is the metric tensor and $\varepsilon_{\mu\nu\alpha\beta}$ is the fully antisymmetric Levi-Civita tensor[2]. The hadronic tensor is instead defined by

$$W_{\mu\nu} = \sum_{\sigma_i\ \sigma_f} \frac{1}{2E_p} \int \frac{\mathrm{d}^3p'}{2E_{p'}} \langle N(p)|J^\mu|X(p')\rangle\langle X(p')|J^\nu|N(p)\rangle \delta^{(4)}(p'+k'-p-k) \ . \tag{2.16}$$

Thus the double differential cross section reads [54, 55, 56, 57]

$$\frac{\mathrm{d}^2\sigma_{\nu N}}{\mathrm{d}E_\ell \mathrm{d}\Omega_\ell} = \frac{1}{16\pi^2}\frac{|\mathbf{k}'|}{|\mathbf{k}|}\frac{G_F^2|V_{ud}|^2}{2} L_{\mu\nu}W^{\mu\nu} \ , \tag{2.17}$$

and the amplitude squared of the process can be written as

$$|\overline{\mathcal{M}}_{fi}|^2 = \frac{G_F^2|V_{ud}|^2}{2} L_{\mu\nu}W^{\mu\nu} \ . \tag{2.18}$$

Furthermore, we can consider that

$$\frac{\mathrm{d}^3p'}{2E'_p} = \mathrm{d}^4p' \ \delta(p'^2 - M'^2) \ , \tag{2.19}$$

where M' is the mass of the final state. Thus integrating over d^4p' the $\delta^{(4)}$ function, the hadronic tensor reads

$$W_{\mu\nu} = \sum_{\sigma_i\ \sigma_f} \frac{1}{2E_p} \langle N(p)|J^\mu|X(p')\rangle\langle X(p')|J^\nu|N(p)\rangle \delta((p+q)^2 - M'^2) \ . \tag{2.20}$$

where q is the four-momentum transferred, $q = p' - p$. In the most general case the above formula can be expressed as a function of six independent structure functions W_i

$$W_{\mu\nu} = -g_{\mu\nu}W_1 + \frac{W_2}{M^2}p_\mu p_\nu - i\varepsilon_{\mu\nu\alpha\beta}p^\alpha q^\beta \frac{W_3}{2M^2} + q_\mu q_\nu \frac{W_4}{M^2} + \tag{2.21}$$
$$+ (p_\mu q_\nu + q_\mu p_\nu)\frac{W_5}{M^2} + i(p_\mu q_\nu - q_\mu p_\nu)\frac{W_6}{2M^2} \ ,$$

however the term in W_6 does not contribute to the cross section, thus the final expression for $W_{\mu\nu}$ is

$$W_{\mu\nu} = -g_{\mu\nu}W_1 + \frac{W_2}{M^2}p_\mu p_\nu - i\varepsilon_{\mu\nu\alpha\beta}p^\alpha q^\beta \frac{W_3}{2M^2} + q_\mu q_\nu \frac{W_4}{M^2} + (p_\mu q_\nu + q_\mu p_\nu)\frac{W_5}{M^2} \ . \tag{2.22}$$

The averaging over the initial spin σ_i of the target brings a factor 1/2. The above hadronic tensor has different parametrizations for each interaction channel. In the next sections we will consider the quasi-elastic interaction, the resonances production and the deep inelastic scattering.

[2]The antisymmetric term of the leptonic tensor changes sign for antineutrino scattering.

The leptonic tensor

The contraction between the two tensors in Eqs. (2.15) and (2.22) leads to

$$\begin{aligned} L^{\mu\nu}W_{\mu\nu} =& 16W_1(k\cdot k') + 8\frac{W_2}{M^2}\Big(2(k\cdot p)(k'\cdot p) - p^2(k\cdot k')\Big) + \\ &- 16\frac{W_3}{2M^2}\Big((k'\cdot p)(k\cdot q) - (k\cdot p)(k'\cdot q)\Big) + \\ &+ 8\frac{W_4}{M^2}\Big(2(k\cdot q)(k'\cdot q) - q^2(k\cdot k')\Big) + \\ &+ 16\frac{W_5}{M^2}\Big((k'\cdot p)(k\cdot q) + (k\cdot p)(k'\cdot q) - (k\cdot k')(p\cdot q)\Big) \ , \end{aligned} \tag{2.23}$$

thus, it is possible to rewrite [54]

$$L_{\mu\nu}W^{\mu\nu} = \frac{16}{M^2}\sum_i L_i W_i \ , \tag{2.24}$$

where the W_i will be derived in next sections, and the L_i are

$$L_1 = M^2(k\cdot k') \ , \tag{2.25}$$

$$L_2 = (k\cdot p)(k'\cdot p) - \frac{p^2}{2}(k\cdot k') \ , \tag{2.26}$$

$$L_3 = -\frac{1}{2}\Big((k'\cdot p)(k\cdot q) - (k\cdot p)(k'\cdot q)\Big) \ , \tag{2.27}$$

$$L_4 = (k\cdot q)(k'\cdot q) - \frac{q^2}{2}(k\cdot k') \ , \tag{2.28}$$

$$L_5 = (k'\cdot p)(k\cdot q) + (k\cdot p)(k'\cdot q) - (k\cdot k')(p\cdot q) \ , \tag{2.29}$$

with

$$q^2 = (k-k')^2 = k^2 + k'^2 - 2k\cdot k' = m_\ell^2 - 2k\cdot k' = m_\ell^2 - 2E_\nu E_\ell + 2\mathbf{k}\cdot\mathbf{k}' \ , \tag{2.30}$$

$$p^2 = M^2 \ . \tag{2.31}$$

To proceed with the calculation of the cross section, we choose $\hat{q}$ along the $\hat{z}$ direction and $\hat{y}$ perpendicular to the scattering plane, as in Fig. 2.1.
Thus, being $\mathbf{q} = (0,0,q_z)$, $\mathbf{k} = (k_x,0,k_z)$ and $\mathbf{k}' = (k'_x,0,k'_z)$ with $k_x = k'_x$, we have the following expansion of the scalar products of Eqs. (2.25)-(2.29)

$$k\cdot k' = E_\nu E_\ell - \mathbf{k}\cdot\mathbf{k}' = \frac{1}{2}(m_\ell^2 - q^2) \ , \tag{2.32}$$

$$k\cdot p = E_\nu E_p - k_x p_x - k_z p_z \ , \tag{2.33}$$

$$k'\cdot p = E_\ell E_p - k'_x p_x - k'_z p_z \ , \tag{2.34}$$

$$k\cdot q = E_\nu\omega - k_z|\mathbf{q}| \ , \tag{2.35}$$

$$k'\cdot q = E_\ell\omega - k'_z|\mathbf{q}| \ , \tag{2.36}$$

$$p\cdot q = E_p\omega - p_z|\mathbf{q}| \ , \tag{2.37}$$

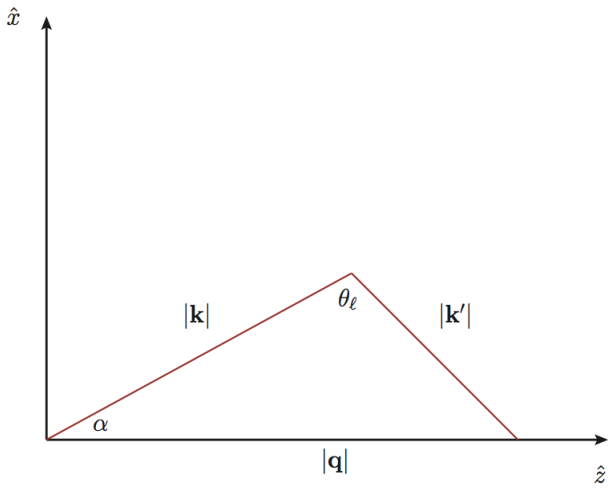

Figure 2.1: Schematic representation of the scattering plane.

and it is possible to rewrite

$$m_\nu^2 = 0 = E_\nu^2 - k_x^2 - k_z^2 \Rightarrow k_z = \sqrt{E_\nu^2 - k_x^2} \ , \tag{2.38}$$

$$k_x = k'_x = |\mathbf{k}| \sin\alpha = \frac{|\mathbf{k}||\mathbf{k}'|}{|\mathbf{q}|} \sin\theta_\ell = \frac{E_\nu |\mathbf{k}'|}{|\mathbf{q}|} \sin\theta_\ell \ , \tag{2.39}$$

$$|\mathbf{q}| = q_z = k_z - k'_z \ , \tag{2.40}$$

where α is the angle between the incoming neutrino and $\hat{q}$, and θ_ℓ is the emission angle of the outgoing lepton. The explicit form obtained for the L_i are reported in Appendix B.

2.2 Quasi-elastic channel

In the quasi-elastic interaction the hadron produced at the interaction vertex is a nucleon, and the hadronic tensor in Eq. (2.20) can be written as[3] [58]

$$W_{\mu\nu} \propto \sum_{\sigma_i \sigma_f} \overline{u}(p) \tilde{\Gamma}_\mu^{QE} u(p') \overline{u}(p') \Gamma_\nu^{QE} u(p) \ . \tag{2.41}$$

The hadronic current of the process has a vector – axial (**V** - **A**) structure, and it is possible to write

$$J_\mu^{QE} = \langle N', \mathbf{p}' | J^\mu(0) | N, \mathbf{p} \rangle = \overline{u}(p') \Gamma_\mu^{QE} u(p) \ , \tag{2.42}$$

with

$$\Gamma_\mu^{QE} = J_\mu^V - J_\mu^A \ , \tag{2.43}$$

[3]The proportionality symbol is used to remind that the normalization of spinors must be included in the evaluation of the cross section.

and

$$J_\mu^V = F_1\gamma_\mu + i\sigma_{\mu\nu}q^\nu\frac{F_2}{2M} + \frac{q_\mu}{M}F_S \ , \tag{2.44}$$

$$-J_\mu^A = \gamma_\mu\gamma_5 F_A + q_\mu\gamma_5\frac{F_P}{M} \ , \tag{2.45}$$

where $F_{1,2}$ are the Dirac and Pauli form factors, respectively, F_S is the scalar form factor and F_A and F_P are the axial and pseudo-scalar form factors, respectively.
The CVC (*Conserved Vector Current*) hypothesis [4, 5, 6] allows to set $F_S = 0$ and to relate the Dirac and Pauli form factors to the electromagnetic proton and neutron form factors, extracted from electron scattering off hydrogen and deuterium

$$F_1 = F_1^p - F_1^n \ , \tag{2.46}$$

$$F_2 = F_2^p - F_2^n \ . \tag{2.47}$$

It is also possible to relate the vector form factors to the electric and magnetic form factors, G_E and G_M

$$G_E(q^2) = F_1(q^2) - \tau F_2(q^2) \ , \tag{2.48}$$

$$G_M(q^2) = F_1(q^2) + F_2(q^2) \ , \tag{2.49}$$

with $\tau = q^2/4M^2$. The most popular parameterization is the dipole form

$$G_E(q^2) = \left(1 - \frac{q^2}{M_V^2}\right)^{-2} \ , \tag{2.50}$$

$$G_M(q^2) = (\mu_n - \mu_p)\left(1 - \frac{q^2}{M_V^2}\right)^{-2} \ , \tag{2.51}$$

with $\mu_n = -1.91$ and $\mu_p = 2.79$ the magnetic moment of the neutron and of the proton respectively, and $M_V = 0.71$ GeV is the vector mass. The vector form factors are then

$$F_1(q^2) = \frac{1}{1-\tau}[G_E(q^2) - \tau G_M(q^2)] \ , \tag{2.52}$$

$$F_2(q^2) = \frac{1}{1-\tau}[-G_E(q^2) + G_M(q^2)] \ . \tag{2.53}$$

More refined parameterizations are available [59, 60], accurately derived from electron scattering data. To evaluate the cross section in the QE channel we used the vector form factors from Ref. [59].
For the axial part, with the PCAC (*Partially Conserved Axial Current*) hypothesis [4, 5, 6] it is possible to relate F_P and F_A

$$F_P = \frac{2M^2}{(m_\pi^2 - q^2)}F_A \ , \tag{2.54}$$

and F_A can be expressed in the standard dipole form as

$$F_A(q^2) = g_A\left(1 - \frac{q^2}{M_A^2}\right)^{-2} , \tag{2.55}$$

where $g_A = -1.26$ is the axial coupling constant obtained from β-decay, and $M_A = 1.03$ GeV is the nucleon axial mass.
Finally, the hadronic tensor for the quasi elastic scattering reads

$$W_{\mu\nu}^{QE} \propto \frac{1}{2}\mathrm{Tr}[(\not{p} + M)\tilde{\Gamma}_\mu^{QE}(\not{p}' + M')\Gamma_\nu^{QE}] , \tag{2.56}$$

with $\tilde{\Gamma}_\mu^{QE} = \gamma_0 \Gamma_\mu^{QE\dagger}\gamma_0$. The factor 1/2 represents the averaging over the initial nucleon spin. From Eqs. (2.56) and (2.22) we obtain

$$W_1 = 4M^2\left[(F_1 + F_2)^2\frac{Q^2}{4M^2} + F_A^2\left(1 + \frac{Q^2}{4M^2}\right)\right] , \tag{2.57}$$

$$W_2 = 4M^2\left(F_1^2 + \frac{Q^2}{4M^2}F_2^2 + F_A^2\right) , \tag{2.58}$$

$$W_3 = -8M^2 F_A(F_1 + F_2) , \tag{2.59}$$

$$W_4 = -2M^2\left[F_1F_2 + \frac{F_2}{4M^2}\left(2M^2 - \frac{Q^2}{2}\right) - F_P^2\frac{Q^2}{2M^2} + 2F_AF_P\right] , \tag{2.60}$$

$$W_5 = \frac{W_2}{2} . \tag{2.61}$$

2.3 Resonance production

The most important contribution to the cross section, beyond the QE peak, is given by the excitation of nuclear resonances, such as the $\Delta(1232)$. The state of the Δ, or more generally of any spin 3/2 particle, can be described using the Rarita-Schwinger formalism [61], yielding

$$\sum_s \psi_\alpha^\Delta(p', s)\overline{\psi}_\beta^\Delta(p', s) = \Lambda_{\alpha\beta}(p') = -(\not{p}' - M')\left(g_{\alpha\beta} - \frac{2}{3}\frac{p'_\alpha p'_\beta}{M'^2} + \frac{p'_\alpha\gamma_\beta - p'_\beta\gamma_\alpha}{3M'} - \frac{1}{3}\gamma_\alpha\gamma_\beta\right) , \tag{2.62}$$

where M' is the mass of the resonance. As for the CC QE interaction, the production of a spin 3/2-resonance has a **V-A** structure, and we can write the hadronic current in a similar way

$$J_\mu^{CC} = \langle R, \mathbf{p}'|J_\mu(0)|N, \mathbf{p}\rangle = \overline{\psi}_\lambda^\Delta(p')\Gamma^{\lambda\nu}u(p) , \tag{2.63}$$

where

$$\Gamma^{\lambda\nu} = \Gamma_{\mathbf{V}}^{\lambda\nu} - \Gamma_{\mathbf{A}}^{\lambda\nu} . \tag{2.64}$$

Following Refs. [58, 62, 63, 64], the axial and vector parts can be parametrized in terms of form factors as

$$\Gamma^{\lambda\nu}_{\mathbf{V}} = g^{\lambda\nu}\Big[\frac{C_3}{M}\not{q} + \frac{C_4}{M^2}(p'\cdot q) + \frac{C_5}{M^2}(p\cdot q) + C_6\Big]\gamma_5 - q^\lambda\Big[\frac{C_3}{M}\gamma^\nu + \frac{C_4}{M^2}p'^\nu + \frac{C_5}{M^2}p^\nu\Big]\gamma_5 \ , \tag{2.65}$$

$$-\Gamma^{\lambda\nu}_{\mathbf{A}} = g^{\lambda\nu}\Big[\frac{A_3}{M}\not{q} + \frac{A_4}{M^2}(p'\cdot q)\Big] - q^\lambda\Big[\frac{A_3}{M}\gamma^\nu + \frac{A_4}{M^2}p'^\nu\Big] + g^{\lambda\nu}A_5 + q^\lambda q^\nu\frac{A_6}{M^2} \ , \tag{2.66}$$

where the C_i and the A_i stand for the vector and axial form factors, respectively.
Isospin relations allow to relate the matrix elements of CC interaction for resonance production for the scattering off proton and neutron

$$\langle\Delta^{++}|J^\mu|p\rangle = \sqrt{3}\langle\Delta^+|J^\mu|n\rangle \ , \tag{2.67}$$

thus

$$\langle\Delta^{++}|J^\nu|p\rangle = \sqrt{3}\overline{\psi}^\Delta_\lambda(p')\Gamma^{\lambda\nu}u(p) \ . \tag{2.68}$$

Exploiting the usual spinors projectors of Eq. (2.9), and the one for resonance production of Eq. (2.62), the hadronic tensor for neutrino scattering can be written as

$$W^{\mu\nu} \propto \frac{3}{2}\mathrm{Tr}[\tilde{\Gamma}^{\mu\sigma}\Lambda_{\sigma\lambda}\Gamma^{\lambda\nu}(\not{p}+M)] \tag{2.69}$$

where $\Lambda_{\sigma\lambda}$ is given in Eq. (2.62) and $\tilde{\Gamma}^{\mu\sigma} = \gamma^0(d^\dagger)^{\mu\sigma}\gamma^0$ is given by

$$\begin{aligned}\tilde{\Gamma}^{\mu\sigma} =& g^{\mu\sigma}\Big[\frac{C_3}{M}\not{q} - \frac{C_4}{M^2}(p'\cdot q) - \frac{C_5}{M^2}(p\cdot q) - C_6\Big]\gamma_5 - \Big[\frac{C_3}{M}\gamma^\mu - \frac{C_4}{M^2}p'^\mu - \frac{C_5}{M^2}p^\mu\Big]q^\sigma\gamma_5 + \\ &+ g^{\mu\sigma}\Big[\frac{A_3}{M}\not{q} + \frac{A_4}{M^2}(p'\cdot q)\Big] - \Big[\frac{A_3}{M}\gamma^\mu + \frac{A_4}{M^2}p'^\mu\Big]q^\sigma + g^{\mu\sigma}A_5 + q^\mu q^\sigma\frac{A_6}{M^2} \ .\end{aligned} \tag{2.70}$$

At this point, even if the structure of cross section and current has been set, the main problem is the determination of the form factors.
The vector form factors can be extrapolated from helicity amplitudes of electro-production data [58, 62, 63, 64]. In the electromagnetic interaction the current can be expressed in a similar way as in Eq. (2.64), but setting the axial components equal to zero. Thus only the terms of Eq. (2.65) will contribute, with vector form factors replaced by the electromagnetic form factors. Experimental data of electro-production are obtained for the cross sections at the peak of each resonance, and they are a function of the amplitudes, related to the electromagnetic matrix elements [65, 66, 67, 68]

$$A_{1/2} \propto \langle R, +\frac{1}{2}|J_{em}\cdot\varepsilon^R|N, -\frac{1}{2}\rangle \ , \tag{2.71}$$

$$A_{3/2} \propto \langle R, +\frac{3}{2}|J_{em}\cdot\varepsilon^R|N, +\frac{1}{2}\rangle \ , \tag{2.72}$$

$$S_{1/2} \propto \langle R, +\frac{1}{2}|J_{em}\cdot\varepsilon^S|N, +\frac{1}{2}\rangle \ , \tag{2.73}$$

where $|R\rangle$ represents the resonant state and $|N\rangle$ the nucleon state, and the third component of the spin is indicated as well. These amplitudes also depend on the polarization of the

photon, with $\varepsilon^{\mu}_{R,L} = \pm 1/2(0;1,\pm i,0)$ and $\varepsilon^{\mu}_{S} = \pm 1/\sqrt{Q^2}(q^z;0,0,q^0)$. The above matrix elements can then be parametrized as a function of the electromagnetic form factors. The comparison between electromagnetic and weak amplitudes, also using isospin relations, allows to relate the form factors as

$$C_i = C_i^n - C_i^p \qquad \text{for isospin } \frac{1}{2} \text{ resonances,} \tag{2.74}$$

$$C_i = C_i^n = C_i^p \qquad \text{for isospin } \frac{3}{2} \text{ resonances,} \tag{2.75}$$

where C_i and $C_i^{n,p}$ are the vector and electromagnetic form factors, respectively.
For the Δ-resonance, as reported in [63], the extracted vector form factors are parametrized as

$$C_3(Q^2) = \frac{2.13}{1+Q^2/M_V^2}\frac{1}{1+Q^2/(4M_V^2)} , \tag{2.76}$$

$$C_4(Q^2) = \frac{-1.51}{1+Q^2/M_V^2}\frac{1}{1+Q^2/(4M_V^2)} , \tag{2.77}$$

$$C_5(Q^2) = \frac{0.48}{1+Q^2/M_V^2}\frac{1}{1+Q^2/(0.776M_V^2)} , \tag{2.78}$$

$$C_6(Q^2) = 0 \quad \text{for CVC} , \tag{2.79}$$

and the fit to the proton helicity amplitudes is shown in Fig. 2.2, from Ref. [63].

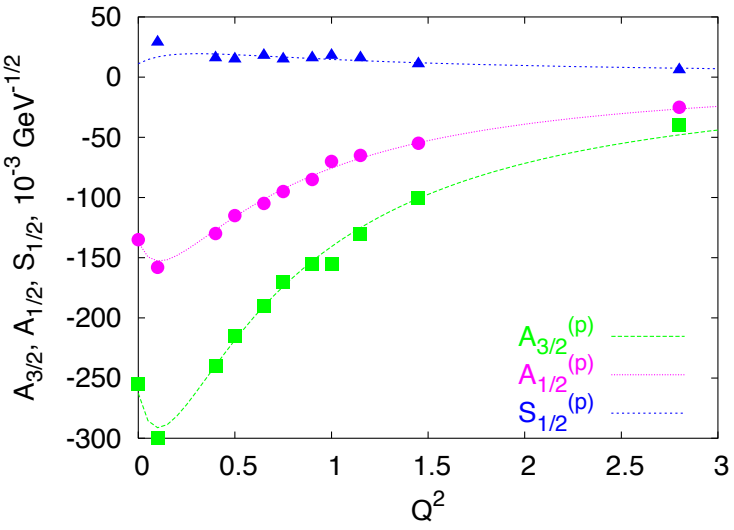

Figure 2.2: Helicity amplitudes for $\Delta(1232)$ from Ref. [63], calculated using Eqs. (2.76)-(2.79). Data are from Ref. [67].

The evaluation of the axial form factors follows a different procedure. According to Ref. [63], an effective Lagrangian for the decay $R \to N\pi$ can be used to evaluate the decay

widths. The PCAC and decay widths for each resonance allow to determine the axial form factors. For $\Delta(1232)$ they are [63]

$$A_3(Q^2) = 0 \ , \tag{2.80}$$

$$A_4(Q^2) = -\frac{A_5}{4} \ , \tag{2.81}$$

$$A_5(Q^2) = \frac{1.2}{(1+Q^2/M_A^2)^2}\frac{1}{1+Q^2/(3M_A)^2} \ , \tag{2.82}$$

$$A_6(Q^2) = A_5\frac{M^2}{Q^2+m_\pi^2} \ , \tag{2.83}$$

with M_A the axial mass, M_V the vector mass and m_π the pion mass. Computing the trace in Eq. (2.69), and using the usual parametrization of the hadronic tensor in terms of the structure functions in Eq. (2.22), it is possible to obtain the W_i, reported in Appendix C. As a final remark we recall that the energy conserving δ-function in Eq. (2.20), can be replaced by a Breit-Wigner function

$$\delta(p'^2 - M'^2) \Rightarrow \frac{\sqrt{p'^2}}{\pi}\frac{\Gamma(p')}{(p'^2-M'^2)^2 + p'^2\Gamma^2(p')} \ . \tag{2.84}$$

The resonance width Γ can be written as[4]

$$\Gamma(W) = \Gamma_0\Big(\frac{p_\pi(W)}{p_\pi(M')}\Big)^3 \ , \tag{2.85}$$

with W the invariant hadronic mass of the final state, $\Gamma_0 = 0.114$ GeV, and the pion momentum p_π given by

$$p_\pi = \frac{1}{2M'}\sqrt{(M'^2 - M^2 - m_\pi^2)^2 - 4M^2m_\pi^2} \ . \tag{2.86}$$

The second resonances region

In the region of resonant pion production the contribution of the Δ-resonance to the neutrino cross section is the most prominent one. However the contribution coming from the second resonance region is not negligible. It includes three isospin 1/2 states: $D_{13}(1520)$, $P_{11}(1440)$ and $S_{11}(1535)$. In the next Chapter we will evaluate the neutrino-nucleus cross section including also these resonances, and the procedure followed for their parametrization is the one used in Refs. [62] and [63].

2.4 Deep inelastic scattering

In the kinematical region in which the neutrino energy is much bigger than the mass of the nucleon, the dominant process is the deep inelastic scattering (DIS) [69, 70, 71].
The contraction of the hadronic tensor with the leptonic one can be simplified if terms proportional to the lepton mass are neglected. In this case the hadronic tensor will be

[4]Notice that the third power dependency on the pion momentum is valid only for spin 3/2-particles. For spin 1/2-particles the dependence is linear.

a function of W_1, W_2 and W_3 dependent on the energy transferred ω and on the four momentum q

$$W_{\mu\nu} = -g_{\mu\nu}W_1 + \frac{W_2}{M^2}p_\mu p_\nu - i\varepsilon_{\mu\nu\alpha\beta}p^\alpha q^\beta \frac{W_3}{2M^2} \ . \tag{2.87}$$

A widely used parametrization, similar to that used in electron scattering, is

$$W_{\mu\nu} = -\left(g_{\mu\nu} + \frac{q_\mu q_\nu}{Q^2}\right)W_1 + \frac{W_2}{M^2}\left(p_\mu + \frac{p\cdot q}{Q^2}q_\mu\right)\left(p_\nu + \frac{p\cdot q}{Q^2}q_\nu\right) - i\varepsilon_{\mu\nu\alpha\beta}p^\alpha q^\beta \frac{W_3}{2M^2} \ . \tag{2.88}$$

Even if the two expressions look different, they lead to the same result if terms proportional to the lepton mass are neglected. The contraction of the leptonic tensor with $W_{\mu\nu}$ of Eq. (2.88) gives

$$\begin{aligned} L^{\mu\nu}W_{\mu\nu} =& 16W_1(k\cdot k') + 8\frac{W_2}{M^2}\Big(2(k\cdot p)(k'\cdot p) - p^2(k\cdot k')\Big) + \\ &- 16\frac{W_3}{2M^2}\Big((k'\cdot p)(k\cdot q) - (k\cdot p)(k'\cdot q)\Big) \ . \end{aligned} \tag{2.89}$$

To describe the process

$$\nu_\ell(k) + N(p) \to \ell^-(k') + X(p') \ , \tag{2.90}$$

it is useful to introduce Lorentz – invariant quantities

$$s = (p+k)^2 \ , \tag{2.91}$$

$$x = \frac{Q^2}{p\cdot q} \ , \tag{2.92}$$

$$y = \frac{p\cdot q}{p\cdot p'} \ , \tag{2.93}$$

where s is the squared center-of-mass energy, x is the *Björken* scaling variable, and y is the scaling variable that defines the fraction of the energy transferred in the interaction process related to the scattering angle in the center-of-mass system.
The evaluation of the double differential cross section in terms of these invariant quantities leads to

$$\begin{aligned} \frac{\mathrm{d}^2\sigma_{\nu N,\overline{\nu}N}}{\mathrm{d}x\mathrm{d}y} =& \frac{G_F^2|V_{ud}|^2(s-M^2)}{2\pi}\Bigg[xy^2MW_1(x,y) + \left(1 - y - \frac{xyM^2}{(s-M^2)}\right)\omega W_2(x,y) + \\ &\pm\left(1-\frac{y}{2}\right)\omega W_3(x,y)\Bigg] \ , \end{aligned} \tag{2.94}$$

where the upper (lower) sign is referred to neutrino (anti-neutrino) charged current interaction. In the limit of $Q^2 \to \infty$ and $\omega \to \infty$, at fixed x, Björken scaling tells us that the structure functions W_i become functions of a single variable x

$$MW_1(x,y) \to F_1(x) \ , \tag{2.95}$$
$$\omega W_2(x,y) \to F_2(x) \ , \tag{2.96}$$
$$\omega W_3(x,y) \to F_3(x) \ . \tag{2.97}$$

Furthermore, from the Callan – Gross relation [71]

$$\omega W_2 = 2xMW_1 \ , \tag{2.98}$$

it follows that

$$F_2 = 2xF_1 \ . \tag{2.99}$$

The double differential cross section can be written in terms of the F_i, as

$$\frac{\mathrm{d}^2\sigma_{\nu N,\overline{\nu}N}}{\mathrm{d}x\mathrm{d}y} = \frac{G_F^2|V_{ud}|^2 s}{2\pi}\left\{\frac{1}{2}[F_2(x) \pm xF_3(x)] + \frac{1}{2}[F_2(x) \mp xF_3(x)](1-y^2)\right\} . \tag{2.100}$$

From the above equation it is possible to extract $F_2(x)$ and $F_3(x)$ from the differential neutrino and antineutrino cross sections

$$F_2 = \frac{1}{\sigma_0}\left(\frac{\mathrm{d}^2\sigma_{\nu N}}{\mathrm{d}x\mathrm{d}y} + \frac{\mathrm{d}^2\sigma_{\overline{\nu}N}}{\mathrm{d}x\mathrm{d}y}\right)[1+(1+y)^2]^{-1} \ , \tag{2.101}$$
$$xF_3 = \frac{1}{\sigma_0}\left(\frac{\mathrm{d}^2\sigma_{\nu N}}{\mathrm{d}x\mathrm{d}y} - \frac{\mathrm{d}^2\sigma_{\overline{\nu}N}}{\mathrm{d}x\mathrm{d}y}\right)[1-(1+y)^2]^{-1} \ , \tag{2.102}$$

where

$$\sigma_0 = \frac{G_F^2|V_{ud}|^2 s}{2\pi} \ . \tag{2.103}$$

The DIS for neutrino-nucleon interaction can be described in the light of the *Quark – Parton Model* (QPM) of hadrons, that allows us to rewrite the structure functions in terms of the partonic distributions. In this model, the nucleon is seen as a composite object, that is a system of three valence quarks and a sea of quark – antiquark pairs of all flavors. Then, the virtual gauge bosons ($W^{\pm}$ and Z for charged and neutral current interaction, respectively) interact with these elementary constituents of the nucleon (quarks).
Within the QPM, the structure functions can be written in the form

$$F_1(x) = \sum_i e_i^2 q_i(x) \ , \tag{2.104}$$
$$F_2(x) = \sum_i x e_i^2 q_i(x) \ ,$$

where $q_i(x)$ can be interpreted as the probability of finding a quark of flavor i, whose charge is e_i, with a fraction x of the of the nucleon momentum in the infinite momentum frame.

To proceed in the treatment of the DIS, we consider the neutrino scattering off a quark

$$\nu_\ell(k) + d(p) \to \ell^-(k') + u(p') \ , \tag{2.105}$$

described by the weak current

$$J^\mu = \overline{u}(x)\gamma^\mu(1-\gamma_5)[d(x)\cos\theta_c + s(x)\sin\theta_c] + \tag{2.106}$$
$$\overline{c}(x)\gamma^\mu(1-\gamma_5)[s(x)\cos\theta_c - d(x)\sin\theta_c] \ , \tag{2.107}$$

with θ_c the Cabibbo angle.
Thus, the cross section for the neutrino and antineutrino scattering is given by

$$\frac{\mathrm{d}\sigma}{\mathrm{d}y}(\nu_\ell + d \to \ell^- + u) = \frac{G_F^2|V_{ud}|^2 xs}{\pi} \ , \tag{2.108}$$

$$\frac{\mathrm{d}\sigma}{\mathrm{d}y}(\overline{\nu}_\ell + u \to \ell^+ + d) = \frac{G_F^2|V_{ud}|^2 xs}{\pi}(1-y)^2 \ . \tag{2.109}$$

Within the QPM the neutrino–nucleon cross section can be expressed as the weighted sum of cross–sections on the quarks

$$\frac{\mathrm{d}^2\sigma}{\mathrm{d}x\mathrm{d}y} = \sum_i x q_i(x)\left(\frac{\mathrm{d}\sigma_i}{\mathrm{d}y}\right)_{\hat{s}=xs} \ , \tag{2.110}$$

with $\hat{s}$ the energy in the center-of-mass of the process at the parton level, and s is referred instead to the process off the nucleon.
Thus, using Eqs. (2.108)-(2.110), the neutrino and antineutrino cross sections are

$$\frac{\mathrm{d}^2\sigma_{\nu N}}{\mathrm{d}x\mathrm{d}y} = \frac{G_F^2|V_{ud}|^2 xs}{2\pi}\left\{[u(x)+d(x)] + [\bar{u}(x)+\bar{d}(x)](1-y)^2\right\} \ , \tag{2.111}$$
$$\frac{\mathrm{d}^2\sigma_{\bar{\nu}N}}{\mathrm{d}x\mathrm{d}y} = \frac{G_F^2|V_{ud}|^2 xs}{2\pi}\left\{[\bar{u}(x)+\bar{d}(x)] + [u(x)+d(x)](1-y)^2\right\} \ . \tag{2.112}$$

Comparing Eq. (2.111) with Eq. (2.100) it is possible to evaluate the F_i as a function of the parton distribution functions

$$2xF_1(x) = F_2(x) = x[q(x) + \bar{q}(x)] \ , \tag{2.113}$$
$$xF_3(x) = x[q(x) - \bar{q}(x)] \ , \tag{2.114}$$

with

$$q(x) = u(x) + d(x) \ , \tag{2.115}$$

neglecting the contribution of quark s.
Finally, the neutrino structure functions can be related to those of electron scattering. Performing the same analysis for electron – nucleon scattering we would have obtained for F_2

$$F_2^{eN}(x) = \frac{5}{18} x[q(x) + \bar{q}(x)] \ , \tag{2.116}$$

that compared to Eq. (2.113), gives

$$F_2^{\nu N}(x) = \frac{18}{5} F_2^{eN}(x) \ . \tag{2.117}$$

The parametrization of the structure functions for the DIS can be performed following two different procedures. It is possible to extrapolate the structure functions from fits on electron–proton and electron–deuteron scattering. In this case resonances and DIS are modeled from data and, even if it does not distinguish the two processes, this procedure avoids the problem of double counting of these effects in the kinematical region where both interaction mechanisms are active.
Alternatively, parton distribution functions can be used directly in the parametrization of the structure functions. The main feature of this approach is the possibility to account for DIS on its own. However, it suffers from the problem linked to the extrapolation of the distributions at low Q^2.
Many different parameterizations are available, and in the following we will briefly discuss two particular cases: the Bodek and Ritchie model [72] which describes, beside the DIS, also the resonance production, and in the second case we consider quark distribution functions, from Glück–Reya–Vogt parametrization [73], used to parametrize the structure functions.

Bodek and Ritchie parameterization

The parametrization of the proton and neutron structure functions of Bodek and Ritchie [72, 74, 75, 76] has the advantage of describing the resonance production and the DIS together.
This parametrization includes effects of scaling violation in terms of a new modified scaling variable ω_ω. In this approach W_2, extrapolated from fits to the SLAC $e-p$ and $e-d$ data [72], is given by

$$\omega W_2(\omega, Q^2) = B(W, Q^2) g\left(\frac{1}{\omega_\omega}\right) \frac{\omega_\omega}{\omega_0} \ , \tag{2.118}$$

$$g\left(\frac{1}{\omega_\omega}\right) = \sum_{n=3}^{n=7} C_n \left(1 - \frac{1}{\omega_\omega}\right)^n \ , \tag{2.119}$$

$$\omega_\omega = \frac{2M\omega + a^2}{Q^2 + b^2} \ . \tag{2.120}$$

with $\omega_0 = 1/x$. The modulating function $B(W, Q^2)$ is close to the unity in the region of the DIS ($W > 2$ GeV), and contains 12 parameters representing the masses, the widths and the amplitudes of the cross sections for the electro-production of the most important resonances, and eight parameters representing the dependence on the invariant hadronic mass W for the low-W contribution and single pion production threshold. All these parameters are extrapolated from the fit to electron scattering data.
Through the link between the electron and neutrino structure functions in Eq. (2.117), it is possible to evaluate W_2 for neutrino scattering.

Given the expressions of the structure functions in terms of the parton distribution functions in Eqs. (2.113) and (2.114), we can use the relation

$$x\omega W_3 = \omega W_2 - 2\bar{Q}_\nu \ . \tag{2.121}$$

and the parametrization for the anti-quark distribution, used in Ref. [74], is

$$\bar{Q}_\nu(x_\omega, Q^2) = \frac{18}{5}\frac{1}{2}\Big(1 - x_\omega\Big)^7 B(W, Q^2) g(0)\frac{\omega_\omega}{\omega} \ , \tag{2.122}$$

with $x_\omega = 1/\omega_\omega$.
The structure functions obtained with the parametrization introduced above are reported in Fig. 2.3, showing ωW_2 for the electron scattering off an isoscalar nucleus. For comparison, the behavior of $x\omega W_3$ rescaled of a factor 5/18 is also shown. Notice that the contribution coming from the resonances is visible at low Q^2, while they start to disappear as the value of Q^2 increases.

Glück–Reya–Vogt parametrization

The Glück–Reya–Vogt parametrization (GRV98) [73] can be used to pin down the contributions of DIS to the cross section. The parton distribution functions (PDFs) are extracted from global fits to different sets of DIS data at high energies and high Q^2, where non-perturbative QCD effects are negligible. This allows to determine the PDFs over a wide range of x and Q^2. The GRV98 parametrization is performed fitting the data collected at HERA [77, 78], obtaining the parton densities and also the proton structure function F_2^p. In GRV98 the structure functions are evolved to extend the kinematical region in x and Q^2, where they can be used. The minimum value of Q^2 was set around 0.8 GeV^2 and for x the minimum value reached is around 10^{-8}.
To study neutrino interactions in the inelastic region we used this parametrization to obtain the structure functions expressed by PDFs, to include DIS processes without the contribution of resonances. To use the PDFs also for $Q^2 \lesssim 0.8$ GeV^2, we used the parton densities keeping Q^2 fixed at the lowest value available.
For comparison we show the behavior of the structure functions obtained using the GRV98 parametrization and the Bodek and Ritchie model. To compare the behavior in a kinematical region where the contribution of the resonances is negligible, in Figs. 2.4 and 2.5, we show the two results obtained for F_2^{ep} extrapolated from electron-proton scattering data with fixed Q^2 at 20 GeV^2 and 100 GeV^2, respectively.
The results obtained for the structure functions within the two different approaches used are clearly different, mostly for $x \lesssim 0.2$. The differences in the small x region is due to the fact that in the Bodek and Ritchie parametrization the fits from electron on fixed-target scattering data are performed up to $x \sim 0.1$. For $x \lesssim 0.1$ the behavior is obtained after extrapolation.

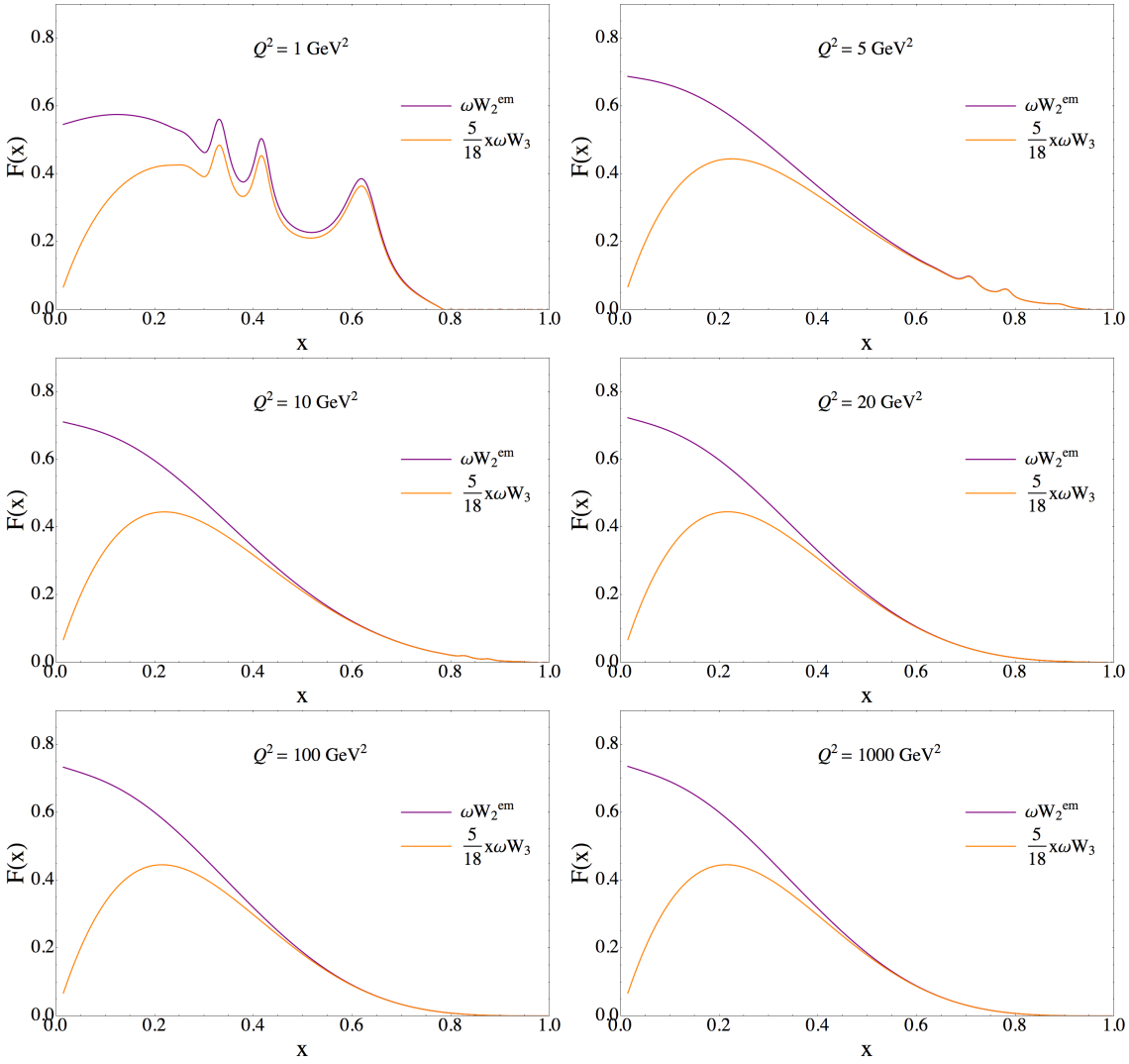

Figure 2.3: Structure functions $\omega W_2^{em}(x) = \omega(W_2^{ep}(x) + W_2^{en}(x))$ and $5/18 x\omega W_3 = 5/18 x\omega(W_3^{\nu p}(x) + W_3^{\nu n}(x))$, at different Q^2, obtained from the parametrization reported in Eqs. (2.118)–(2.120). In the y-axis, $F(x)$ is referred to the two functions shown.

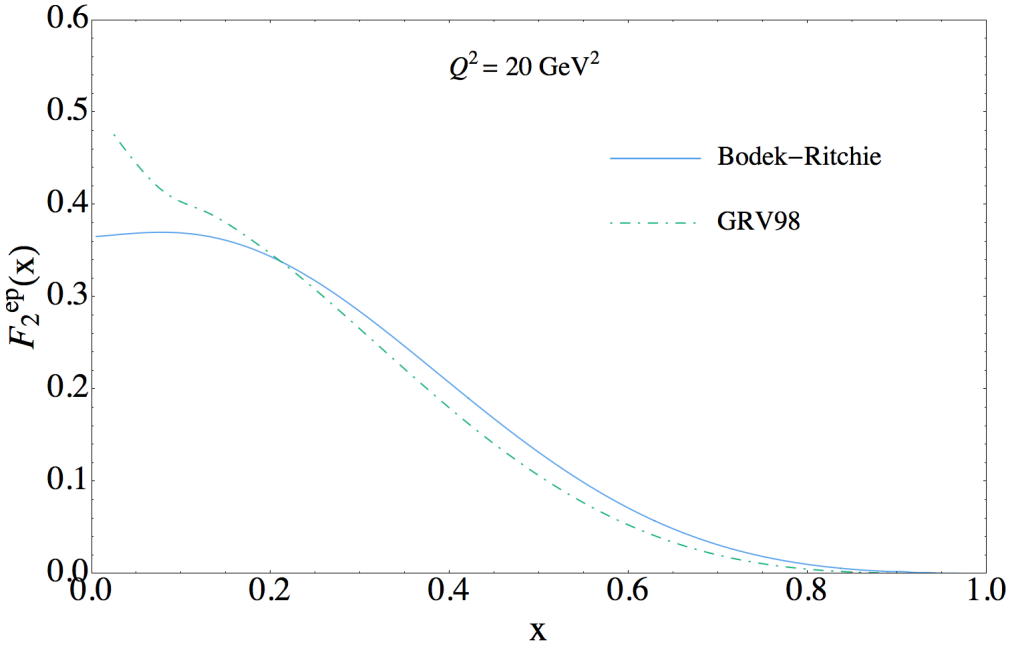

Figure 2.4: Behavior of the proton structure function F_2^{ep} at $Q^2 = 20$ GeV^2, obtained using the Bodek and Ritchie parametrization (solid line) and the GRV98 parametrization (dot-dashed line). In the second case the structure function is computed using PDFs.

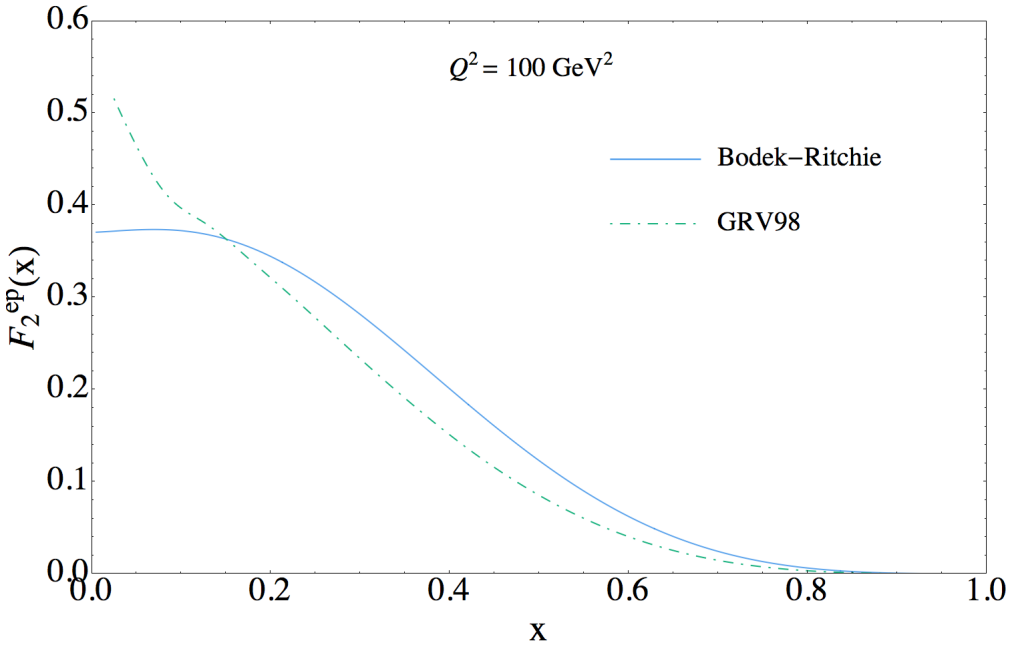

Figure 2.5: As in Fig. 2.4, but at $Q^2 = 100$ GeV^2.

Chapter 3

Neutrino-nucleus interactions

In this Chapter we discuss the charged-current scattering of neutrinos off a nucleus of mass number A, and we report the results obtained for ν_μ-Carbon scattering [79], in the quasi-elastic, resonance production and deep inelastic sectors. The interaction process under study is

$$\nu_\ell(k) + A \to \ell^-(k') + X \ , \tag{3.1}$$

where a neutrino with four momentum $k = (E_\nu, \mathbf{k})$ scatters off a nuclear target of mass number A leading to a final state with a lepton, of four momentum $k' = (E_\ell, \mathbf{k}')$, and an hadronic state X[1].
The double differential cross section of the process can be written in Born approximation, in a form similar to Eq. (2.17)

$$\frac{\mathrm{d}^2\sigma_{\nu A}}{\mathrm{d}\Omega_\ell \mathrm{d}E_\ell} = \frac{G_F^2 |V_{ud}|^2}{16\pi^2} \frac{|\mathbf{k}'|}{|\mathbf{k}|} L_{\mu\nu} W_A^{\mu\nu} \ , \tag{3.2}$$

with G_F the Fermi constant and V_{ud} the CKM matrix element for the $u-d$ coupling. The leptonic tensor $L_{\mu\nu}$ is completely defined by the leptonic kinetic variables and is given in Eq. (2.15). The hadronic tensor $W_A^{\mu\nu}$ can be written in a form similar to Eq. (2.16), indicating with $|0\rangle$ the nuclear ground state with four-momentum $P_0 = (E_0, \mathbf{p}_0)$

$$W_A^{\mu\nu} = \sum_X \int \mathrm{d}^3 p_X \ \langle 0|J_A^\mu|X\rangle\langle X|J_A^\nu|0\rangle \delta^{(4)}(P_X + k' - P_0 - k) \ , \tag{3.3}$$

the summation being carried over all possible final states $|X\rangle$, with four-momentum $P_X = (E_X, \mathbf{p}_X)$, including eventually the spinors' normalizations. The above definition also involves the nuclear current J_A^μ. The evaluation of the nuclear response tensor $W_A^{\mu\nu}$ will be derived in the next section within the *Impulse Approximation* (IA).

3.1 The Impulse Approximation

The definition of the hadronic tensor involves initial and final hadronic states and the nuclear hadronic current. The nuclear ground state can be described in the *non-relativistic many-body theory* (NMBT).

[1] See Appendix A for a brief discussion of the notation used.

In this approach the nucleons are described as point-like particles and the nuclear dynamics is described by the non-relativistic Hamiltonian

$$\mathscr{H} = \sum_{i=1}^{A} \frac{\mathbf{p}_i}{2M} + \sum_{j>i=1}^{A} v_{ij} + \sum_{k>j>i=1}^{A} V_{ijk} \ , \tag{3.4}$$

where $\mathbf{p}_i$ is the momentum of the i-th nucleon, v_{ij} is the potential describing two-nucleons interactions (first described by Yukawa [80]), and V_{ijk} is the interaction potential for three-nucleon states. NMBT allows to describe the tensor of Eq. (3.3) of light nuclei in the region of low momentum transfer, where the non relativistic approximation is justified.
The IA approach can be used for the evaluation of the nuclear cross section when the transferred momentum $|\mathbf{q}|$ exceeds ~ 400 MeV. It is based on the hypothesis that, when the momentum $\mathbf{q}$ is large enough, the nuclear target can be treated as a collection of individual nucleons. Furthermore, the particle produced in the final state and the residual system of $(A-1)$ nucleons are assumed to evolve independently. In the IA regime we can thus describe the scattering off a nucleus as the incoherent sum of the elementary processes that involve a single nucleon, as schematically illustrated in Fig. 3.1.

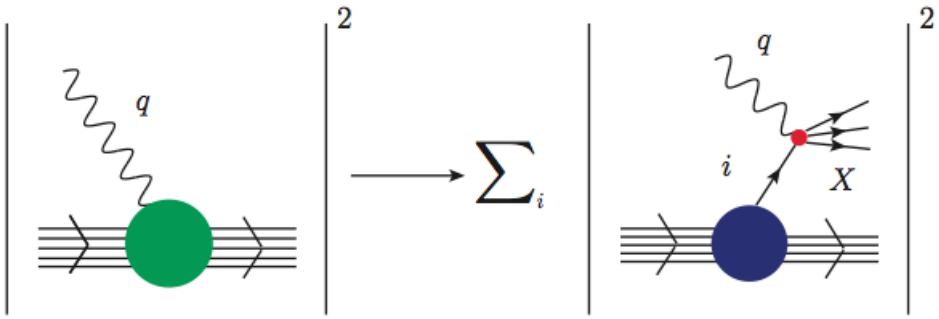

Figure 3.1: Schematic representation of lepton-nucleus scattering within the IA. The nuclear cross section is described as the incoherent sum of the elementary processes off the nucleons, and the residual system of $(A-1)$-nucleons acts as spectator.

The nuclear current can be written then as the sum of one-body currents

$$J_\mu \to \sum_i j_\mu^i \ , \tag{3.5}$$

and the generic hadronic final state can be written as the direct product of the hadronic state produced with momentum $\mathbf{p}'$ and the recoil system of $(A-1)$-nucleons with momentum $\mathbf{p_R}$

$$|X\rangle \to |x, \mathbf{p}'\rangle \otimes |R, \mathbf{p}_R\rangle \ . \tag{3.6}$$

It follows that

$$\sum_X \int \mathrm{d}^3\ p_X |X\rangle\langle X| \to \sum_x \int \mathrm{d}^3\ p' |x, \mathbf{p}'\rangle\langle x, \mathbf{p}'| \sum_R \int \mathrm{d}^3\ p_R |R, \mathbf{p}_R\rangle\langle R, \mathbf{p}_R| \ . \tag{3.7}$$

By inserting a completeness relation

$$\sum_N \int \mathrm{d}^3 p |N, \mathbf{p}\rangle\langle N, \mathbf{p}| = 1 \ , \tag{3.8}$$

the matrix element of Eq. (3.3) becomes

$$\begin{aligned}
\langle 0|J^A_\mu|X\rangle =& \sum_i \langle 0|j^i_\mu|x, \mathbf{p}'\rangle |R, \mathbf{p}_R\rangle = \\
=& \sum_i \sum_N \int \mathrm{d}^3 p \left(\frac{M}{\sqrt{|\mathbf{p}|^2 + M^2}} \right)^{\frac{1}{2}} \langle 0|R, \mathbf{p}_R\rangle |N, \mathbf{p}\rangle \langle N, \mathbf{p}|j^i_\mu|x, \mathbf{p}'\rangle = \\
=& \sum_i \sum_N \left(\frac{M}{\sqrt{|\mathbf{p}_R|^2 + M^2}} \right)^{\frac{1}{2}} \langle 0|R, \mathbf{p}_R\rangle |N, -\mathbf{p}_R\rangle \langle N, -\mathbf{p}_R|j^i_\mu|x, \mathbf{p}'\rangle \ .
\end{aligned} \tag{3.9}$$

Thus, the hadronic tensor in Eq. (3.3) can be rewritten as

$$\begin{aligned}
W^A_{\mu\nu} \propto & \sum_i \sum_{x,R} \sum_N \int \mathrm{d}^3 p' \mathrm{d}^3 p_R \frac{M}{\sqrt{|\mathbf{p}_R|^2 + M^2}} |\langle 0|R, \mathbf{p}_R\rangle |N, -\mathbf{p}_R\rangle|^2 \times \\
& \times \langle N, -\mathbf{p}_R|j^i_\mu|x, \mathbf{p}'\rangle \langle x, \mathbf{p}'|j^i_\nu|N, -\mathbf{p}_R\rangle \times \\
& \times \delta^{(3)}(\mathbf{q} - \mathbf{p}_R - \mathbf{p}') \delta(\omega + E_0 - E_R - E_{p'}) \ ,
\end{aligned} \tag{3.10}$$

where we split the δ-function of the quadri-momenta conservation, having considered the nucleus at rest. Moreover $E_R = \sqrt{|\mathbf{p}_R|^2 + M_R^2}$, being M_R the mass of the recoiling system. The energy conservation δ can be rewritten as

$$\delta(\omega + E_0 - E_R - E_{p'}) = \int \mathrm{d}E\ \delta(E - M + E_0 - E_R) \delta(\omega + M - E - E_{p'}) \ , \tag{3.11}$$

and we can define the spectral function

$$P(\mathbf{p}, E) = \sum_R |\langle 0|R, -\mathbf{p}\rangle |N, \mathbf{p}\rangle|^2 \delta(E - M + E_0 - E_R) \ , \tag{3.12}$$

which expresses the probability that, by removing a nucleon with momentum $\mathbf{p}$ from the nucleus, the residual system is left with an excitation energy E. Finally, we can rewrite the hadronic tensor as

$$\begin{aligned}
W^A_{\mu\nu} \propto & \sum_i \sum_{x,N} \int \mathrm{d}E\ \mathrm{d}^3 p'\ \mathrm{d}^3 p\ \frac{M}{E_p} P(\mathbf{p}, E) \langle N, \mathbf{p}|j^i_\mu|x, \mathbf{p}'\rangle \langle x, \mathbf{p}'|j^i_\nu|N, \mathbf{p}\rangle \times \\
& \times \delta^{(3)}(\mathbf{q} - \mathbf{p} - \mathbf{p}') \delta(\omega + M - E - E_{p'}) \ .
\end{aligned} \tag{3.13}$$

The above hadronic tensor can be written in terms of the elementary one for neutrino-nucleon scattering given by

$$\begin{aligned} W^i_{\mu\nu} =& \sum_{\sigma_i}\sum_x \int \frac{\mathrm{d}^3p'}{2E_{p'}2E_p}\ \langle N,\mathbf{p}|j^i_\mu|x,\mathbf{p}'\rangle\langle x,\mathbf{p}'|j^i_\nu|N,\mathbf{p}\rangle\times \\ &\times\delta^{(3)}(\mathbf{q}-\mathbf{p}-\mathbf{p}')\delta(\omega+M-E-E_{p'}) = \\ =& \sum_{\sigma_i}\sum_x \frac{1}{2E_{p'}2E_p}\ \langle N,\mathbf{p}|j^i_\mu|x,\mathbf{p}+\mathbf{q}\rangle\langle x,\mathbf{p}+\mathbf{q}|j^i_\nu|N,\mathbf{p}\rangle\delta(\omega+E_0-E_R-E_{p'}) = \\ =& \sum_{\sigma_i}\sum_x \frac{1}{2E_{p'}2E_p}\ \langle N,\mathbf{p}|j^i_\mu|x,\mathbf{p}+\mathbf{q}\rangle\langle x,\mathbf{p}+\mathbf{q}|j^i_\nu|N,\mathbf{p}\rangle\delta(\tilde{\omega}+E_p-E_{p'})\ , \end{aligned} \tag{3.14}$$

where we replaced $M-E=E_0-E_R$ in the second equality, while the quantity $\tilde{\omega}$, appearing in the third equality, is defined as

$$\tilde{\omega}=\omega+E_0-E_R-E_p\ . \tag{3.15}$$

Replacing $\omega\to\tilde{\omega}$ is equivalent to consider a rescaled momentum transfer, $q\to\tilde{q}=(\tilde{\omega},\mathbf{q})$, which takes into account the fraction of the transferred energy going into excitation energy E of the spectator system. Finally, we can rewrite

$$\frac{\delta(\tilde{\omega}+E_p-E_{p'})}{2E_{p'}}=\delta((p+\tilde{q})^2-M'^2)\ , \tag{3.16}$$

obtaining for the elementary hadronic tensor in Eq. (3.14)

$$W^i_{\mu\nu} = \sum_{\sigma_i}\sum_x \frac{1}{2E_p}\ \langle N,\mathbf{p}|j^i_\mu|x,\mathbf{p}+\mathbf{q}\rangle\langle x,\mathbf{p}+\mathbf{q}|j^i_\nu|N,\mathbf{p}\rangle\delta((p+\tilde{q})^2-M'^2)\ , \tag{3.17}$$

that is an expression equivalent to the one obtained for the scattering off a nucleon in Eq. (2.20), but dependent on the rescaled momentum transferred $\tilde{q}$ and on the momentum $p=(E_p,\mathbf{p})$. The above equation will then be parametrized as a function of five independent structure functions, as seen in the previous chapter, characteristic for each interaction channel.
The hadronic tensor, within the IA, finally becomes

$$W^{\mu\nu}_A = A\int \mathrm{d}^3p\ \mathrm{d}E\ \frac{M}{E_p}\ P(\mathbf{p},E)\ W^{\mu\nu}_i(\tilde{q},p)\ , \tag{3.18}$$

where A is the number of nucleons in the considered nucleus, and derives from the summation over N. Notice that the above expression is restricted to the special case of an isoscalar target. In the most general case we have

$$W^{\mu\nu}_A = \int \mathrm{d}^3p\ \mathrm{d}E\ \frac{M}{E_p}\ [ZP_p(\mathbf{p},E)\ W^{\mu\nu}_p(\tilde{q},p)+(A-Z)P_n(\mathbf{p},E)\ W^{\mu\nu}_n(\tilde{q},p)]\ , \tag{3.19}$$

with Z the number of the protons. In the isoscalar case it is possible to assume $P_p(\mathbf{p},E)=P_n(\mathbf{p},E)=P(\mathbf{p},E)$, with $W^{\mu\nu}_i=(W^{\mu\nu}_p+W^{\mu\nu}_n)/2$, obtaining Eq. (3.18) from Eq. (3.19).

Finally the cross section for the scattering off a nucleus reads

$$\frac{\mathrm{d}^2\sigma_{\nu A}}{\mathrm{d}E_\ell \mathrm{d}\Omega_\ell} = \sum_i \int \mathrm{d}E\ \mathrm{d}^3p\ P(E,\mathbf{p}) \frac{M}{E_p} \frac{1}{16\pi^2} \frac{\mathbf{k}'}{\mathbf{k}} \mathscr{C}^2 L_{\mu\nu} W_i^{\mu\nu} = \tag{3.20}$$
$$= \sum_i \int \mathrm{d}E\ \mathrm{d}^3p\ P(E,\mathbf{p}) \frac{M}{E_p} \frac{\mathrm{d}^2\sigma^i_{\nu N}}{\mathrm{d}E_\ell \mathrm{d}\Omega_\ell}$$

which is the convolution of the elementary cross section with the spectral function.

3.2 The Spectral Function

The spectral function, introduced in the previous section in Eq. (3.12), is proportional to the imaginary part of the two-point Green's function, describing the propagation of a nucleon in nuclear ground state [81, 82]. The two-point Green's function is defined as

$$G(\mathbf{p},E) = \langle\overline{0}|\frac{1}{H - E_0 - E - i\eta}|\overline{0}\rangle - \langle\overline{0}|\frac{1}{H - E_0 + E - i\eta}|\overline{0}\rangle \tag{3.21}$$
$$= G_h(\mathbf{p},E) + G_p(\mathbf{p},E)$$

where H is the nuclear hamiltonian, $|\overline{0}\rangle$ is its true ground state with energy E_0, such that

$$H|\overline{0}\rangle = E_0|\overline{0}\rangle\ . \tag{3.22}$$

The two components of the Green's function, G_p and G_h, describe the propagation of a nucleon sitting in a particle state, defined for $-E > \varepsilon_F$, and a hole state, defined for $-E < \varepsilon_F$, respectively, with ε_F the Fermi energy. The imaginary part of the Green's function is proportional to the spectral functions [83]

$$P_h(\mathbf{p},E) = \sum_N |\langle\overline{0}|a^\dagger_{\mathbf{p}}|\overline{N}_{A-1}\rangle|^2 \delta(E + E_0 - E_N^{A-1})\ , \tag{3.23}$$

$$P_p(\mathbf{p},E) = \sum_N |\langle\overline{0}|a_{\mathbf{p}}|\overline{N}_{A+1}\rangle|^2 \delta(E - E_0 + E_N^{A+1})\ , \tag{3.24}$$

where $|\overline{N}_{A\mp1}\rangle$ denotes the intermediate state of $A \mp 1$ particles with energy $E_N^{A\mp1}$ and $a^\dagger_{\mathbf{p}}$ is the creation operator of a particle with momentum $\mathbf{p}$. Eqs. (3.23) and (3.24) give the probability of leaving the nuclear system with an excitation energy E removing/adding a nucleon with momentum $\mathbf{p}$.
The spectral function defined in Eq. (3.12) is proportional to $G_h(\mathbf{p},E)$, so we have

$$P(\mathbf{p},E) = P_h(\mathbf{p},E)\ . \tag{3.25}$$

Studies on the use of a realistic spectral function have been performed for different kind of systems: three nucleon systems [84, 85, 86], oxygen [87], and symmetric nuclear matter [83, 88].
From the Källen–Lehman representation, one can rewrite the two-point Green's function as the sum of two different components, according to their energy dependence. The first part,

called *single–particle spectral function*, or mean–field component, includes the contribution of one–hole intermediate states, which exhibits a pole at $E = -e_{\mathbf{p}}$, being $e_{\mathbf{p}}$ the energy of a nucleon in the hole state with momentum $\mathbf{p}$. The width of the peak gives a measure of the lifetime of the hole state, and goes to zero as $e_{\mathbf{p}} \to \varepsilon_F$. The integration of the single–particle spectral function, $P_{1h}(\mathbf{p}, E)$, over the energy, gives the normalization of the hole state, $Z(\mathbf{p})$, which is reduced with respect of the unity, due to nucleon–nucleon correlations.
The second part, called *correlated spectral function*, $P_{corr}(\mathbf{p}, E)$, takes into account the contribution coming from dynamical nucleon–nucleon correlations, that is from n-hole–$(n-1)$-particle states. The leading contribution comes from two-hole–one-particle states. The energy dependence of the correlation part is such that it smoothly extends to large values of energy and momentum.
The spectral function can be described within the *Local Density Approximation* (LDA). In this framework, the spectral function is given by the combination of the mean-field contribution and the correlation part extracted from the nuclear-matter calculation and then adapted to the case of nuclei. The LDA can be used to evaluate a generic two-body function, when the dependence on the center mass coordinate is weak, which is the case of short-range correlations terms, being the relative distance small compared to the surface thickness.
When correlation effects are negligible, the spectral function is given by the mean field contribution, written in the form

$$P_{MF}(\mathbf{p}, E) = \sum_{\alpha} |\phi_\alpha(\mathbf{p})|^2 \delta(E - e_\alpha) \ , \tag{3.26}$$

where ϕ_α is the momentum space wave function for the particle state α, and e_α is its energy. To account for NN short range correlations, Eq. (3.26) becomes

$$P_{MF}(\mathbf{p}, E) = \sum_{\alpha} Z_\alpha \big|\phi_\alpha(\mathbf{p})\big|^2 F_\alpha(E - e_\alpha) \ , \tag{3.27}$$

where Z_α is a normalization constant which includes interactions not taken into account by the mean field approximation; $F_\alpha(E - e_\alpha)$ describes the energy dependence of the α-state, which will be broader than a δ-function due to finite lifetime of the single particle state.
The correlation part is given by

$$P_{corr}(\mathbf{p}, E) = \int \mathrm{d}^3 r \ \rho_A(\mathbf{r}) P^{MN}_{corr}(\mathbf{p}, E; \rho = \rho_A(\mathbf{r})) \ , \tag{3.28}$$

where $\rho_A(\mathbf{r})$ is the nuclear density distribution, $P^{MN}_{corr}(\mathbf{p}, E; \rho_A(\mathbf{r}))$ is the correlation part of the spectral function for infinite nuclear matter at density ρ.
Thus, in the LDA approach the spectral function is

$$P_{LDA}(\mathbf{p}, E) = P_{MF}(\mathbf{p}, E) + P_{corr}(\mathbf{p}, E) \tag{3.29}$$

with the normalization condition given by

$$\int \mathrm{d}^3 p \ \mathrm{d}E \ P_{LDA}(\mathbf{p}, E) = 1 \ . \tag{3.30}$$

As a final remark, we mention that, since the correlation component arises from short-range dynamics, it gives rise to the occurrence of strongly correlated nucleons pairs, not expected to be affected by finite size and shell effects. This assumption is supported by theoretical results of the nucleon momentum distribution, defined as

$$n(\mathbf{p}) = \int \mathrm{d}E \; P(\mathbf{p}, E) \tag{3.31}$$

and, in Fig. 3.2, it is shown the quantity $n(\mathbf{p})/A$ that becomes independent from A in the kinematical region where $|\mathbf{p}| \gtrsim 350$ MeV, which is most sensitive to short-range correlations.

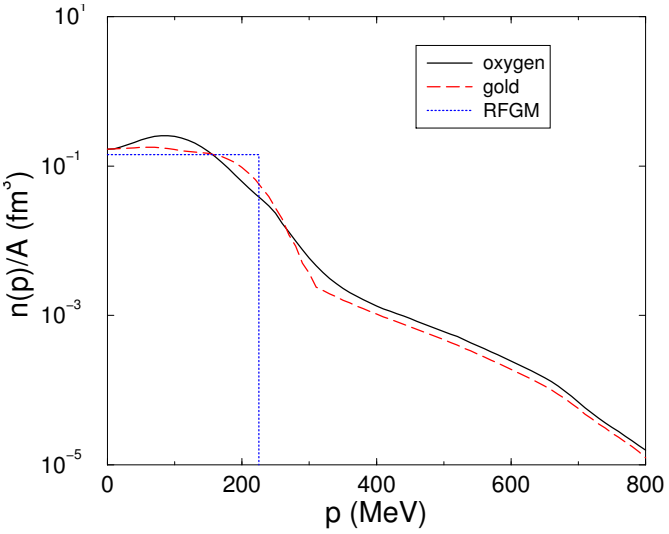

Figure 3.2: Behavior of the nucleon momentum distribution normalized to the number of nucleons for oxygen (solid line) and for gold (dashed line), from Ref. [54]. The step function corresponds to the Fermi distribution with momentum $p_F = 225$ MeV and binding energy $E = 25$ MeV.

It is also important to mention that a widely used model of the spectral function is based on the Relativistic Fermi Gas Model (RFGM), which considers the nucleus as a degenerate gas of fermions

$$P_{RFGM}(\mathbf{p}, E) = \frac{6\pi^2}{p_F^3}\theta(p_F - \mathbf{p})\delta(E_p - E_B - E) \; , \tag{3.32}$$

where p_F is the Fermi momentum and E_B is the binding energy.
However, the Fermi gas model does not describe particles which populate states with momentum above the Fermi sphere, originating from nucleon-nucleon correlations. Due to correlations, the number of nucleons with $E < E_F$ and $|\mathbf{p}| < p_F$ decreases, and the contribution coming from correlated nucleon pairs with $E > E_F$ and $|\mathbf{p}| > p_F$ becomes non vanishing.
To evaluate the typical energy scale of nuclear correlations, consider a pair of nucleons with momenta $\mathbf{k_1}$ and $\mathbf{k_2}$ much larger than the Fermi momentum ($p_F \sim 250$ MeV). In the rest-frame of the nucleus, assuming the residual system of $(A-2)$-nucleons with low momentum, we have $\mathbf{k_1} \sim -\mathbf{k_2} = \mathbf{k}$. Thus, the emission of a nucleon with high momentum

k will leave the residual system with a nucleon in the continuum, and it requires an energy ($\mathcal{O}(100)$ MeV) given by

$$E \sim E_{th} + \frac{\mathbf{k}^2}{2m} \,, \tag{3.33}$$

where E_{th} is the two-nucleon emission threshold.

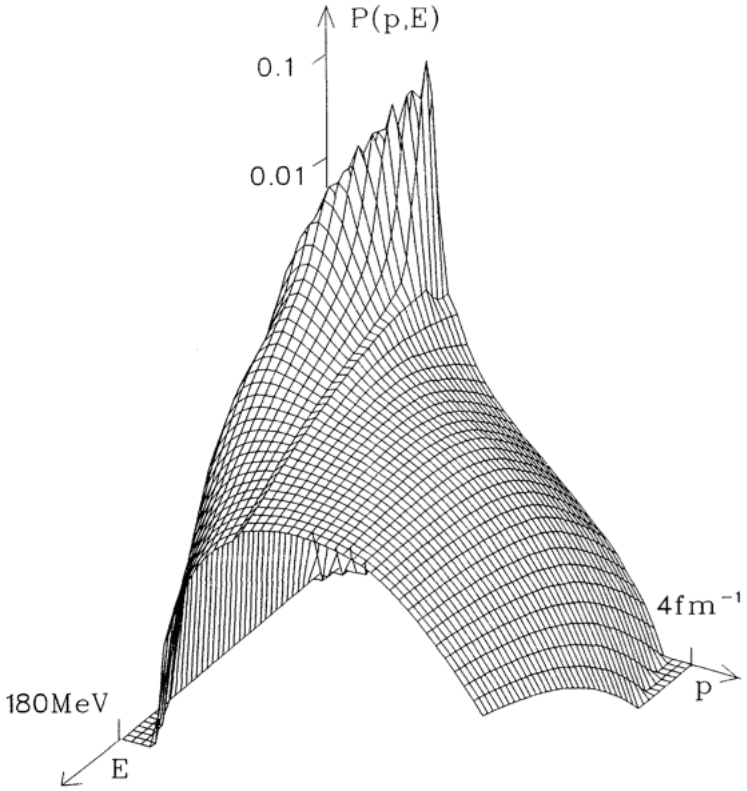

Figure 3.3: Nucleon spectral function for isospin-symmetric nuclear matter, from Refs. [83, 89].

This is also visible in Fig. 3.3, where the spectral function for isospin-symmetric nuclear matter is shown [83, 89]. The peaks correspond to the single particle states, and the broad background is due to n-hole–$(n-1)$-particle, characterized by having a nucleon excited to the continuum.

The use of a realistic Spectral Function obtained from the formalism of NMBT for the description of the nuclear response has been validated through the comparison with data from electron scattering experiment off nuclear targets, such as Carbon and Oxygen. The results obtained for the description of the kinematical region dominated by QE interactions, reproduce the experimental data with an accuracy of few percent [55, 56]. The results, taken from Ref. [90], are shown in Fig. 3.4, for different electron kinematics and Carbon as nuclear target.

The cross sections obtained in the IA formalism are shown with the solid line, where effects due to *Final State Interactions* (FSI) between the struck particle and the spectators have

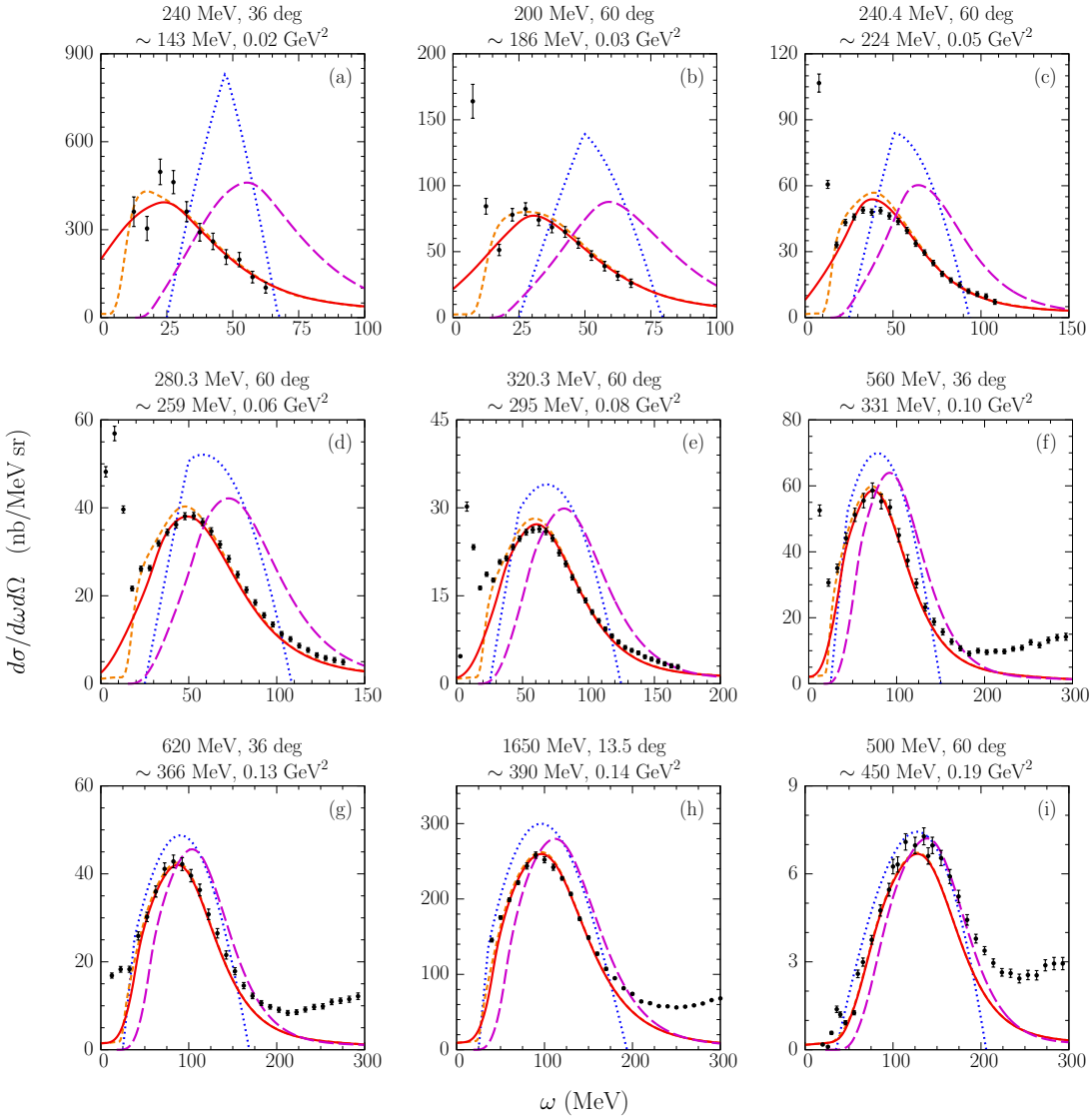

Figure 3.4: Double differential cross section as a function of the energy transferred ω, for electron-carbon scattering, taken from Ref. [90]. The solid lines and the short-dashed lines are obtained using the IA formalism including the FSI. They differ in the implementation of the Pauli Blocking. The dotted lines are the results for the RFMG and the long dashed lines are obtained using the IA alone. The data are taken from Refs. [91, 92, 93]. The labels indicate the beam energy, the incident scattering angle, and the values of $|\mathbf{q}|$ and Q^2 at the QE peak.

been included through the following prescription

$$\frac{\mathrm{d}^2\sigma^{FSI}}{\mathrm{d}\Omega\mathrm{d}\omega} = \int \mathrm{d}\omega' f_q(\omega-\omega')\frac{\mathrm{d}^2\sigma^{IA}}{\mathrm{d}\Omega\mathrm{d}\omega'} \ , \tag{3.34}$$

where the folding function f_q, depends on the in medium NN scattering cross section, as well as on the one- and two-nucleon density distributions [90, 94]. In the absence of FSI, the folding function reduces to a δ-function and the pure IA is recovered.
For comparison also the behavior of the cross section obtained within the FGM is shown

with the dotted line, while the use of the pure IA is represented by the long-dashed line. The short-dashed and solid lines show both the cross section in the IA scheme including the FSI, but using two different approaches for the treatment of the Pauli Blocking [90], which specifies the phase space available to the knocked-out particle. It clearly appears that the description of the nuclear dynamics within the spectral function approach, allows to reproduce quasi elastic electron scattering data with good accuracy over a broad kinematical region.

3.3 Neutrino-Carbon cross section

In this section we present the results obtained for the muon neutrino cross section on ^{12}C [79]. The calculations have been performed using the formalism described in the previous sections and the spectral function of Ref. [95], including the different interaction channels discussed in Chapter 2.

The double differential cross section has been computed according to Eq. (3.20), and we report in Figs. 3.5 and 3.6 the results obtained for the neutrino energy at $E_\nu = 1$ GeV and $E_\nu = 1.5$ GeV, with $\theta_\mu = 30°$, being the angle of the outgoing charged lepton.

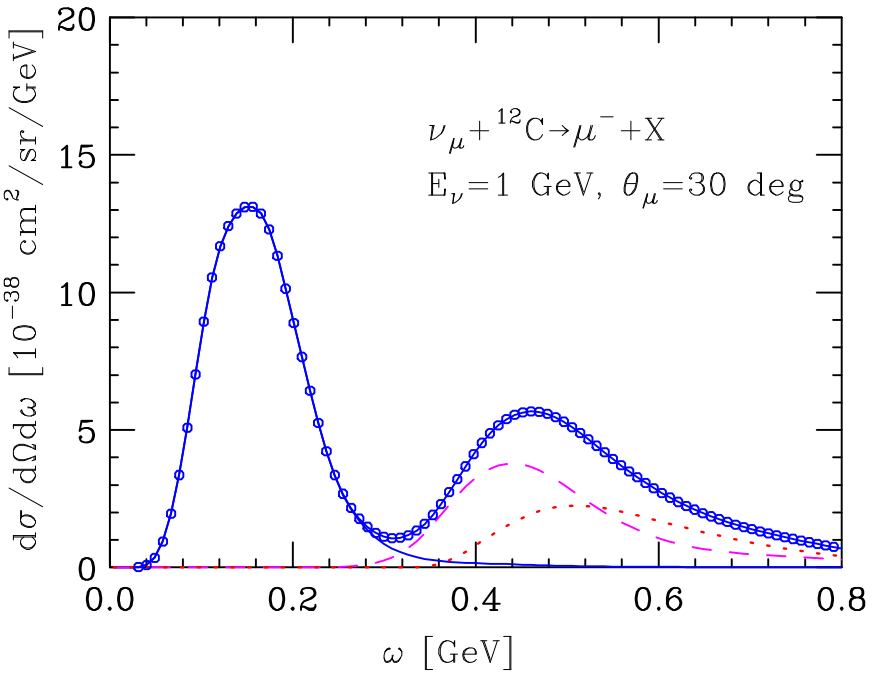

Figure 3.5: Double differential cross section for ν_μ on ^{12}C for $E_\nu = 1$ GeV and $\theta_\mu = 30°$. The blue circles represent the total cross section given by the sum of QE interaction (solid line), resonance production (dashed line) and DIS (dotted line). Note that in this kinematics only the Δ resonance plays a significant role.

At the kinematics reported in Fig. 3.6 it is also visible the contribution coming from the second resonance region and it is represented by the dashed line.

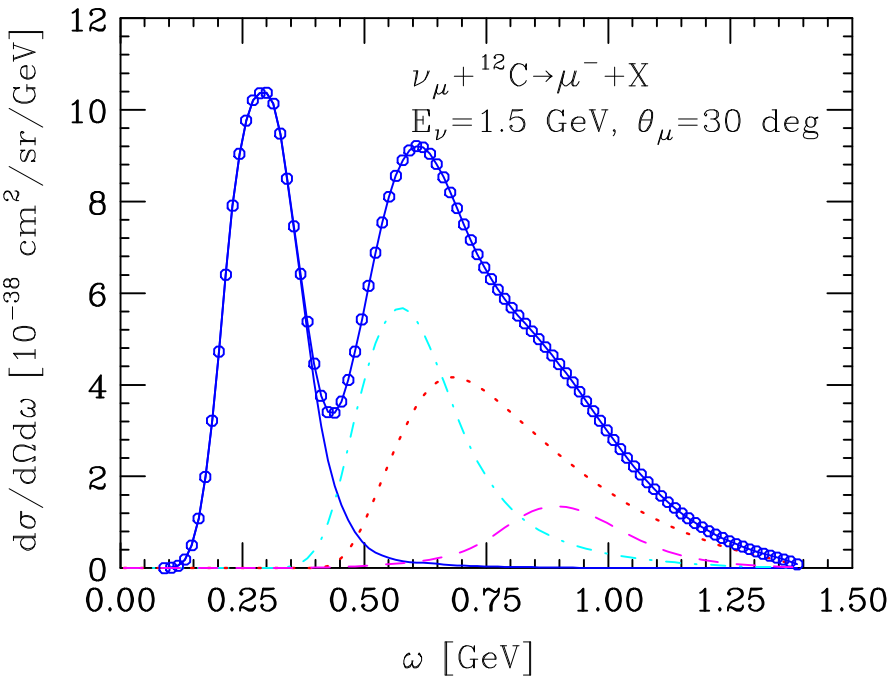

Figure 3.6: The same as Fig. 3.5, but for $E_\nu = 1.5$ GeV. At this kinematics is visible also the contribution coming from the second resonance region represented by the dashed line, while the Δ is represented by the dot-dashed line.

To obtain the total cross section we also consider the distribution in the four-momentum transferred Q^2, given by

$$Q^2 = 2E_\nu E_\mu \left(1 - \frac{|\mathbf{k}_\mu|}{E_\mu}\cos\theta_\mu\right) - m_\mu^2 \ , \tag{3.35}$$

where E_μ, $\mathbf{k}_\mu$ and m_μ are the energy, the three-momentum and the mass of the outgoing muon, respectively. Thus the differential cross section in Q^2 is given by

$$\frac{d\sigma}{dQ^2} = 2\pi \int d\cos\theta_\mu \frac{d^2\sigma}{d\Omega_\mu dE_\mu} \delta\left(Q^2 - 2E_\nu E_\mu \left(1 - \frac{|\mathbf{k}_\mu|}{E_\mu}\cos\theta_\mu\right) + m_\mu^2\right) \ . \tag{3.36}$$

The results obtained for the differential cross section of Eq. (3.36), for the same neutrino energies used before, are reported in Figs. 3.7 and 3.8. All Q^2 distributions are peaked at low Q^2 (~ 0.2 GeV^2). As pointed out in Section 2.4, the PDFs used to describe the DIS in this Q^2 region are not available, thus we used distributions keeping Q^2 fixed at the lowest value available.

Finally, the total cross section as a function of the neutrino energy E_ν is reported in Fig. 3.9. The two panels show the total cross section for ν_μ on ^{12}C divided by the neutrino energy (upper panel), and the cross sections in the different interaction channels considered (lower panel). For comparison, in the upper panel, the experimental points obtained by the NOMAD Collaboration [49] are also shown with black diamonds: they are in reasonable agreement with our theoretical results for the DIS channel. However, the total cross section overestimates the data and exhibits a decreasing behavior when the energy increases.

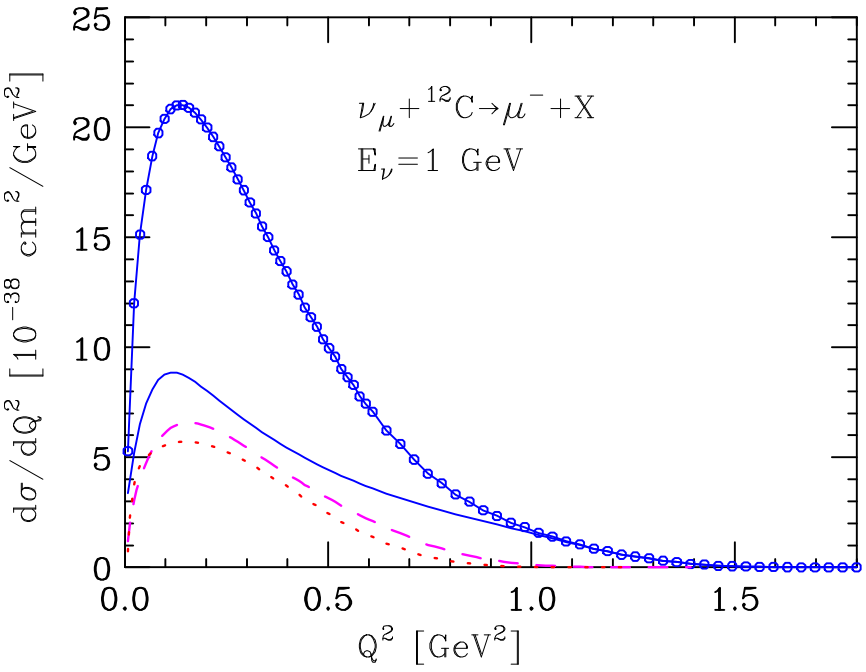

Figure 3.7: Q^2 distribution of the differential cross section, for $E_\nu = 1$ GeV. The total differential cross section is represented by the blue circles and is given by the sum of QE channel (solid line), resonances production (dashed line) and DIS (dot-dashed line).

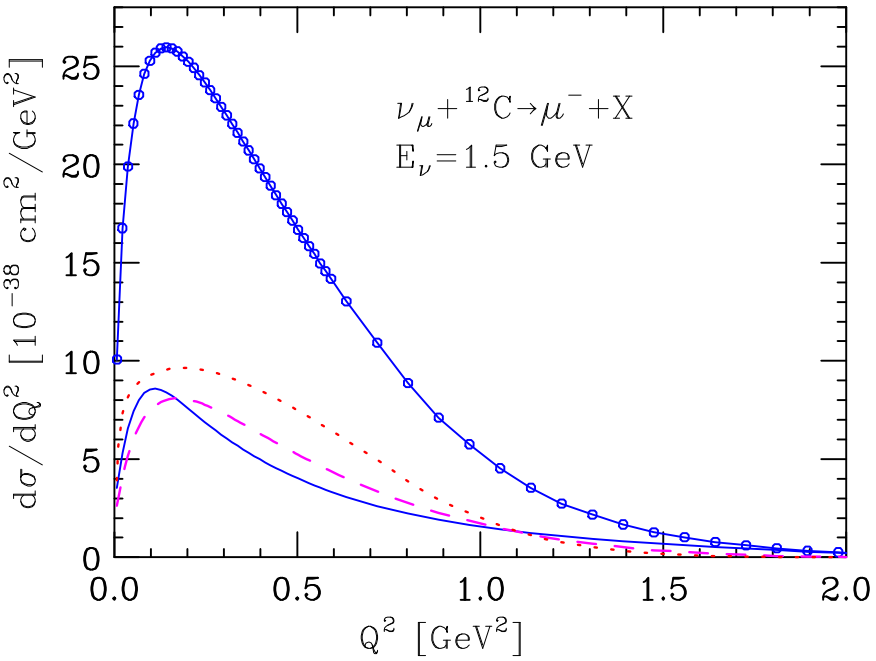

Figure 3.8: The same as Fig. 3.7, but for $E_\nu = 1.5$ GeV.

This feature is likely to be ascribed to a double counting between DIS and resonances contribution.

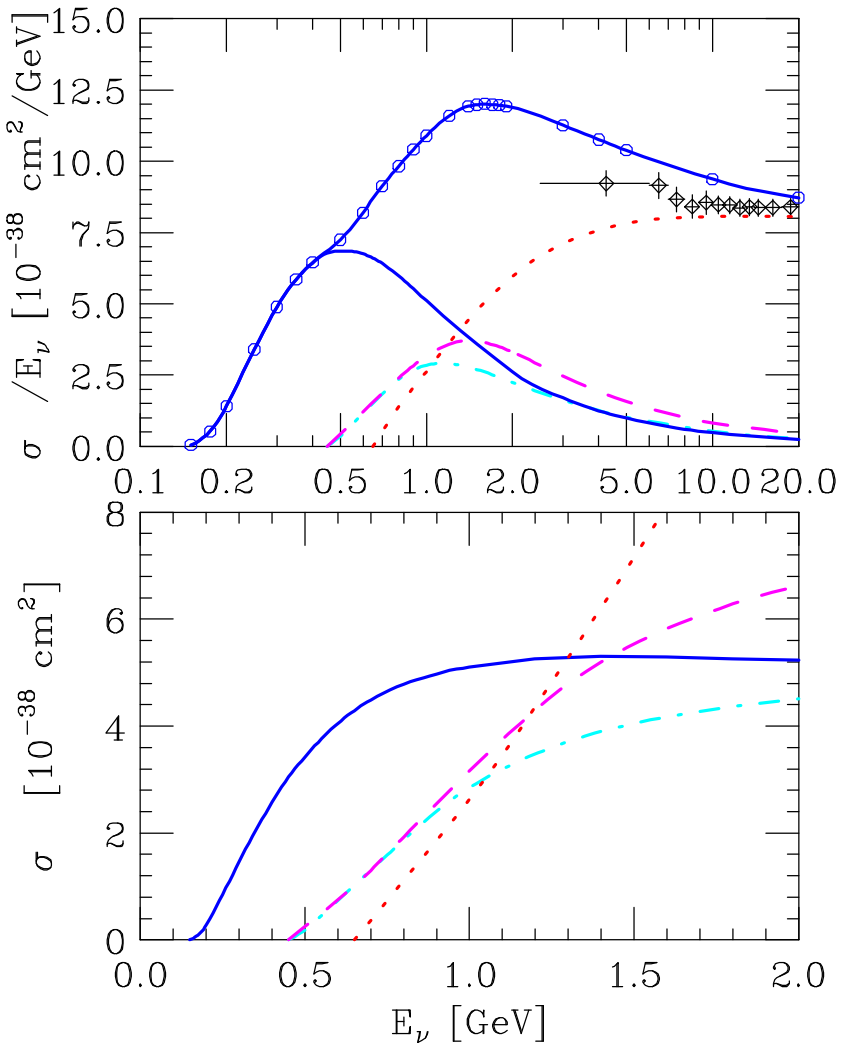

Figure 3.9: Total ν_μ cross section on ^{12}C. The upper panel represents the total cross section divided by the neutrino energy. The lower panel shows the cross sections in the different interaction channels considered. The blue circles represent the total cross section, the solid line the contribution of QE interactions, the dot-dashed line the Δ-resonance production, the dashed line the contribution of the resonances from the second region plus the Δ, and the dotted line is the DIS. For comparison in the upper panel are also shown the experimental data, with black diamonds, obtained by the NOMAD experiment [49].

Unfortunately, a truly model independent separation of these two reaction mechanisms does not appear to be achievable, and the problem of double counting clearly manifests itself at proton level. In fact, the electron-proton cross section obtained using the structure functions of Refs. [63, 73], employed in our study, turns out to by sizably larger than the Jefferson Lab data, collected in a kinematical region extending from the Δ-production threshold up to $W^2 \lesssim 4$ GeV^2 [96]. The authors of Ref. [74] circumvented the prob-

lem of double counting carrying out a *global* fit, in which the data were modeled by the *product*—rather than the sum—of a smooth universal background and a modulating function, describing the resonance peaks.

Chapter 4

Neutrino energy reconstruction

Long-baseline experimental searches of neutrino oscillations largely rely on the capability of pinning down the energy profile of the oscillation probability. Thus, the reconstruction technique employed for the study of the incoming neutrino energy is a key element of the oscillation analysis.

The kinematic method of energy reconstruction is based on the assumption that the beam particle interacts with a single nucleon at rest, bound with constant energy, and that no other nucleons are knocked out from the nucleus. This reconstruction scheme is largely used by experiments with beam flux peaked around $600 - 800$ MeV, such as T2K [97] and MiniBooNE [98]. The kinematic reconstruction is mostly applied to QE events, identified by the absence of pions in the final state, that provide the dominant contribution to the total cross section at these energies. However, it necessarily involves hypotheses on the reaction mechanism. For instance, processes involving two-nucleon currents, final-state interactions, and nucleon-nucleon correlations give rise to the appearance of more complex final states, featuring more than one nucleon excited to the continuum. These events can be misidentified to be QE, thus more complex methods, involving realistic models of nuclear dynamics, are needed.

As alternative to Cherenkov detectors, calorimeters measuring the visible energy associated with each event – i.e., the energy deposited by the final-state particles – have been proposed as effective devices, allowing for an accurate neutrino-energy reconstruction. Calorimeters are presently being used in the MINOS [99] and NOνA [100] experiments. The calorimetric technique obviously rests on the ability of fully reconstructing the final state, which largely depends on the detector design and performance. Nuclear effects also play a role, as they may lead to a sizable amount of missing energy, hindering the reconstruction of E_ν. For example, if a pion produced at the elementary interaction vertex is absorbed in the spectator system, in general its energy is not deposited in the calorimeter.

In this Chapter we describe two reconstruction techniques, the calorimetric and the kinematic one. We will describe how they have been implemented to analyze neutrino events produced with the Monte Carlo event generator GENIE [101]. We considered two different approaches for energy reconstruction: a *perfect reconstruction*, in which all produced particles are detected and their true energies are measured, and a *realistic reconstruction*, where we assumed detection efficiencies, thresholds and finite detector resolution. Notice that the assumed detector capabilities can be currently considered optimistic, compared to those achieved in existing experiments; however, they might be reached in future detectors.

The analysis of neutrino events within the calorimetric and kinematic reconstruction allowed us to generate *Migration Matrices* (MM), M_{ij}, that define the probability that an event with a true neutrino energy E_j in the jth bin ends up being reconstructed as E_i in an energy bin i. Such matrices will be described in the last section of this chapter.

4.1 Reconstruction methods

Consider charged-current neutrino scattering off a nuclear target

$$\nu_\ell(k) + A \to \ell^-(k') + X \ , \tag{4.1}$$

where the neutrino, with four momentum $k = (E_\nu, \mathbf{k})$, scatter off the target A leading to a final state with a lepton of four momentum $k' = (E_\ell, \mathbf{k}')$. The general hadronic final state X can be described by n nucleons, knocked out from the nucleus, and m mesons produced by the interaction, with four-momentum $p' = (E_{\mathbf{p}'_i}, \mathbf{p}'_i)$ and $h' = (E_{\mathbf{h}'_j}, \mathbf{h}'_j)$ being $1 \leq i \leq n$ and $1 \leq j \leq m$, respectively[1].
Applying energy and momentum conservation, one gets

$$E_\nu + M_A = E_\ell + E_{A-n} + \sum_i^n E_{\mathbf{p}'_i} + \sum_j^m E_{\mathbf{h}'_j} \ , \tag{4.2}$$

$$\mathbf{k} = \mathbf{k}' - \mathbf{p} + \sum_i^n \mathbf{p}'_i + \sum_j^m \mathbf{h}'_j \ , \tag{4.3}$$

where M_A is the mass of the nuclear target, $-\mathbf{p}$ is the recoil momentum of the system and E_{A-n} represents the energy of the residual system of $(A-n)$-nucleons, that can be expressed as

$$E_{A-n} = M_A - nM + E + T_{A-n} \ , \tag{4.4}$$

where M is the nucleon mass, E the excitation energy of the system and T_{A-n} the recoil energy. Using Eqs. (4.2) and (4.4), it follows that

$$E_\nu = E_\ell - M_A + M_A - nM + E + T_{A-n} + \sum_i^n E_{\mathbf{p}'_i} + \sum_j^m E_{\mathbf{h}'_j} \ ,$$

$$E_\nu = E_\ell + E + T_{A-n} + \sum_i^n (E_{\mathbf{p}'_i} - M) + \sum_j^m E_{\mathbf{h}'_j} \ . \tag{4.5}$$

Since the nucleons are knocked out from the nucleus, they participate in the energy conservation through their kinetic energy, while mesons are produced by neutrino-nucleus interaction and their total energy enters the formula. Given that multi-nucleon processes exhibit a rather weak energy dependence, the quantity $\epsilon_n = E + T_{A-n}$ is usually approximated by a constant, obtained replacing E and T_{A-n} with the average values

$$< E > = \int E \ P(\mathbf{p}, E) \ \mathrm{d}^3p \ \mathrm{d}E \ , \tag{4.6}$$

$$< T_{A-n} > = \frac{1}{2M_R} \int |\mathbf{p}|^2 \ P(\mathbf{p}, E) \ \mathrm{d}^3p \ \mathrm{d}E \ , \tag{4.7}$$

[1] See Appendix A for details on the notation.

where M_R is the mass of the residual system and $P(\mathbf{p}, E)$ is the spectral function introduced in Section 3.2. These considerations can be cast together in order to obtain the neutrino energy in the so called *calorimetric method*

$$E_\nu^{\text{cal}} = \epsilon_n + E_\ell + \sum_i^n (E_{\mathbf{p}'_i} - M) + \sum_j^m E_{\mathbf{h}'_j} \ . \tag{4.8}$$

In principle this reconstruction scheme can be used for any type of charged current interaction. However, the ability to reconstruct the hadronic final state in the most accurate way is a huge experimental challenge; neutrons, for instance, typically escape detection and any undetected meson will result as an energy underestimation equal, at least, to the pion mass.
Through the knowledge of the invariant hadronic mass squared, given by

$$W^2 = \left(\sum_i^n E_{\mathbf{p}'_i} + \sum_j^m E_{\mathbf{h}'_j} \right)^2 - \left(\sum_i^n \mathbf{p}'_i + \sum_j^m \mathbf{h}'_j \right)^2 \tag{4.9}$$

by replacing Eq. (4.9) in Eqs. (4.2-4.3), we can obtain[2] the neutrino energy given by

$$E_\nu = \frac{W^2 - m_\ell^2 + 2E_{\mathbf{p}}E_\ell - (E_{\mathbf{p}}^2 - \mathbf{p}^2) - 2\mathbf{p}\cdot\mathbf{k}'}{2(E_{\mathbf{p}} - E_\ell + |\mathbf{k}'|\cos\theta_\ell - |\mathbf{p}|\cos\theta_{\mathbf{p}})} \ , \tag{4.10}$$

with $E_{\mathbf{p}} = M_A - E_{A-n}$, m_ℓ is the lepton mass, $|\mathbf{p}|\cos\theta_{\mathbf{p}} = \mathbf{p}\cdot\mathbf{k}/E_\nu$ and $|\mathbf{k}'|\cos\theta_\ell = \mathbf{k}'\cdot\mathbf{k}/E_\nu$.
In the following, the application of the above formula is linked to some assumptions: to neglect the recoil momentum $|\mathbf{p}|$ and to approximate the energy of the residual system with a constant, that is setting $E_{\mathbf{p}} = nM - \epsilon_n$. Under these assumptions, the reconstruction formula can be expressed as

$$E_\nu^{\text{kin}} = \frac{W^2 - m_\ell^2 + 2(nM - \epsilon_n)E_\ell - (nM - \epsilon_n) - 2\mathbf{p}\cdot\mathbf{k}'}{2(nM - \epsilon_n - E_\ell + |\mathbf{k}'|\cos\theta_\ell)} \ , \tag{4.11}$$

where E_ν^{kin} represents the neutrino energy reconstructed via the *kinematic method*, mostly applied to processes with single nucleon knocked-out without pions[3], where the invariant mass assumes the value of the nucleon mass $W^2 = M^2$. This reconstruction method suffers from the lack of knowledge of the undetected hadrons in the final state. For example, when a produced pion is absorbed or undetected the reconstructed neutrino energy is underestimated at least by $\sim 300 - 350$ MeV (see Figs. 6 and 7 of Ref. [102]).
In this Thesis, the reconstruction via the lepton kinematic variables has been performed using Eq. (4.11), assuming single nucleon knocked out events regardless of the actual number of nucleons in the final state. Furthermore, we assumed the invariant squared mass W^2 to be equal to the nucleon squared mass for meson-less events and to M_Δ^2 for events with at least a meson detected in the final state, being $M_\Delta = 1.232$ GeV the mass of the Δ-resonance, and the average single-nucleon separation energy ϵ_n is fixed to 34 MeV.
For the sake of completeness, the neutrino energy can also be reconstructed using the momentum conservation, exploited in Eq. (4.3), multiplied by a factor $\mathbf{k}/E_\nu$

[2] See Appendix D.

[3] This is due to the difficulties linked to the accuracy in the determination of the invariant hadronic mass.

$$E_\nu = |\mathbf{k}'|\cos\theta - |\mathbf{p}|\cos\theta_{\mathbf{p}} + \sum_i^n |\mathbf{p}'_i|\cos\theta_i + \sum_j^m |\mathbf{h}'_j|\cos\theta_j \ , \tag{4.12}$$

with $|\mathbf{p}'_i|\cos\theta_i = \mathbf{p}'\cdot\mathbf{k}/E_\nu$ and $|\mathbf{h}'_j|\cos\theta_j = \mathbf{h}'_j\cdot\mathbf{k}/E_\nu$. Eq. (4.12) can be further simplified with the same assumption used before, that is neglecting the recoil momentum

$$E_\nu = |\mathbf{k}'|\cos\theta + \sum_i^n |\mathbf{p}'_i|\cos\theta_i + \sum_j^m |\mathbf{h}'_j|\cos\theta_j \ , \tag{4.13}$$

which has been employed by the NOMAD Collaboration [103] for events with single nucleon knockout.

4.2 Event generation

Neutrino events have been produced using the Monte Carlo event generator GENIE [101]. It is a platform for neutrino events simulation that includes the most relevant scattering processes from several MeV to hundred GeV.

GENIE is employed in data analysis by a number of neutrino experiments [104], as well as in phenomenological estimates of the impact of nuclear effects on the determination of oscillation parameters, following the pioneering studies carried out by the authors of Ref. [105].

The default nuclear model employed for all kind of processes is the RFGM. The oscillation analysis, described in the next chapter, has been done considering the additional νT package used to generate neutrino events [106]. This allowed us to replace the RFGM by the Spectral Function approach for the description of quasi-elastic interactions.
In our analysis we considered quasi-elastic interaction, two-particle two-hole ($2p2h$) processes, which describe multinucleon mechanisms involving more than one nucleon excited to the continuum, and resonant and non-resonant pion production. In the QE sector the default model is the RFG model of Bodek and Ritchie [74], with a modified version which incorporates short range nucleon-nucleon correlations.
The resonant pion production is considered for $W \leq 1.7$ GeV within the Rein and Sehgal model [107], considering 16 resonances but neglecting the interference between them.
The contribution of non-resonant processes, classified in GENIE as DIS, is calculated following the method of Bodek and Yang [108]. Two-nucleon knockout ($2p2h$) events are simulated in GENIE using the procedure of Dytman[4] [109], obtained modifying and extending the one of Ref. [110], derived for electron scattering. For completeness, in Figs. 4.1 and 4.2, we show the cross sections used in these works, for ν_μ and $\overline{\nu}_\mu$ respectively, in charged current on ^{12}C.

[4] In this model the $2p2h$ process is modeled using a gaussian distribution to fill the dip region of electron scattering inclusive cross section data between the QE peak and the peak of the Δ-resonance.

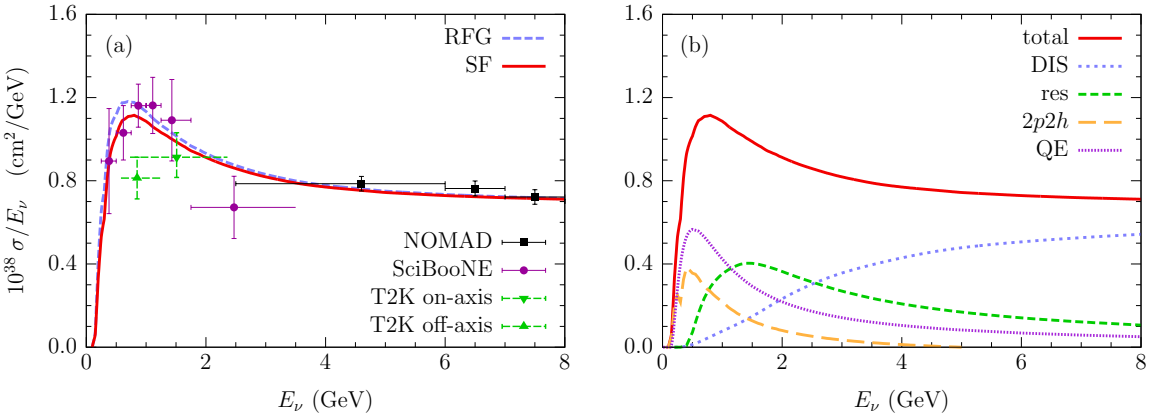

Figure 4.1: Inclusive ν_μ cross section in CC per nucleon, divided by the neutrino energy. The cross section is obtained using GENIE 2.8.0 +νT. Panel (a): Comparison of the total cross section using SF approach and the RFGM with solid and dashed lines, respectively. The data points shown for comparison are taken from NOMAD [49] (using carbon target), SciBooNE [50] and T2K [43, 111] (using hydrocarbon target). Panel (b): Breakup into the different interaction channels considered: QE (purple line), 2p2h (orange line), resonance production (green line) and DIS (blue line).

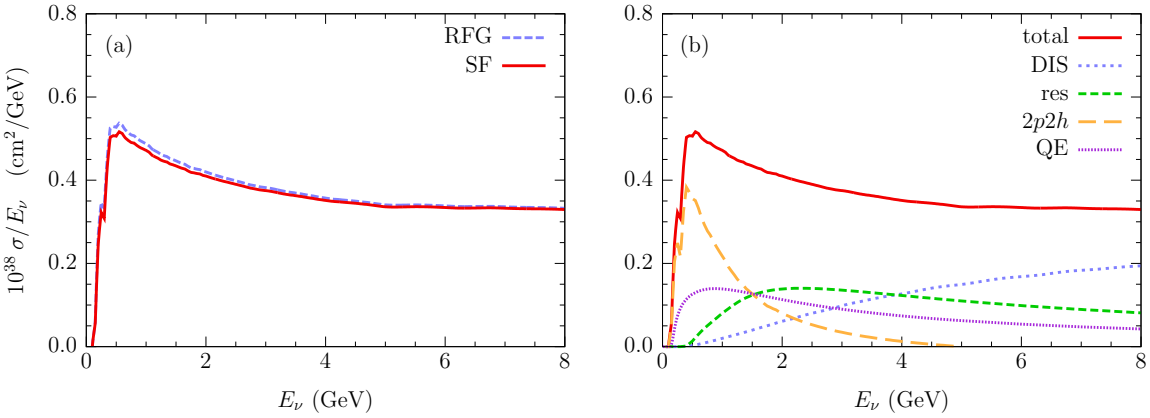

Figure 4.2: Same as Fig. 4.2, but for $\overline{\nu}_\mu$ cross section.

In the figures the panels indicated with (a) show the comparison between the total cross sections obtained using the SF and the RFGM for the description of QE interactions. In the case of the neutrino cross section the results are compared to the experimental data for carbon extracted from NOMAD [49], and for hydrocarbon from SciBooNE [50] and T2K [43, 111]. In the panels indicated with (b) it is shown the breakup into the different interaction channels considered.

To conclude, we show in Fig. 4.3 the energy contribution to the (anti-)neutrino energy coming from the different particles produced in the final state.

We can see that in the QE range, most of the contribution comes from nucleons, protons in the case of neutrino interaction and neutrons for anti-neutrino interaction. In the region of

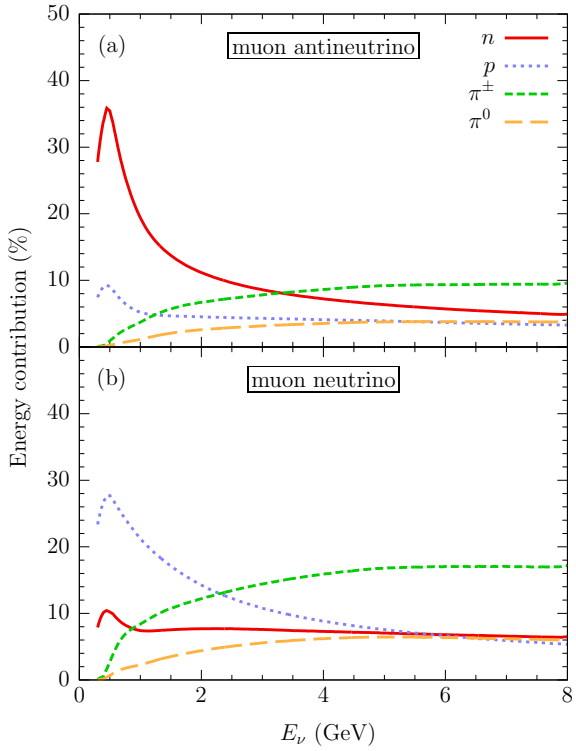

Figure 4.3: Energy contribution coming from the different particles produced in the final state for muon anti-neutrino (panel (a)) and muon neutrino (panel (b)) interaction. The solid red line is for neutrons, the blue dotted line for protons, the green dashed line for charged pions and the long dashed line for neutral pions.

resonant and non-resonant pion production most of the contribution comes from charged pions. Finally, for (anti-)neutrino energies such that $E_\nu \gtrsim 1.4$ GeV, neutrons contribute less than $\sim 15\%$ to the total (anti-)neutrino energy.

4.3 Considered detector effects

As pointed out in the introduction of this chapter, neutrino events produced with GENIE have been analyzed within two different extreme scenarios, that is

- *Perfect Scenario*: all the produced particles are observed with their measured energies equal to the true ones.
- *Realistic Scenario*: the measured energies and angles are smeared with respect to the true ones by a finite detector resolution. The detection efficiencies and thresholds on produced particles are taken into account.

In both configurations we assumed neutrons to escape detection.
The detection thresholds used correspond to the measured kinetic energy of 20 MeV for mesons and 40 MeV for protons. For instance, for the comparison with the values used in existing experiments, NOMAD and MiniBooNE collaborations were able to detect protons of kinetic energy above $\sim$ 50 MeV [112], and for future experiment with liquid argon

detectors ~ 40 MeV is expected [113].
We assumed efficiencies to be energy independent for simplicity. The chosen values can be considered optimistic compared to those achieved in existing detectors [112, 114, 115], and we set 60% for π^0's, 80% for other mesons, and 50% for protons. We also assumed that the charged lepton is always detected. Effects of the finite detector resolution have been considered, using a gaussian smearing centered around the *true* value x_{true}

$$f(x_{meas}) = \frac{1}{\sqrt{2\pi}\sigma(x_{true})} \exp\left[-\frac{1}{2}\left(\frac{x_{meas} - x_{true}}{\sigma(x_{true})}\right)^2\right] \tag{4.14}$$

where x_{meas} is the observable under study. The leptonic variables for muons [116] and for electrons [100, 117] are smeared using

$$\sigma(|\mathbf{k}'_\mu|) = 0.02|\mathbf{k}'_\mu|, \qquad \sigma(\theta_\mu) = 0.7^\circ, \qquad \text{Muon} \tag{4.15}$$
$$\sigma(E_e) = 0.10E_e, \qquad \sigma(\theta_e) = 2.8^\circ, \qquad \text{Electron} \tag{4.16}$$

For other particles the only variable smeared is the energy. For neutral pions and other hadrons the functions applied are

$$\frac{\sigma(E_{\pi^0})}{E_{\pi^0}} = \max\left\{\frac{a_{\pi^0}}{\sqrt{E_{\pi^0}}}, \frac{b_{\pi^0}}{E_{\pi^0}}\right\}, \qquad \text{with} \qquad a_{\pi^0} = 0.107,\ b_{\pi^0} = 0.020 \tag{4.17}$$
$$\frac{\sigma(E_h)}{E_h} = \max\left\{\frac{a_h}{\sqrt{E_h}}, b_h\right\}, \qquad \text{with} \qquad a_h = 0.145,\ b_h = 0.067\ . \tag{4.18}$$

where the energies are in GeV, and the values of a and b are taken from Refs. [99, 116]. Notice that the hadron energy resolutions applied in our analysis can be considered optimistic, as they are to be compared to

$$\frac{\sigma(E_{\pi^0})}{E_{\pi^0}} = 2\sqrt{\frac{a^2_{\pi^0}}{E_{\pi^0}} + \frac{b^2_{\pi^0}}{E^2_{\pi^0}}} \qquad \text{and} \qquad \frac{\sigma(E_h)}{E_h} = 2\sqrt{\frac{a_h^2}{E_h} + b_h^2} \tag{4.19}$$

achieved in the MINOS [99] and MINERvA [116] experiments.

4.4 Migration matrices

The reconstruction of neutrino events within the calorimetric and the kinematic methods, using two different assumptions for particles detection (*perfect reconstruction* and *realistic reconstruction*), allowed us to produce Migration Matrices, M_{ij}, whose columns are the probability distribution functions (PDFs) for a neutrino interaction X at the true energy in the ith bin to be reconstructed with an energy in the jth bin. The observed event distribution, accounting for detector effects, can then be computed as

$$N_i^{tot} = \sum_X \sum_j M_{ij}^X N_j^X \tag{4.20}$$

where X represents the interaction channel, i and j refer to the energy bins, and N_j^X is the number of events for the interaction channel X in the jth bin, computed without detector effects. The migration matrices have been produced up to 8 GeV with an energy step of 100 MeV. The complete set of MM[5] is available in Refs. [118] and [119]. Some migration matrices and the format in which they are produced are shown in Appendix E.
To see how realistic detector capabilities affect the muon neutrino and anti-neutrino energy distribution in Figs. 4.4 and 4.5 we show the PDFs for the calorimetric reconstruction comparing the realistic and perfect reconstruction for the QE and DIS interactions, respectively.

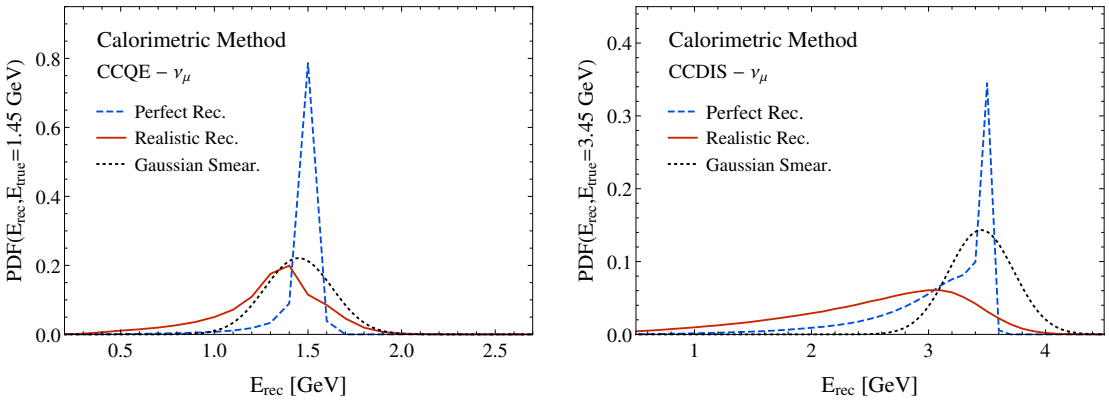

Figure 4.4: Probability distribution function for a ν_μ event as a function of the reconstructed energy. The PDFs are obtained applying the calorimetric reconstruction, and the results, at a fixed true neutrino energy, are obtained for the QE at $E_\nu^{true} = 1.45$ GeV (left panel) and for the DIS at $E_\nu^{true} = 3.45$ GeV (right panel). The blue dashed line and the red solid line are obtained from the perfect and realistic reconstruction, respectively. The black dotted line represents a standard gaussian smearing.

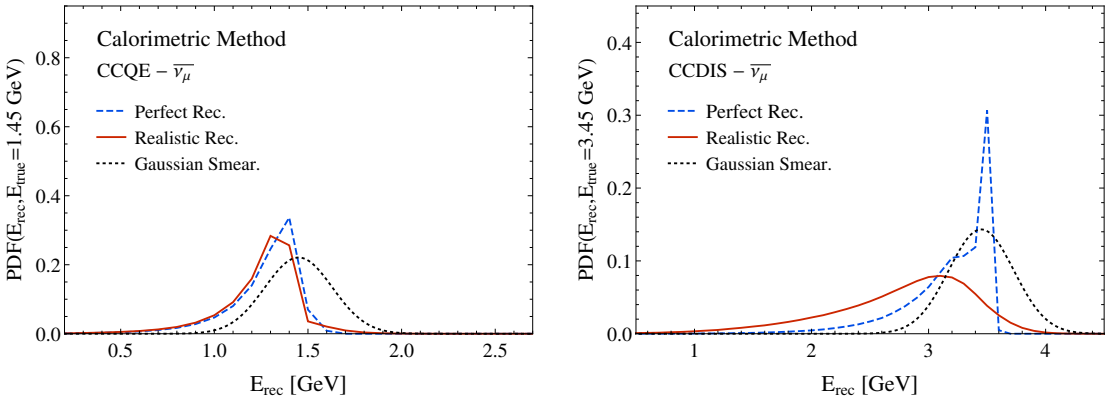

Figure 4.5: Same as Fig. 4.4, but for a $\overline{\nu}_\mu$ event.

[5]The analysis performed to study the impact of $2p2h$ uncertainties, in Sec. 5.3, employes matrices up to 2 GeV with a step of 50 MeV.

The solid lines and the blue dashed lines are the distributions obtained in the case of realistic and perfect reconstruction, respectively. These distributions are given as a function of the reconstructed energy and for a fixed value of the true neutrino energy, that is $E_\nu^{true} = 1.45$ GeV for the QE interaction and $E_\nu^{true} = 3.45$ GeV for the DIS.
As a further comparison it is also shown a gaussian distribution (black dotted line) with the standard deviation $\sigma(E_\nu) = 0.15\sqrt{E_\nu}$, usually used to account for detector effects in phenomenological studies devoted to liquid-argon detectors [113, 120, 121, 122, 123].
The effects of energy resolutions, efficiencies, and thresholds affect the probability for a neutrino event to be reconstructed in the correct energy bin. In particular, finite energy resolution produces a smearing of the measured energy, while imperfect efficiencies and finite thresholds produce a shift to lower energies, due to energy partially carried away by undetected particles. As it can be noticed in Figs. 4.4 and 4.5, PDFs have finite widths, they are asymmetric, with a broader tail toward the lower energies, and their mean values are lowered with respect to the true neutrino energies.
Comparing Fig. 4.4 and Fig. 4.5, we can notice some discrepancies in the behavior of the PDFs for a neutrino and anti-neutrino event. These differences can be traced back to the different contributions of neutrons to the final-state energy (see, for instance, Fig. 4.3) and to the fact that the typical energy transfer is lower in an anti-neutrino interaction.
Furthermore, a certain asymmetry can be seen also in the case of a perfect reconstruction. This feature is a consequence of pion absorption in the nuclear medium and of energy carried away by neutrons, assumed to escape detection. When the realistic detector effects are accounted for, the PDFs clearly broaden due to the employed energy resolutions, and their modes shift toward lower energies. The latter effect is particularly large for DIS events, in which the muon contribution to the final-state energy is typically smaller than in QE scattering, and the role of the efficiencies is larger.
The effective energy resolutions obtained from our distributions are presented as a function of the true neutrino energy in Figs. 4.6 and 4.7, for neutrino and anti-neutrino, respectively. To make contact with existing phenomenological studies of neutrino and antineutrino oscillations, we also add for comparison a few simple functions typically employed as an effective energy resolution. The estimates for QE and DIS events are shown separately, as the lower (darker) and upper (lighter) bands.
The results shown are obtained for the calorimetric reconstruction in the left panels and for the kinematic one in the right panels. Our calculations of the PDF's standard deviations are presented as bands spanning the values between the results for the perfect reconstruction scenario (lower edge) and those for the realistic scenario (upper edge).
Because the energy resolutions widths in the realistic scenario are about twice as large as those in existing experiments, they can be considered optimistic. On the other hand, an effective energy resolution better than our result for the perfect reconstruction scenario can be achieved only by means of neutron detection.
Finally, in Figs. 4.8 and 4.9, we show how the modes of the reconstructed-energy distributions depend on the true value of energy, comparing the calorimetric and kinematic reconstruction methods, for neutrino and anti-neutrino respectively.
The bands represent our Monte Carlo results for QE and DIS events, the lower (upper) edge of which corresponds to the realistic (perfect) scenario.

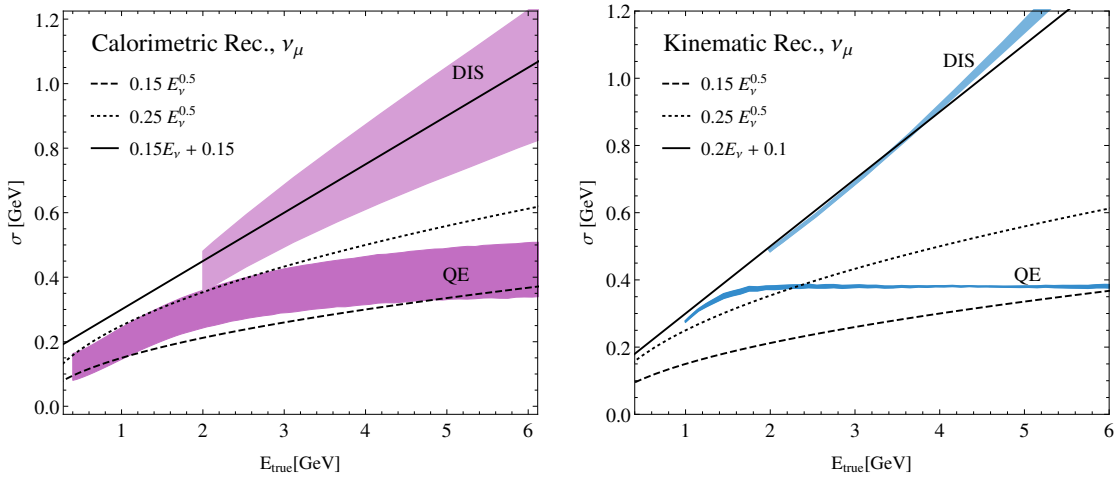

Figure 4.6: Effective energy resolution as a function of the true energy for muon neutrinos, using the calorimetric (left panel) and the kinematic (right panel) reconstruction. The results of our Monte Carlo simulations for QE (DIS) events are shown as lower (upper) bands. For each band, the upper (lower) edge corresponds to the realistic (perfect) detection capabilities, defined in Sec. 4.3. For comparison, a few smearing functions frequently used in phenomenological oscillation studies are also shown.

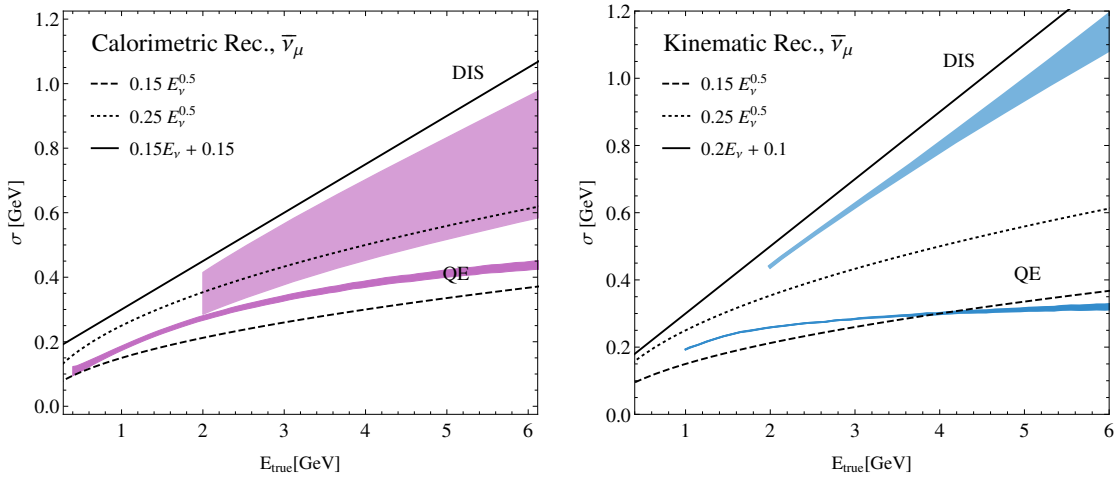

Figure 4.7: Same as Fig. 4.4, but for $\overline{\nu}_\mu$.

In the calorimetric method, the modes for QE scattering are in a good agreement with the true energy, and the expected presence of neutrons in the final state of antineutrino events introduces only a small effect. While for DIS, the agreement is somewhat reduced, especially when detector effects are taken into account, the modes do not differ from the true energy by more than 20%.

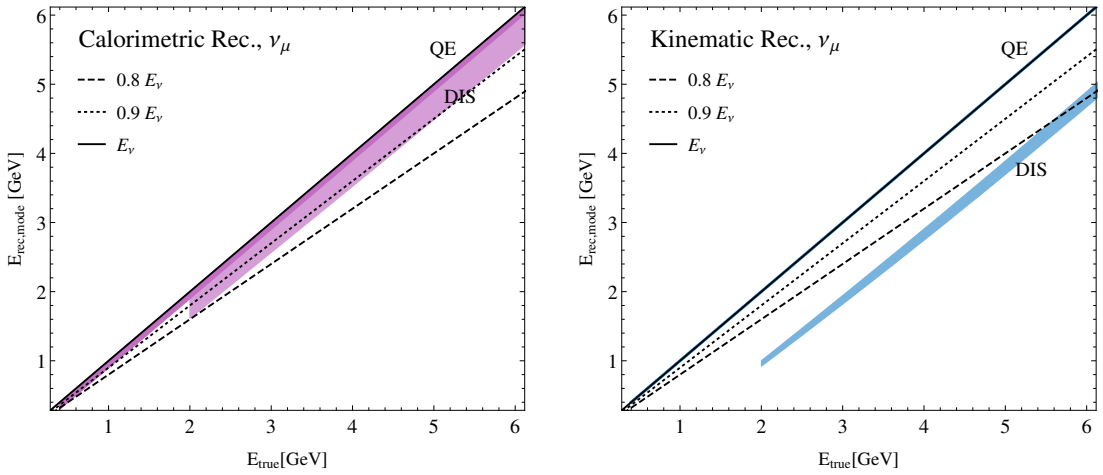

Figure 4.8: Mode of the reconstructed-energy distributions as a function of the true energy calculated for muon neutrinos. The bands show our Monte Carlo results, with the lower (upper) edge obtained assuming the realistic (perfect) scenario. The darker (lighter) bands present the results for QE (DIS) events. As a further comparison, the lines corresponding to the true value and its underestimation by 10 and 20% are also shown.

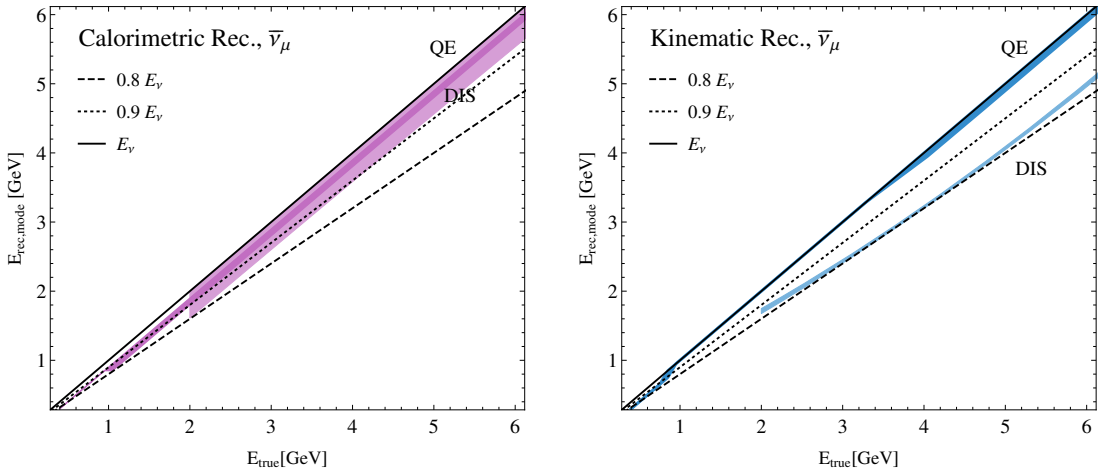

Figure 4.9: Same as Fig. 4.8, but for $\overline{\nu}_\mu$.

For the kinematic method, in QE interactions, both the neutrino and antineutrino modes are in excellent agreement with the true energy. However, this is not the case for DIS events. For antineutrinos, the discrepancy between the DIS mode and the true energy exceeds 10% and is typically close to 20%. For neutrinos, the mode underestimates the true energy by $\sim$ 1 GeV. This behavior can be traced back to the simplicity of our kinematic analysis, assuming that all events containing at least one pion are produced through excitation of a resonance of invariant mass $M_\Delta = 1.232$ GeV.

In conclusion, the bands in Figs. 4.4 - 4.7 show the differences between the results for the realistic and perfect scenarios. Their widths can be used as a measure of the sensitivity to

detector effects, which turns out to be larger for the calorimetric migration matrices than for the kinematic ones. However, they do not represent uncertainties entering any actual experiment. In practical situations, detection capabilities and their uncertainties must be estimated in test-beam exposures.

Chapter 5

Oscillation analysis

In this Chapter we describe three different oscillation analyses aimed at the estimation of the impact of the systematic uncertainties on the extraction of the oscillation parameters in long-baseline experiments.
In the first analysis, performed in the disappearance channel, we study the effect of the incorrect estimation of the detector performances on the extraction of the atmospheric parameters, using the two different reconstruction techniques introduced in this Thesis [118].
In the second analysis we estimate, in the appearance channel, the effects of the missing energy on the determination of the CP-violating phase using the calorimetric reconstruction [124].
Finally, we consider the impact on the atmospheric parameters of two different approaches that can be used to describe multi-nucleon mechanism [125]. The kinematic method of energy reconstruction has been used to analyze events produced with GENIE according to two different models for the description of interactions in the quasi-elastic range: in the first case two-particle two-hole processes are taken into account using the GENIE model, and in the second case multi-nucleon effects are included using an increased value of the axial mass for the parametrization of QE interactions.
The study of the oscillation parameters, introduced in Chapter 1, is based on the analysis of the event rates. A general expression of the event rates in the oscillation channel $\nu_\alpha \to \nu_\beta$ and in the energy bin $[E_i^\nu, E_i^\nu + \Delta E^\nu]$, is given by

$$N_\beta^i = \int_{E_i^\nu}^{E_i^\nu + \Delta E^\nu} \mathrm{d}E^\nu \; \sigma_{\nu_\beta}(E^\nu) P_{\nu_\alpha \to \nu_\beta}(E^\nu, \theta_i, \delta) \frac{\mathrm{d}\phi_{\nu_\alpha}(E^\nu)}{\mathrm{d}E^\nu} \epsilon_\beta(E^\nu) \; , \tag{5.1}$$

where σ_{ν_β} is the neutrino cross section, $P_{\nu_\alpha \to \nu_\beta}$ is the oscillation probability for the considered channel dependent on the mixing angles θ_i, and on the CP violating phase δ, ϕ_{ν_α} is the neutrino flux and ϵ_β is the signal efficiency, eventually dependent on the neutrino energy.
From the knowledge of the event rate it is possible to extract the oscillation parameters that enter in the probability $P_{\nu_\alpha \to \nu_\beta}$. But, as can be seen from (5.1), there is a strong dependency on the neutrino energy E^ν. Neutrino beams are produced as tertiary decay products, coming from the decay of pions and kaons mostly, and their energy is not sharply defined, but widely distributed. So the energy of the incoming neutrino has to be reconstructed from the information that we can obtain from the final state produced by the

neutrino-nucleus interaction.
The reconstruction of neutrino events leads to systematic uncertainties that depend on the detector capabilities (that is on the detection efficiency of the particles in the final state) and on the interaction channel.
Above the quasi-elastic (QE) peak, other interaction processes in charged current take place: resonance production, deep inelastic scattering (DIS) and two-particle two-hole ($2p2h$) processes.
The analysis of neutrino events has been done using the calorimetric and kinematic energy reconstruction described in (4.8) and (4.11). These two reconstruction techniques have been applied considering the experimental features for particles detection, as listed in Sec. 4.3.
We produced the Migration Matrices (MM), $M_{ij} \equiv N(E_i^{rec}, E_j^{true})$, that define the probability that an event with a true neutrino energy in the bin j ends up being reconstructed in the energy bin i, as explained in Section 4.4. The MM have been produced for all interaction channels considered and for the four neutrino types $(\nu_e, \bar{\nu}_e, \nu_\mu, \bar{\nu}_\mu)$.
The oscillation analysis has been performed using the software GLoBES [126, 127, 128].

5.1 Impact of detector effects in disappearance experiments

In the disappearance oscillation channel $\nu_\mu \to \nu_\mu$, we perform an analysis for the determination of atmospheric parameters θ_{23} and Δm^2_{31}. The main contribution to the background is given by neutral current (NC) events, misidentified as CC events. It is expected to be low, compared to the signal, so we neglect it in our analysis.
Matter effects are included in the analysis, where the matter density profile has been chosen according to the "Preliminary Reference Earth Model" (PREM) [129]. Systematic uncertainties are used in order to accommodate possible differences in the shape of the expected event distribution at the detectors, as in [130] and [105]. Their treatment and the χ^2 implementation[1] follow Refs. [128, 130] where systematic errors have been largely investigated, and we assumed a 20% bin-to-bin uncorrelated systematic uncertainty, as well as a 20% overall normalization uncertainty, which is bin-to-bin correlated. This scheme is simpler than the one used in actual experiments, therefore, the constraints we will obtain just represent a lower limit. The true input values used for the analysis are listed in Table 5.1, from Ref. [35], and they have been kept fixed during the analysis.

Δm^2_{21}	Δm^2_{31}	θ_{12}	θ_{23}	θ_{13}	δ
$7.50 \times 10^{-5}\text{eV}^2$	$2.457 \times 10^{-3}\text{eV}^2$	33.48 deg	42.3 deg	8.5 deg	0.0

Table 5.1: Values of the oscillation parameters used for the analysis as *true* input values.

The experimental setups used in our analysis belong to two different classes: a *low-energy setup* (LE), with a narrow band off-axis neutrino beam and a *high-energy setup* (HE), with

[1] The χ^2 analysis is also briefly discussed in Appendix F.

a broad-band on-axis beam. These choices are motivated by the fact that we could be able to study effects of neutrino energy reconstruction for a wider set of neutrino-nucleus interactions, that goes beyond the quasi-elastic interaction.
In the LE configuration, the neutrino flux is peaked at $\sim$ 600 MeV, with a baseline of 295 km, while the HE setup has a flux peaked at $\sim 1-2$ GeV and a baseline of 1000 km. These main features are summarized in Tab. 5.2, and the fluxes are shown in Fig. 5.1

Experimental Setup	Type	Baseline	Energy Peak
Low Energy (**LE**)	off-axis	295 km	600 MeV
High Energy (**HE**)	on-axis	1000 km	$1-2$ GeV

Table 5.2: Relevant features of the two experimental setups chosen for the disappearance analysis, aimed at quantify the impact of the incorrect estimation of detector effects.

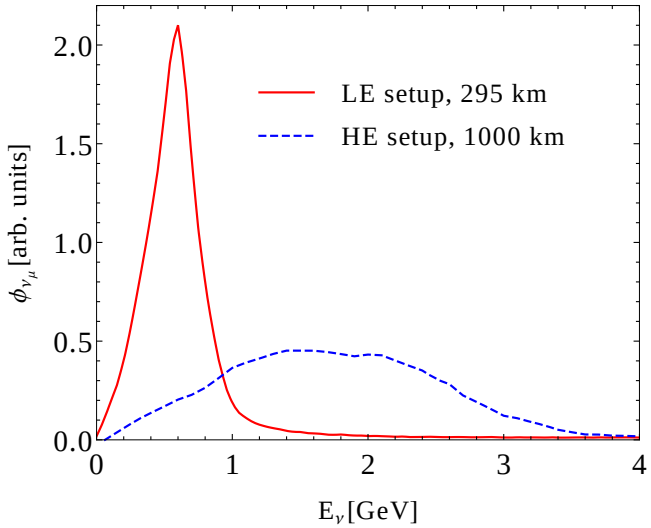

Figure 5.1: Muon neutrino fluxes in arbitrary units as a function of the neutrino energy. The red line represents the low-energy setup flux, while the blue dashed line the high-energy setup flux.

Both configurations have advantages and disadvantages. In an off-axis configuration, due to pion-decay kinematics, the neutrino flux is more peaked around a given neutrino energy. It also allows a significant reduction of the background coming from neutral current events, and guarantees that the range of the values of L/E_ν is well localized around the first oscillation maximum. However the beam intensity is highly reduced compared to an on-axis configuration, thus the number of events at the far detector is also lower.
In an on-axis configuration the energy spread of the beam is larger. This allows to determine the shape of the oscillation probability performing measurements at different values of L/E_ν. Due to the high intensity of the neutrino beam it is also easier to collect a larger statistics. However, the high energy tail produces a significant neutral-current background

contamination.
The ν_μ-disappearance analysis within these two different experimental setups has been done considering a normalization on the number of the un-oscillated events, in the energy range relevant for the two analysis, around ~ 5000 events, as reported in Tab. 5.3. Due to the differences in the fluxes shape, the energy window considered would not be the same for the two setups. We choose for the LE configuration the energy window $[0.3, 2]$ GeV, while for the HE $[0.3, 4]$ GeV.

	QE	**2p-2h**	**res**	**DIS**	Total
LE [0.3,2] GeV	49%	28%	21%	2%	4891
HE [0.3,4] GeV	26%	11%	37%	26%	4456

Table 5.3: Number of un-oscillated events for the two experimental setups under study, with the percentage of the number of events coming from the different interaction channels.

As we can see from the Table, the event samples in the two experimental setups are very different. In the HE setup we obtain a larger contribution from inelastic processes, compared to the LE setup that privileges the QE-like sample.
In general the neutrino oscillation analysis is based on Monte Carlo simulations in order to generate the event rate distribution. To be more predictive, these simulations needs to include also detector capabilities. According to this, we generated our *true* event distribution using realistic MM, with the aim of reproducing an event distribution obtainable in a "realistic" experiment

$$N_i^{true} = \sum_X \sum_j M_{ij}^{X,real} N_j^X \ , \tag{5.2}$$

where X represents the interaction channel (QE, $2p2h$, resonance production and DIS) and i and j are the energy-bin indices. $M^{X,real}$ represents the matrices obtained from the realistic scenario, and N_j^X is the number of events in the energy bin j for the interaction type X, computed without accounting for the detector effects.
To perform our analysis we generated the predicted (or *fitted*) event distribution including the uncertainties related to the estimation of the detector performances. In practice, the fitted event rate has been generated using a linear combination of the matrices obtained for the realistic and perfect reconstruction scenarios (see Section 4.3), due to the fact that the production of MM is computationally expensive. This approach, allowing for a continuous transformation of the event-rate distribution from one scenario to the other, is useful to quantify when the incorrect estimation of the detector performance starts to have a significant impact on the fit. Thus, the event distributions used for the fit are given by

$$N_i^{fit} = \sum_X \sum_j \{(1-\alpha) M_{ij}^{X,real} + \alpha M_{ij}^{X,perf}\} N_j^X \tag{5.3}$$

where $M^{X,perf}$ and $M^{X,real}$ represent the matrices obtained from the perfect and realistic scenario, respectively. The parameter α in Eq. (5.3) is a phenomenological parameter used in order to obtain an *effective* migration matrix as a linear deformation of the two

extreme cases [105], that is the perfect and realistic scenarios. For example, if the value of α is set equal to zero, this means that the fitted rates are obtained in the same way as the true rates. Likewise, if we set $\alpha = 0.3$, we will have the fitted rate obtained with an overestimation of the detector performances of the 30%.
When the fitted rate is computed, it is simulated for every value of the oscillation parameters in the plane $(\theta_{23}, \Delta m^2_{31})$. After the identification of the point with the minimum value of the χ^2, the confidence region is drawn with the requirement

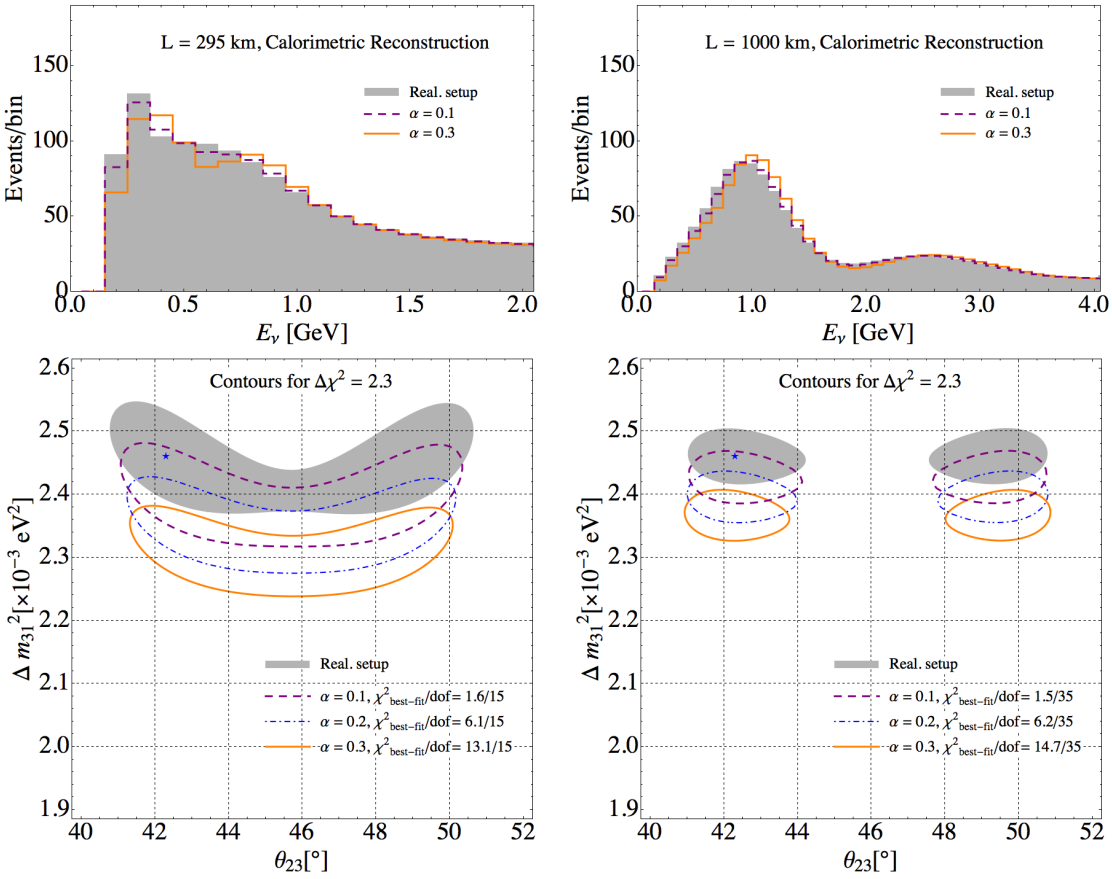

Figure 5.2: Results for the analysis of the oscillation parameters when the calorimetric method is applied to analyze neutrino events. On the left there are the results for the LE setup, while on the right the ones obtained for the HE setup. Upper panels: event rate distribution at the far detector as a function of the reconstructed neutrino energy, using the oscillation parameters in Tab. 5.1. The shaded histogram is obtained when realistic MM are applied, while the dashed and solid lines are obtained when we consider a combination of realistic and perfect matrices using $\alpha = 0.1$ and $\alpha = 0.3$, respectively. Lower panels: confidence regions in the plane $(\theta_{23}, \Delta m^2_{31})$ at 1σ C.L. for 2 d.o.f. The shaded area corresponds to the perfect estimate of the detector effects. The lines show the contours obtained for the detector performance overestimated by 10%, 20%, and 30% in the fit. The blue star is the true input value.

$$\Delta\chi^2(\theta_{23}, \Delta m^2_{31}) \equiv \chi^2(\theta_{23}, \Delta m^2_{31}) - \chi^2_{best\,fit} < 2.30 \tag{5.4}$$

that is at 1σ for two degrees of freedom (d.o.f). The results of our analysis are shown in Figs. 5.2 - 5.3, for the calorimetric and kinematic reconstructions, respectively.

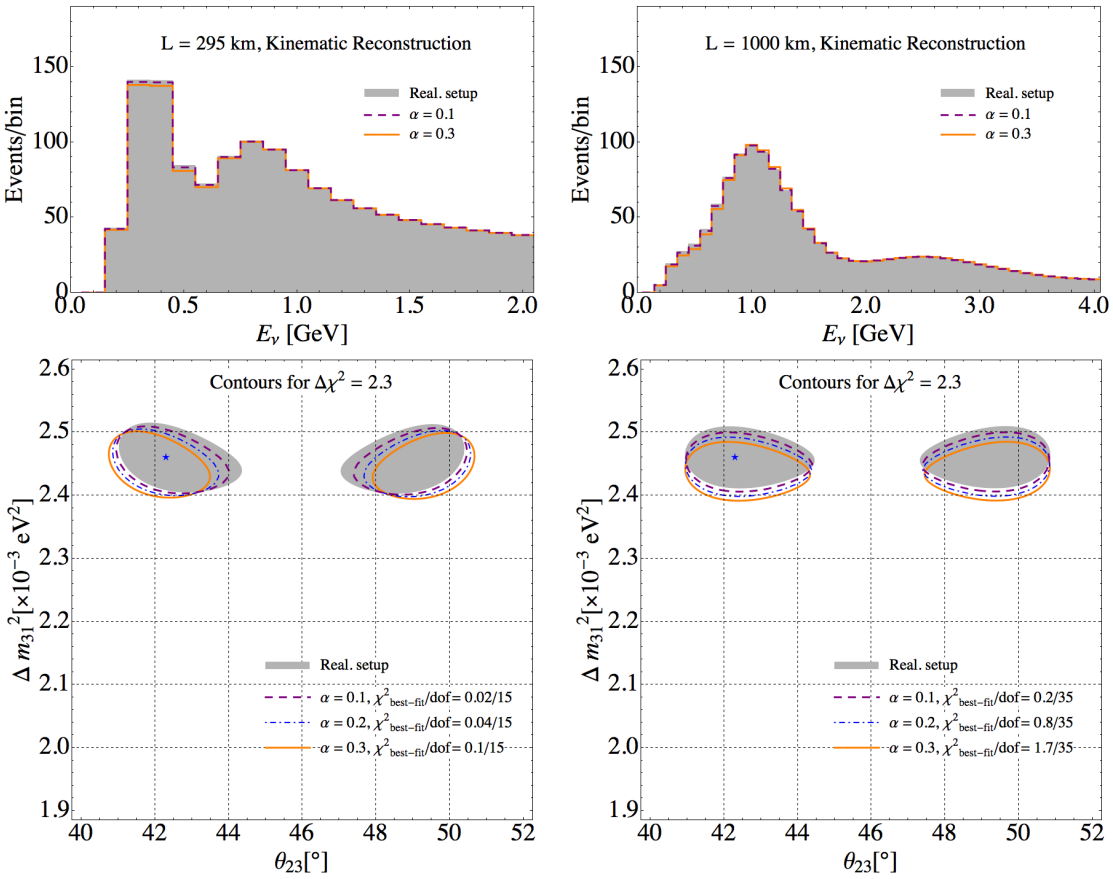

Figure 5.3: Same as Fig. 5.2, but applying the kinematic method of energy reconstruction.

On the left we have the results for the LE setup and on the right those obtained for the HE setup. In the upper panels there are the event rate distributions, where the shaded areas are obtained using realistic MM, while the dashed and solid lines are obtained using a combination of realistic and perfect matrices, for the values of α equal to 0.1 and 0.3. Notice that the event rates shown using the linear combination of realistic and perfect matrices, have been computed with the true input values of the oscillation parameters. The lower panels show the confidence regions in the plane $(\theta_{23}, \Delta m^2_{31})$ at 1σ C.L. for 2 d.o.f. The shaded areas are obtained when the true and the fitted rates are computed using the same set of MM, and correspond to a complete estimation of the detector capabilities. The lines are instead obtained when the true rate is computed from realistic MM and for the fit a combination of realistic and perfect matrices is used for $\alpha = 0.1$ (dashed lines), $\alpha = 0.2$ (dot-dashed lines) and $\alpha = 0.3$ (solid lines). These confidence regions represent the regions allowed when the detector performances are overestimated of the 10%, 20% and 30%. In the case of the calorimetric reconstruction, the allowed confidence regions start to drift away from the shaded areas when the detector capabilities are incorrectly estimated, excluding the true input value for an overestimation more than 10%. In the case of the

kinematic reconstruction, the result obtained is milder compared to the calorimetric one. This is mostly due to the fact that it relies on the ability of reconstructing the track of the outgoing lepton, and actually the muon reconstruction is very precise in modern detectors. Finally, in the figures it is also shown the minimum value of the χ^2 obtained for each value of α, together with the effective number of d.o.f.[2].

5.2 Impact of missing energy on the extraction of the CP-violating phase

The aim of the analysis presented in this section is to describe the problem arising from missing energy and to explore the level of accuracy required in estimating it to avoid a deleterious effect on the measurement of the CP phase. We perform a phenomenological study aimed at demonstrate and quantify how an underestimation of the missing energy in neutrino events may affect the extraction of the value of CP-violating phase δ.
To analyze the effect of realistic detection capabilities on the energy reconstruction in a fine-grained TPC (Time Projection Chamber), we take into account energy resolutions, efficiencies, and thresholds for particle detection, as in the previous case (details in Sec. 4.3).
It should be stressed the fact that our results are inevitably subject to uncertainties coming from nuclear effects. In order to minimize nuclear uncertainties, we consider the carbon target, for which a number of extracted cross sections is available.
The considered experimental setup consists on a wide-band neutrino beam produced mainly from pion and kaon decays, aimed at a 40 kton detector located at a distance of $L = 1300$ km from the source. The neutrino flux used for this analysis consists in a 80 GeV beam configuration from Ref. [131], with an assumed beam power of 1.08 MW. The background implementation follows Ref. [131] as well, where the sensitivities for the neutral- and charged current mis-identification rates are set at the 1%. No migration matrices are used for the background events, which are always smeared according to a Gaussian with $\sigma(E_\nu) = 0.15\sqrt{E_\nu}$, with E_ν in GeV. Since the detection of neutrino and antineutrino CC events depends on the ability to observe and tag only the associated charged lepton, we use the same signal efficiencies as in Ref. [131] (80%). The energy of all particles produced in the event (both the charged leptons and the hadrons) are then smeared according to a Gaussian before reconstructing the neutrino energy. Detection thresholds and efficiencies for all hadrons are implemented as well (see Chapter 4). The hadron thresholds and efficiencies will affect the smearing of the events in reconstructed neutrino energy, but not the total event rates.
To perform this study we considered a combined measure of $\nu_\mu \to \nu_e$ and $\overline{\nu}_\mu \to \overline{\nu}_e$ with a total of 6 years (3 in positive horn focusing/neutrino running mode, and 3 in negative horn focusing/antineutrino running mode). Under these assumptions, the total number of events in the neutrino and antineutrino running modes with reconstructed energies between 0.6 GeV and 6 GeV are reported in Tab. 5.4, including also the background contribution coming from intrinsic contamination of the beam of ν_e and $\overline{\nu}_e$, misidentified ν_μ and $\overline{\nu}_\mu$, and neutral currents.

[2]The effective number of degrees of freedom is given by the number of energy bins used in the fit minus the number of parameters determined from the fit.

	Signal	Intrinsic ν_e-$\overline{\nu}_e$	Mis ν_μ-$\overline{\nu}_\mu$	NC
$\nu_\mu \to \nu_e$	740	114	67	65
$\overline{\nu}_\mu \to \overline{\nu}_e$	286	67	33	38

Table 5.4: Expected event rate for the two oscillation channels at the far detector, including the different background sources that we considered. The obtained values are in agreement with those of Ref. [131].

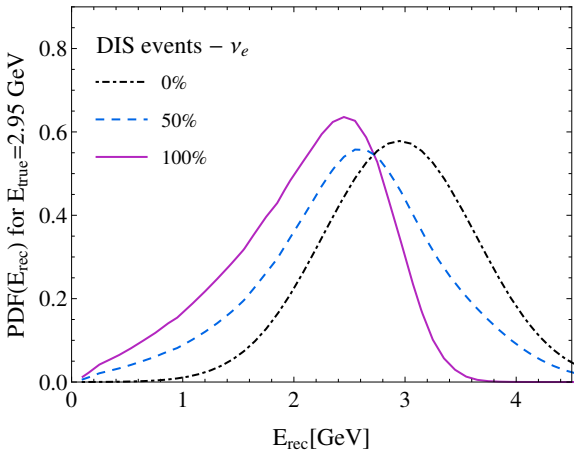

Figure 5.4: Reconstructed energy distributions obtained for ν_e deep-inelastic scattering (DIS) events with true energy of 2.95 GeV. The distributions neglecting the shift due to the missing energy (dot-dashed line), and accounting for its 50% (dashed line) are compared to the full calculations (solid line).

It should be noted that in the antineutrino running mode we consider both $\bar{\nu}_\mu \to \bar{\nu}_e$ and $\nu_\mu \to \nu_e$ as the signal events due to the large contribution to the signal from wrong-sign events, which are also sensitive to CP violation. In the neutrino running mode, however, only the $\nu_\mu \to \nu_e$ events are considered as part of the signal, since the wrong-sign contribution is negligible.

For this analysis we did not consider the near detector. However we made more aggressive assumptions for the systematic uncertainties, and assume that thanks to a possible near detector we will be able to achieve these goals. We considered the same systematic uncertainties of the previous analysis but a prior at the 2% level is considered for both normalization and shape uncertainty, following Refs. [120, 131]. As for the background, only a global normalization uncertainty, at the 5% level, is considered.

Since the atmospheric parameters are fixed to their current best-fit values, and we are only interested in the δ sensitivity, there is no need to include ν_μ and $\bar{\nu}_\mu$ disappearance channels in our analysis. It should be kept in mind, though, that the measurement of the disappearance parameters may be significantly affected by either an incorrect estimate of nuclear effects and/or by an inaccurate detector calibration, as it was pointed out in Refs. [105, 118, 130], among others. This in turn unavoidably affect the extraction of the value of the CP-violating phase from appearance measurements.

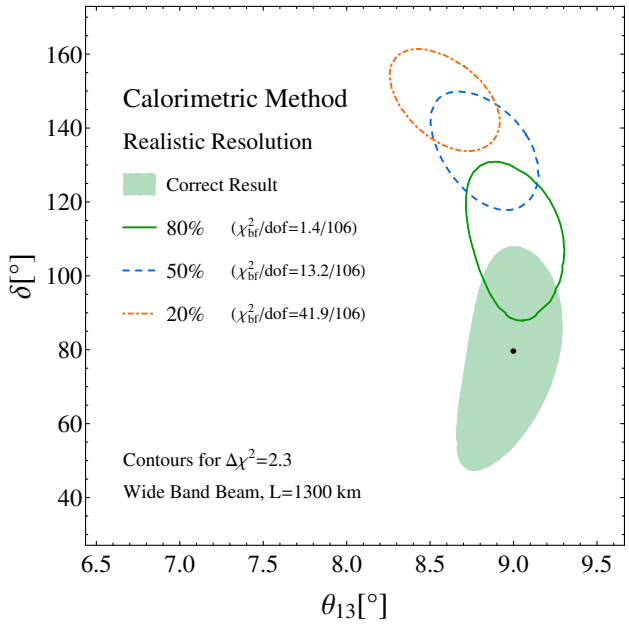

Figure 5.5: Effect of an underestimation of the missing energy in the calorimetric energy reconstruction on the confidence regions in the (θ_{13}, δ) plane, see text for details. The true values of the oscillation parameters are indicated by the dot, and are the same for all contours shown.

The true event rates are obtained taking into account realistic detection capabilities which are implemented using the migration matrices obtained from Monte Carlo events analysis, as in the previous Section. Therefore, the neutrino energy is not reconstructed around the true energy but around a lower value instead, owing to the energy carried away by unobserved particles in the final state.
The fitted event rates are smeared using a different function. In the ideal case where no particle escapes detection, the neutrino energy would be smeared according to a Gaussian distribution centered around the true neutrino energy, with a width dependent on the energy smearing of the different particles observed. As in the previous study, the event rates used to fit the data are smeared using a linear combination of MM, but this time using the two cases described above: migration matrices from the realistic scenario, and the Gaussian smearing around the true neutrino energy. By varying the coefficients in this linear combination, the effective smearing function obtained can be deformed smoothly from one situation to the other. Using this approach, we introduce a way to manually tune the amount of missing energy in the oscillation analysis, while at the same time we account for the effect of realistic energy resolutions of the detector. In summary we have

$$N_i^{true} = \sum_X \sum_j M_{ij}^{X,real} \; N_j^X \tag{5.5}$$

$$N_i^{fit} = \sum_X \sum_j \left\{ (1-\alpha) M_{ij}^{X,real} + \alpha M_{ij}^{X,gauss} \right\} N_j^X \; , \tag{5.6}$$

where $M_{ij}^{X,real}$ and $M_{ij}^{X,gauss}$ are the realistic matrices and the gaussian distributions,

respectively. To illustrate how the energy reconstruction is affected by the missing energy, in Fig. 5.4 we show an example for deep-inelastic ν_e scattering at the true energy $E_\nu = 2.95$ GeV. The solid line represents the reconstructed energy distribution calculated from the Monte Carlo simulations with all detector effects. Should no energy be missing, the distribution would be centered at the true value of the neutrino energy, as the dot-dashed curve. A common way used in the literature to parametrize the resolution in neutrino energy in oscillation experiments is by using a Gaussian function with a simple function for its standard deviation

$$\sigma(E_\nu) = \alpha + \beta\sqrt{E_\nu} + \gamma E_\nu \ , \tag{5.7}$$

where E_ν is the true neutrino energy in GeV. Typical values used in phenomenological studies of liquid argon detector experiments are $\sigma(E_\nu) = 0.15\sqrt{E_\nu}$, see e.g. Refs. [120, 121, 132, 133]. In our case, we use the migration matrices which have been obtained from the neutrino events analysis, and fit the result to a Gaussian with a width as in Eq. (5.7). In the case of ν_e DIS events in the Fig. 5.4, the gaussian smearing is represented by the dot-dashed line. For further details on the gaussian distributions used see Appendix G. Finally, the dashed curve, obtained from linear interpolation between the dot-dashed and solid lines, represents an intermediate situation in which 50% of the missing energy is accounted for: the two distributions used in the linear interpolation do have the same width, while their central value differs due to the impact of missing energy in the events. It should also be noted that, for each type of neutrino interaction considered in this work, the width of the distribution obtained when computing the migration matrices is generally different. The allowed confidence regions in the (θ_{13}, δ) plane are shown in Fig. 5.5. The different contours have been obtained under different assumptions regarding the ability of the experiment to determine the missing energy involved in the events. The shaded area corresponds to the correct result, where all the missing energy in the events is perfectly estimated in the fit. The solid, dashed, and dot-dashed lines represent the results obtained when 90%, 80%, and 70% of the missing energy is correctly accounted for, respectively. Our results show that even a 20% underestimation of the missing energy introduces a sizable bias in the extracted δ value. Should an experimental analysis suffer from a 30% underestimation of the missing energy, it would incorrectly exclude the true value of δ at a confidence level between 2 and 3σ.
The legend in Fig. 5.5 also shows the values of the χ^2 for the best fit (θ_{13}, δ) points divided by the effective number of degrees of freedom. In an actual experiment, this ratio would give an additional contribution to the goodness of fit. A large enough contribution would indicate that the model used to fit the data is not correct. Our results indicate that such contribution would be small enough that, from a fit to the far detector data alone, it would be virtually impossible to realize that the energy carried away by undetected particles is being underestimated in the fit.

5.3 Impact of $2p2h$ uncertainties

The T2K Collaboration has recently reported two measurements of the inclusive cross section for charged-current muon-neutrino scattering off the hydrocarbon target, CH [43, 111]. Being flux-averaged at different mean-energy values, the T2K results show the cross section as a function of neutrino energy with minimal dependence on nuclear models.

While the T2K data are lower by ∼20% than the flux-averaged hydrocarbon result previously obtained by the SciBooNE Collaboration [50], with the difference exceeding the experimental uncertainties, they appear to be in good agreement with the expectations based on the ${}^{12}_{6}C(\nu_\mu, \mu^-)X$ cross section measured at higher energies by the NOMAD experiment [49].

At the kinematics of the T2K and SciBooNE experiments, momentum transfers $\mathbf{q}$ are typically large enough for neutrinos, probing the nuclear interior with the spatial resolution $\sim 1/|\mathbf{q}|$, to scatter off individual (bound) nucleons. On the other hand, the dominant contribution to the cross section comes from low energy transfers ω, insufficient to produce pions, and the quasi-elastic mechanisms of interaction,

$$\begin{aligned} \nu_\ell + n &\to \ell^- + p, \\ \bar{\nu}_\ell + p &\to \ell^+ + n, \end{aligned} \tag{5.8}$$

play the most important role.

In the past, CCQE processes were considered well understood theoretically and used to determine the flux normalization [134]. Recently, however, it has become apparent that this is not the case to the extent required by precise oscillation experiments [135]. For example, while the CC QE cross sections of carbon reported by the MiniBooNE Collaboration [40, 41] turn out to be higher than those of free nucleons, the corresponding NOMAD data [103] show the cross-sections' reduction arising from nuclear effects. Although those puzzling discrepancies have received a great deal of theoretical interest, their interpretation is not fully established so far.

In particular, while a non-negligible role of CCQE reaction mechanisms involving more than one nucleon is now generally acknowledged, and important theoretical progress has been achieved [136], an *ab initio* estimate of the corresponding cross sections is not yet available. As those multinucleon mechanisms involve predominantly two nucleons, we refer to them as $2p2h$ processes.

For nuclear targets ranging from carbon to iron, a growing body of experimental evidence [39, 40, 51, 137, 138, 139] shows that $2p2h$ effects on the differential QE cross sections can be effectively accounted for by increasing the value of the axial mass M_A, typically to ∼1.2 GeV, with respect to $M_A = 1.03$ GeV extracted predominantly from deuterium measurements [140]. Note that as the axial mass is the cutoff parameter driving the axial form factor's dependence on $Q^2 = |\mathbf{q}|^2 - \omega^2$, its changes affect both the differential and total cross sections.

In this section, we study uncertainties of the $2p2h$ cross sections for carbon and quantify their effect on the oscillation analysis for an experimental setup similar to the Low Energy Setup discussed in Sec. 5.1. We consider a disappearance experiment running in both neutrino and antineutrino mode with the same flux [141], peaked at ∼600 MeV. To describe the ground-state properties of the target nucleus, we use the realistic Spectral Function of Ref. [95]. To account for an increase of the CCQE cross sections due to $2p2h$ processes, we used two data-driven phenomenological methods: (i) an increased value of the axial mass, yielding results consistent with the T2K [43, 111], NOMAD [49, 103], and MINERvA [44, 142] data, and (ii) the $2p2h$ estimate in the GENIE Monte Carlo generator [109], determined from the MiniBooNE data [40] and in agreement with the experimental cross sections extracted from SciBooNE [50].

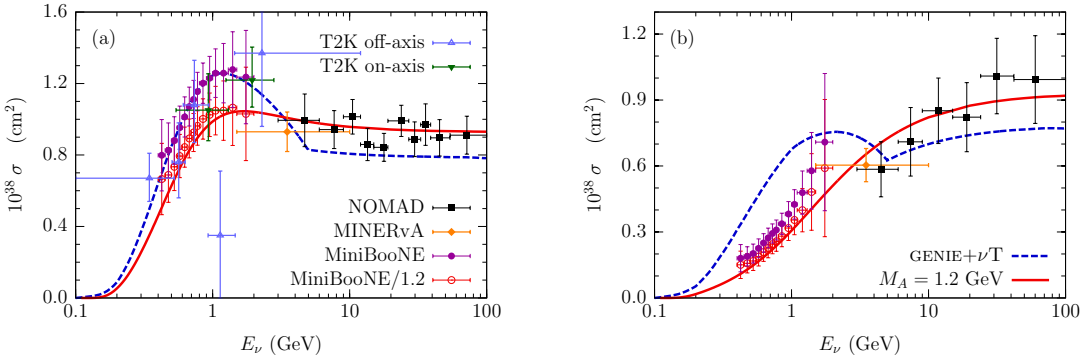

Figure 5.6: CCQE (a) ν_μ and (b) $\bar{\nu}_\mu$ cross sections. The results for carbon obtained using GENIE + νT (dashed lines) and the Spectral Function approach with $M_A = 1.2$ GeV (solid line) are compared with the carbon data reported by the MiniBooNE [40, 41] and NOMAD [103] Collaborations and the hydrocarbon data extracted from the MINERvA [44, 142] and T2K [139, 143] experiments. For comparison, the MiniBooNE data divided by 1.2 are also shown.

We emphasize that although our study is performed for a setup similar—not identical—to that of T2K, it does not follow the analysis of that experiment. For example, applying a generalization of the kinematic method of energy reconstruction [118], we include in the oscillation analysis events of *all types*, instead of the CCQE event sample alone. The rationale for considering the T2K-like kinematics is its importance for the next generation of oscillation experiments [52, 144].

Consequences of 2p2h effects for the CCQE cross sections have been analyzed within a few effective approaches. The calculations of Martini *et al.* [145, 146, 147, 148], based on the local Fermi gas model and the random-phase approximation (RPA), extend the treatment of multinucleon contributions to the electromagnetic responses of iron developed by Alberico *et al.* [149] to the case of neutrino interactions with carbon and to a broader kinematic region.

While employing the local Fermi gas model and the RPA scheme, the approach of Nieves *et al.* [150, 151, 152, 153] differs from that of Martini *et al.* by using effective interactions, the parameters of which were fixed in earlier studies of photon, electron, and pion scattering off nuclei. At the MiniBooNE kinematics, the CCQE ν_μ ($\bar{\nu}_\mu$) cross sections obtained by Nieves *et al.* are lower by ∼10% (∼15%) with respect to those calculated by Martini *et al.*

To extend their superscaling approach and include the contributions of processes involving two-nucleon currents, Amaro *et al.* [154, 155] and Megias *et al.* [156, 157] have estimated the 2p2h cross sections within the relativistic Fermi gas model accounting for the vector meson-exchange currents.

In the Giessen Boltzmann-Uehling-Uhlenbeck transport model, the 2p2h contribution to the CCQE cross sections is obtained from a fit to the MiniBooNE data performed by Lalakulich *et al.* [158].

As pointed out in Sec. 4.2, GENIE [101] simulates 2p2h events following the empirical procedure developed by Dytman [109], based on the one derived for electron scattering in Ref. [110]. The 2p2h strength is set to decrease linearly for neutrino energy larger than 1

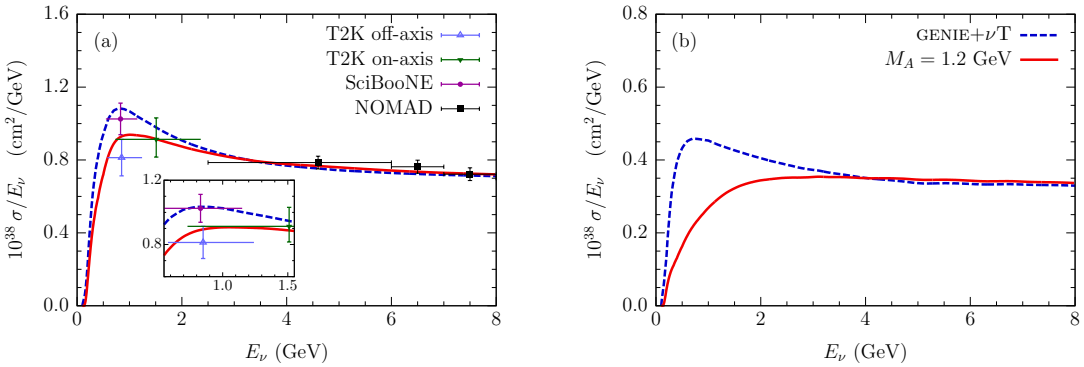

Figure 5.7: Per-nucleon CC inclusive (a) ν_μ and (b) $\bar{\nu}_\mu$ cross sections divided by neutrino energy, obtained using the QE contributions of Fig. 5.6. The calculations for the carbon target (and for the hydrocarbon target in the inset) are compared with the carbon data extracted from the NOMAD [49] experiment and the hydrocarbon flux-averaged measurements reported by the SciBooNE [50] and T2K [43, 111] Collaborations (the central energy values correspond to the mean energy in the detector). Note that antineutrino data are currently unavailable.

GeV and to vanish at 5 GeV, consistently with both the MiniBooNE [40] and NOMAD [103] data.

We analyze how the oscillation analysis may be affected by uncertainties in the description of $2p2h$ contributions to the CCQE cross sections, comparing two estimates obtained from different approaches:

- In the first case, we apply an effective value of the axial mass $M_A = 1.2$ GeV to account for the modifications of the QE cross sections due to $2p2h$ reaction mechanisms in a purely phenomenological manner ("effective" calculations).

- In the second case, we add the $2p2h$ results obtained using GENIE 2.8.0 [109] to the QE calculations performed using the Spectral Function approach with $M_A = 1.03$ GeV, as implemented in the νT package [106] ("GENIE + νT" calculations).

The obtained total CCQE cross sections are compared to the experimental data in Fig. 5.6. It clearly appears that the effective calculations are in good agreement with the NOMAD [103] and MINERvA [44, 142] results for both neutrinos and antineutrinos. They also reproduce the energy dependence of the MiniBooNE data [40, 41], but not their absolute normalization. To better illustrate this feature, we have divided the MiniBooNE cross sections by a factor of 1.2, consistent with the ratio of the detected to predicted events of 1.21 ± 0.24 reported from the first MiniBooNE analysis [39].

For neutrinos the $2p2h$ contribution from GENIE is in very good agreement with the MiniBooNE data, while for antineutrinos it overestimates the experimental points, in spite of being added to the Spectral Function results obtained using $M_A = 1.03$ GeV, which are too low to reproduce the cross sections from NOMAD [159]. Owing to their large uncertainties, the T2K CCQE data [139, 143] cannot discriminate between the two calculations.

Adding the considered CCQE estimates to the cross sections for resonant, non-resonant, and coherent pion production from GENIE, we have calculated the inclusive CC cross sections for carbon shown in Fig. 5.7. The two considered approaches turn out to be in

good agreement with the NOMAD data [49], collected in the region dominated by pion production.
To compare to the T2K [43, 111] and SciBooNE [50] data, extracted for the hydrocarbon target, we have accounted for the contribution of free protons using the cross sections from GENIE + νT. While the on-axis T2K data point [111] does not distinguish the two approaches, the SciBooNE point [50] clearly favors the GENIE + νT calculations and the off-axis T2K point [43] shows a distinct preference for the effective calculations.

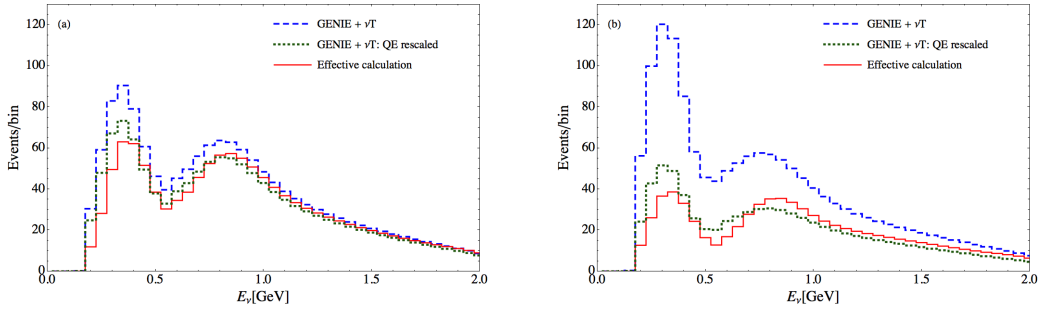

Figure 5.8: Distribution of CC (a) ν_μ and (b) $\bar{\nu}_\mu$ events in the far detector as a function of the reconstructed energy, obtained within the GENIE + νT and effective calculations. For comparison, we also show the GENIE + νT results with the unoscillated QE event rates rescaled to those of the effective calculations.

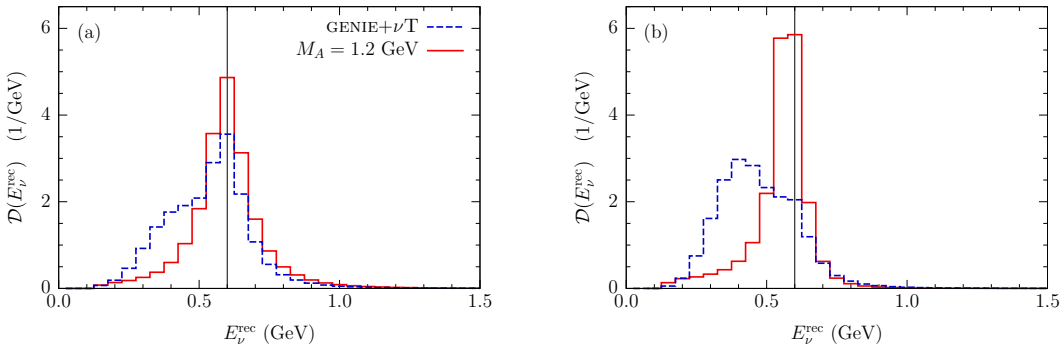

Figure 5.9: Reconstructed energy distributions of CC QE (a) ν_μ and (b) $\bar{\nu}_\mu$ events with any number of nucleons calculated at $E_\nu = 0.6$ GeV. The dashed (solid) lines represent the results obtained using the GENIE + νT (effective) approach.

The puzzling difference between the T2K and SciBooNE data—interesting in its own right—has important consequences for neutrino-oscillation studies.
Neutrino events have been reconstructed using the kinematic method, applying it to all event types. As neutral-current background is expected not to play an important role, we do not take it into account. Our analysis, done with GLoBES [126, 127, 128], is based on ∼6000 un-oscillated events with reconstructed energies between 0.3 and 1.7 GeV, in both the neutrino and antineutrino modes. The oscillation parameters values assumed as the true ones are detailed in Table 5.1. The χ^2 analysis is similar to that explained in Sec. 5.1. In our analysis, the true event rates are simulated using the GENIE + νT calculations, and

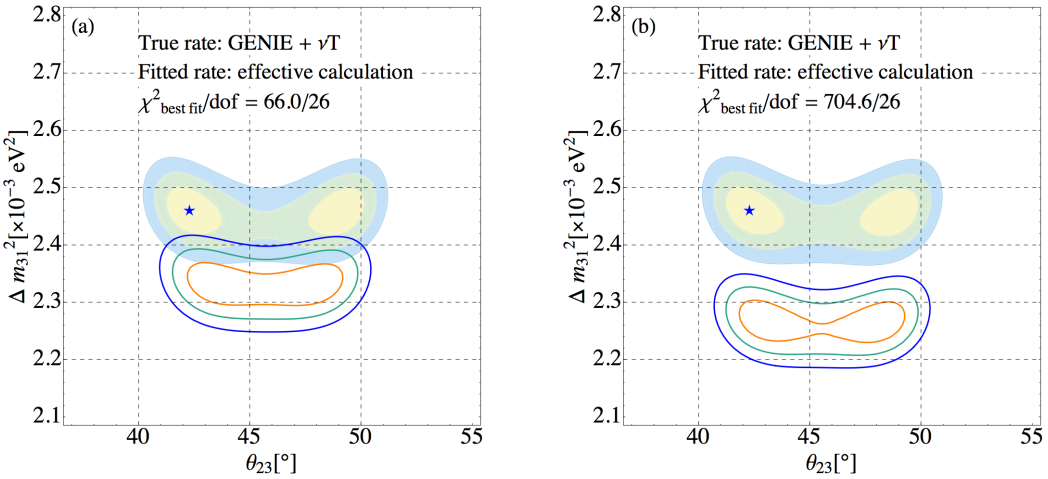

Figure 5.10: Confidence regions in the $(\theta_{23}, \Delta m^2_{31})$ plane for the true (a) ν_μ and (b) $\bar{\nu}_\mu$ event rates from GENIE + νT at the 1, 2 and 3σ C.L. The shaded areas (solid lines) correspond to the fitted rates from the GENIE + νT (effective) calculations.

the fitted rates are obtained for both considered approaches over a range of atmospheric oscillation parameters, θ_{23} and Δm^2_{31}. Having determined the minimal χ^2 value, $\chi^2_{\text{best-fit}}$, the confidence regions are found as in Eq. (5.4), but at 1, 2, and 3σ confidence level.
Before discussing the oscillation results, it is illustrative to compare the reconstructed energy distributions for muon neutrinos and antineutrinos obtained from the GENIE + νT and effective calculations. As shown in Fig. 5.8, the differences between the two cross-section estimates translate into differences between the oscillated event rates in the far detector, with the discrepancies being particularly severe in the case of antineutrinos.
In addition to the total event numbers, the two approaches yield clearly different distributions of reconstructed energy, as shown in Fig. 5.9 for the true energy $E_\nu = 0.6$ GeV. In the effective calculations, $2p2h$ processes enhance the low-energy tails of the distributions, while in the GENIE + νT approach, they also produce additional bumps, corresponding to the reconstructed energy $\sim$0.4 GeV at the kinematics of Fig. 5.9. In the antineutrino case, for $E_\nu \lesssim 1.4$ GeV the strength of these $2p2h$ bumps turns out to be larger than that of the QE ones, located at $E_\nu^{\text{rec}} \simeq E_\nu$. The observed differences in the reconstructed energy distributions have important consequences for the oscillation analysis.
The obtained confidence regions are shown in Fig. 5.10. The shaded areas represent the results for the GENIE + νT fitted rates, and the solid lines correspond to the fitted rates from the effective calculations. The high values of $\chi^2_{\text{best-fit}}$ per degree of freedom, given in Fig. 5.10, clearly indicate that the differences between the two considered approaches are too large to be neglected in a precise oscillation analysis. We have verified that this observation holds true even when the normalization of the QE event sample, with any number of nucleons, is treated as arbitrary. The results obtained rescaling the QE contribution are shown in Fig. 5.11. Therefore, the observed effect can be traced back to the shape discrepancies displayed in Figs. 5.6 and 5.9, which appear to be especially large for antineutrinos. In particular, as for antineutrinos in the relevant E_ν region the reconstructed energy distributions in the effective and GENIE + νT approaches are peaked at different

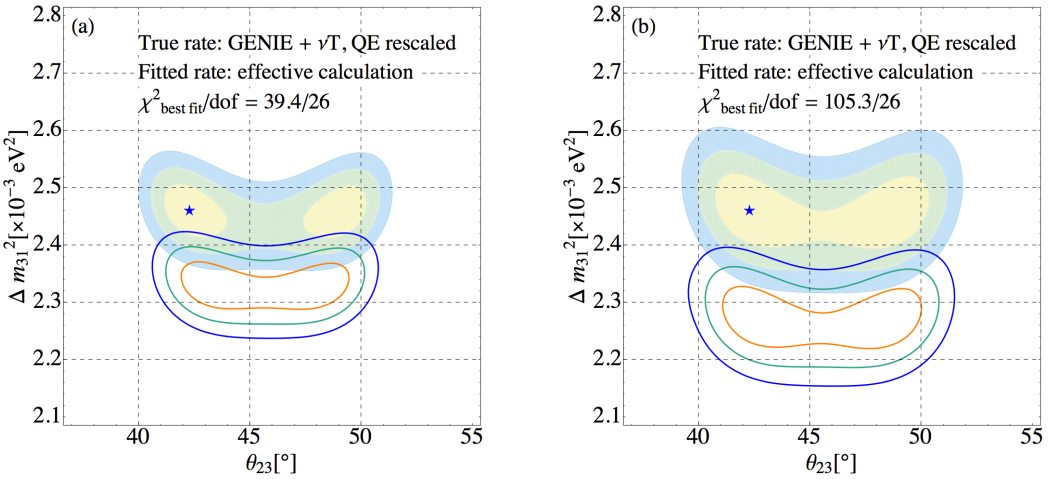

Figure 5.11: Same as Fig. 5.10, but using GENIE + νT with the QE contribution rescaled.

values, the extracted Δm^2_{31} is subject to larger bias for antineutrinos than for neutrinos.
In summary, we have studied the impact of discrepancies between experimental cross sections on neutrino-oscillation analysis, adopting the kinematic method of energy reconstruction. We have compared two data-driven approaches focusing on the 1 GeV energy region and shown that the differences between them have a sizable effect on the resulting oscillation parameters, especially in the antineutrino channel.
In view of these findings, improving the precision of the neutrino and antineutrino cross sections will be of great importance for future oscillation studies. Such progress will require new experimental data for neutrino energies $\sim$1 GeV, as well as an improvement in the understanding of systematic uncertainties, which would allow the tensions between existing measurements to be significantly alleviated.
Because the description of final-state hadrons involves larger uncertainties than those associated with leptons, the conclusions of this analysis are expected to also apply to the calorimetric method of energy reconstruction and are, therefore, relevant to the next generation of long-baseline oscillation measurements, such as the DUNE [52], aimed at determining the charge-parity violating phase and at verification of the three-neutrino paradigm.

Conclusions

In this Thesis we have studied two of the most important sources of systematic uncertainties in neutrino oscillation analysis. We evaluated the charged-current neutrino-carbon cross section using a realistic spectral function—taking into account, for the first time, all relevant interaction channels—to analyze nuclear effects, and studied the effects of neutrino energy reconstruction in long-baseline oscillation experiments.

Charged-current neutrino-nucleus interactions have been computed in the quasi-elastic, resonance production and deep inelastic sectors. We described the nuclear response within the Impulse Approximation, which is known to provide accurate results at momentum transfer exceeding few hundreds MeV. This approach allows to express the neutrino-nucleus cross section in any channels, as the convolution of the elementary cross section on individual nucleons and the Spectral Function, which describes the probability of removing from the nucleus a nucleon with a given momentum, leaving the residual system with a given excitation energy.

Being an intrinsic property of the target nucleus, the Spectral Function can be evaluated within non relativistic many-body theory using realistic phenomenological hamiltonian. In this way it is possible to account for nucleon-nucleon correlations, neglected in Fermi gas model which is largely used in neutrino event generators.

In Chapter 3 we computed the cross section for a wide range of neutrino energies (up to 20 GeV), to cover the kinematical region relevant to many ongoing and planned experiments. The treatment of the quasi elastic cross section closely follows the procedure described in Refs. [54, 160], while the calculation of the cross section in the resonance production and deep inelastic channels using the spectral function formalism is one of the original contributions of this work.

While our model still needs to be validated through a detailed comparison between its results and inelastic electron scattering data, the availability of a formalism allowing to describe all relevant single nucleon knock out processes within a realistic description of nuclear dynamics should be regarded as an important new achievement. In this context, it has to be also mentioned that the spectral function formalism has been recently generalized to describe electron scattering processes involving two-nucleon currents, which are long known to provide a significant fraction of the quasi elastic cross section [136, 161].

The study of the impact of systematic uncertainties on the extraction of oscillation parameters has been performed analyzing neutrino events produced with the Monte Carlo event generator GENIE [101]. These events have been produced up to 8 GeV, within four different charged-current interaction channels: besides quasi elastic scattering, resonance production and deep inelastic scattering, we have included processes in which interactions involving two-nucleon currents lead to the appearance of final states with more than one

nucleon excited to the continuum.
We have analyzed neutrino energy reconstruction by using the kinematic and the calorimetric techniques. The first procedure, in which the energy distribution is determined from the kinematics of the outgoing charged lepton, is mostly applied to analyze quasi elastic events, identified by the absence of pions in the final state. Using the calorimetric reconstruction, on the other hand, the neutrino energy is deduced from the energy deposited in the calorimeters by all reaction products. A key element of our analysis are the migration matrices, presented in Chapter 4, which enclose the probability that an event with a true neutrino energy ends up to be reconstructed in a different energy bin.
In Chapter 5 we have shown the results obtained from three different phenomenological studies, aimed at understanding the level of accuracy required for

- the estimation of detector capabilities,
- the estimation of the missing energy,
- the description of multi-nucleon effects in the QE region,

to avoid a large bias in the extraction of the oscillation parameters.
In the first analysis, we compared the two reconstruction techniques discussed above performing an analysis in the disappearance channel for the evaluation of the atmospheric parameters. We considered two approaches for neutrino event reconstruction: a *perfect scenario*, in which all produced particles are detected and their true energies are measured, and a *realistic scenario*, where realistic detector capabilities are taken into account. The observed event rates have been computed taking into account realistic detector capabilities. To quantify when the incorrect estimation of the detector performance starts to have a significant impact on the fit, we used a linear combination of perfect and realistic matrices.
This analysis showed that detector capabilities have to be understood at a 10% level or better, to avoid a significant bias in the measurement of Δm^2, using the calorimetric reconstruction. On the other hand, the kinematic reconstruction performs well even for pion-production events, but it strongly relies on an accurate understanding of neutrino-nucleus interactions.
The study of the impact of the correct estimation of the missing energy on the CP-violating phase has been performed in the appearance channel. Neutrino events have been reconstructed using the calorimetric method, and the analysis has been performed similarly to the previous case. However, the fit was performed using a linear combination of realistic matrices and gaussian distributions, centered around the true neutrino energy and with a width dependent on the energy smearing of the different particles observed. The results obtained suggest that an underestimation of missing energy by as little as 20% may result in a bias of around 1σ in the extracted value of the CP-violating phase.
The final analysis that we performed was dedicated to estimate the impact of $2p2h$ uncertainties on a disappearance experiment. To account for multi-nucleon mechanisms we considered an effective approach which consists of using an increased value of the axial mass, $M_A = 1.2$ GeV. In the second case $2p2h$ are simulated according to the model implemented in the event generator GENIE. The obtained results show that the differences

between the two data-driven approaches have a sizable effect on the evaluation of the oscillation parameters, confirming the need of using more realistic and sophisticated model to describe neutrino interactions.
As a final remark, it has to be pointed out that the ultimate goal of the project developed for this Thesis is the construction of a fully consistent description of neutrino-nucleus interactions, taking into account all reaction mechanisms relevant to ongoing and future experiment. The spectral function formalism appears to be ideally suited to pursue this goal, because it can be readily generalized to include contributions arising from two-nucleon currents. The extension of the study of Refs. [136, 161] to the case of charged-current weak interactions will make it possible a truly consistent treatment of all reaction mechanisms contributing to the neutrino-nucleus cross section.

Acknowledgments

I would like to express my special appreciation and thanks to my advisors, Prof. Omar Benhar and Dr. Davide Meloni. I am indebted to them for the continuous support during my Ph.D. studies, for their patience, motivation and knowledge. Their guidance helped me during these years of research and in writing this Thesis.
I am grateful to Artur Ankowski and Camillo Mariani for the many helpful discussions and the work carried out together. I would like to thank Pilar Coloma, Patrick Huber and Chun-Min Jen for our collaboration and for the work done together.
I am thankful to my friends and colleagues, Danilo Latini, Angela Mecca, Pietro Pugliese and Noemi Rocco who have accompanied me in these years in a mixture of lightheartedness and anxiety. In particular, I am grateful to Andrea Di Iura for the support and the friendship of many years.
I would like to thank my family for all their love and encouragement, in particular my parents who have always been by my side and for having always supported me.
A special thought goes to my dear grandparents.

Appendix A

Notation

In this Appendix we summarize the notation used in this Thesis to describe neutrino scattering via charged current. The neutrino-nucleon interaction process is denoted as

$$\nu_\ell(k) + N(p) \to \ell^-(k') + X(p') \ , \tag{A.1}$$

where the neutrino with a defined flavor ℓ scatters off the nucleon N, leading to a final state given by the produced associated charged lepton ℓ^- and a generic hadronic state X. The schematic representation of the neutrino-nucleon scattering in charged-current is shown in Fig. A.1.

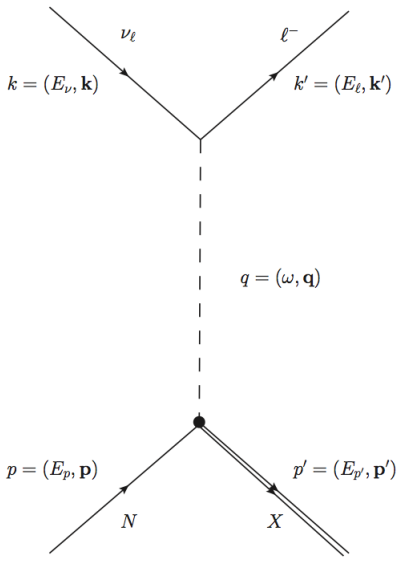

Figure A.1: Schematic representation of neutrino interaction in charged current.

In the figure the four-momenta of the particles involved in the interaction process are also

indicated, that is

$$k = (E_\nu, \mathbf{k}) \ , \qquad \text{Incoming neutrino,} \tag{A.2}$$
$$k' = (E_\ell, \mathbf{k}') \ , \qquad \text{Outgoing charged lepton,} \tag{A.3}$$
$$p = (E_p, \mathbf{p}) \ , \qquad \text{Nucleon target,} \tag{A.4}$$
$$p' = (E_{p'}, \mathbf{p}') \ , \qquad \text{Hadronic final state,} \tag{A.5}$$
$$q = (\omega, \mathbf{q}) \ , \qquad \text{Four-momentum transferred.} \tag{A.6}$$

The four-momentum transferred is such that

$$q^2 = (k - k')^2 = (p' - p)^2 = -Q^2 \ . \tag{A.7}$$

Similarly, the neutrino-nucleus scattering process

$$\nu_\ell(k) + A(P_0) \to \ell^-(k') + X(P_X) \tag{A.8}$$

is described by the same four-momenta for the leptons, and the initial nuclear ground state is given by

$$P_0 = (M_A, \mathbf{0}) \ , \tag{A.9}$$

being considered at rest. The hadronic final state X is instead described by

$$X \ \Rightarrow \ x(p') + R(p_R) \ , \tag{A.10}$$

where $x(p')$ represents the hadrons produced in final state, and $R(p_R)$ the residual system, with

$$p_R = (E_R, -\mathbf{p}) \ . \tag{A.11}$$

The recoil momentum of the system is denoted as $-\mathbf{p}$, to allow the interpretation of $\mathbf{p}$ as the vector sum of the initial momenta of the knocked-out nucleons.
A similar notation has been applied in Chapter 4 when we analyze neutrino interactions in order to evaluate the neutrino energy. In particular, we decomposed the hadrons produced in final state between nucleons and mesons

$$x \ \Rightarrow N(p') + M(h') \ , \tag{A.12}$$
$$p'_i = (E_{\mathbf{p}'_i}, \mathbf{p}'_i) \ , \tag{A.13}$$
$$h'_i = (E_{\mathbf{h}'_i}, \mathbf{h}'_i) \ , \tag{A.14}$$

where N is the state describing the n nucleons knocked-out from the nucleus with four-momenta p'_i, and M represents the state of the produced m mesons with four-momenta h'_i. The energy E_R of the residual system of $(A - n)$-nucleons, can be indicated also with the explicit notation E_{A-n}.

Appendix B

Leptonic Tensor

In this Appendix we report the general expression for the L_i, components of the leptonic tensor, introduced in Sec. 2.1. They are given by

$$L_1 = \frac{M^2}{2}(m_\ell^2 - q^2) \ , \tag{B.1}$$

$$L_2 = (E_\nu E_p - k_x p_x - k_z p_z)(E_\ell E_p - k'_x p_x - k'_z p_z) - \frac{1}{2}\frac{M^2}{2}(m_\ell^2 - q^2) = \tag{B.2}$$
$$= E_\nu E_\ell E_p^2 - E_\nu E_p k'_x p_x - E_\nu E_p k'_z p_z - E_\ell E_p k_x p_x + k_x k'_x p_x^2 + k_x k'_z p_x p_z +$$
$$- E_\ell E_p k_z p_z + k_z p_z k'_x p_x + k_z k'_z p_z^2 - \frac{1}{2}\frac{M^2}{2}(m_\ell^2 - q^2) \ ,$$

$$L_3 = \frac{1}{2}[(E_\nu E_p - k_x p_x - k_z p_z)(E_\ell \omega - k'_z |\mathbf{q}|) - (E_\ell E_p - k'_x p_x - k'_z p_z)(E_\nu \omega - k_z |\mathbf{q}|)] = \tag{B.3}$$
$$= \frac{1}{2}[E_\nu E_p E_\ell \omega - E_\nu E_p k'_z |\mathbf{q}| - k_x p_x E_\ell \omega + k_x k'_z p_x |\mathbf{q}| - k_z p_z E_\ell \omega + k_z k'_z |\mathbf{q}| p_z +$$
$$- E_p E_\ell E_\nu \omega + E_\ell E_p k_z |\mathbf{q}| + k'_x p_x E_\nu \omega - k_z k'_x p_x |\mathbf{q}| + k'_z p_z E_\nu \omega - k'_z k_z p_z |\mathbf{q}|] \ ,$$

$$L_4 = (E_\nu \omega - k_z |\mathbf{q}|)(E_\ell \omega - k'_z |\mathbf{q}|) - \frac{\omega^2 - |\mathbf{q}|^2}{2}\frac{1}{2}(m_\ell^2 - q^2) = \tag{B.4}$$
$$= E_\nu E_\ell \omega^2 - E_\nu \omega k'_z |\mathbf{q}| - E_\ell \omega k_z |\mathbf{q}| + k_z k'_z |\mathbf{q}|^2 - \frac{\omega^2 - |\mathbf{q}|^2}{2}\frac{1}{2}(m_\ell^2 - q^2) \ ,$$

$$L_5 = (E_\ell E_p - k'_x p_x - k'_z p_z)(E_\nu \omega - k_z |\mathbf{q}|) + (E_\nu E_p - k_x p_x - k_z p_z)(E_\nu \omega - k_z |\mathbf{q}|) + \tag{B.5}$$
$$- \frac{1}{2}(m_\ell^2 - q^2)(E_p \omega - p_z |\mathbf{q}|) =$$
$$= E_p E_\ell E_\nu \omega - E_p E_\ell k_z |\mathbf{q}| - k_x p_x E_\nu \omega + k_x p_x k_z |\mathbf{q}| - k'_z p_z E_\nu \omega + k'_z p_z k_z |\mathbf{q}| + E_\nu E_p E_\ell \omega +$$
$$- E_\nu E_p k'_z |\mathbf{q}| - k_x p_x E_\ell \omega + k_x p_x k'_z |\mathbf{q}| - k_z p_z E_\ell \omega + k_z k'_z p_z |\mathbf{q}| - \frac{1}{2}(m_\ell^2 - q^2)(E_p \omega - p_z |\mathbf{q}|) \ .$$

Being W the invariant mass of the final state and γ the angle between $\mathbf{p}$ and $\mathbf{q}$, it is possible to rewrite p_x and p_z as

$$W^2 = p^2 + q^2 + 2p\cdot q = (E_p+\omega)^2 - |\mathbf{p}|^2 - |\mathbf{q}|^2 - 2|\mathbf{p}||\mathbf{q}|\cos\gamma \ , \tag{B.6}$$

$$\cos\gamma = \frac{(E_p+\omega)^2 - |\mathbf{p}|^2 - |\mathbf{q}|^2 - W^2}{2|\mathbf{p}||\mathbf{q}|} \Rightarrow \ , \tag{B.7}$$

$$p_\perp = |\mathbf{p}|\sin\gamma \qquad \Rightarrow \qquad p_x = \frac{1}{\sqrt{2}}|\mathbf{p}|\sin\gamma \ , \tag{B.8}$$

$$p_z = |\mathbf{p}|\cos\gamma \ . \tag{B.9}$$

For the neutrino-nucleus scattering, the elementary cross section is weighted by the Spectral Function (see Chapter 3). In this case the integration in Eq. (3.20) over linear terms in p_x is zero, and $q \to \tilde{q}$, thus the L_i are simplified as

$$L_1 = \frac{M^2}{2}(m_\ell^2 - q^2) \ , \tag{B.10}$$

$$L_2 = E_\nu E_\ell \left[E_p^2 - E_p p_z \left(\frac{k_z}{E_\nu} + \frac{k'_z}{E_\ell} \right) + p_x^2 \frac{k_x^2}{E_\nu E_\ell} + p_z^2 \frac{k_z k'_z}{E_\nu E_\ell} \right] - \frac{1}{2}\frac{M^2}{2}(m_\ell^2 - q^2) \ , \tag{B.11}$$

$$L_3 = E_\nu E_\ell (E_p(p_z+q_z) - E_p p_z)\left(\frac{k_z}{E_\nu} - \frac{k'_z}{E_\ell} \right) \ , \tag{B.12}$$

$$L_4 = E_\nu E_\ell \left[\tilde{\omega}^2 - \tilde{\omega}|\mathbf{q}|\left(\frac{k_z}{E_\nu} + \frac{k'_z}{E_\ell} \right) + |\mathbf{q}|^2 \frac{k_z}{E_\nu}\frac{k'_z}{E_\ell} - \frac{\tilde{q}^2}{2}\left(1 - \frac{|\mathbf{k}'|}{E_\ell}\cos\theta_\ell \right) \right] \ , \tag{B.13}$$

$$\begin{aligned} L_5 = E_\nu E_\ell \Bigg[& 2E_p\tilde{\omega} + 2p_z q_z \frac{k_z}{E_\nu}\frac{k'_z}{E_\ell} - (E_p q_z + \tilde{\omega} p_z)\left(\frac{k_z}{E_\nu} + \frac{k'_z}{E_\ell} \right) + \\ & - (E_p\tilde{\omega} - p_z q_z)\left(1 - \frac{|\mathbf{k}'|}{E_\ell}\cos\theta_\ell \right) \Bigg] \ , \end{aligned} \tag{B.14}$$

where we can rewrite further the terms

$$\frac{k_z}{E_\nu} = \frac{\mathbf{k}\cdot\mathbf{q}}{E_\nu|\mathbf{q}|} = \frac{\omega}{|\mathbf{q}|} - \frac{k\cdot q}{E_\nu|\mathbf{q}|} \ , \qquad k\cdot q = k(k-k') = -k\cdot k' \ , \tag{B.15}$$

$$\frac{k'_z}{E_\ell} = \frac{\omega}{|\mathbf{q}|} - \frac{k'\cdot q}{E_\ell|\mathbf{q}|} \ , \qquad k'\cdot q = k(k-k') = k\cdot k' - m_\ell^2 \ . \tag{B.16}$$

Appendix C

Structure Functions for the Δ-resonance

In this Appendix we report the structure functions obtained for the Δ excitation, following the procedure shown in Sec. 2.3, taken from [62, 63]. The W_i have been computed using the FeynCalc tool [162, 163] of the software Mathematica [164]. Terms proportional to A_3 have been neglected, due to the fact that it has been set to be equal to zero.

$$
\begin{aligned}
W_1 = & \frac{4\mathrm{A}_4^2}{M^4}(p\cdot q - Q^2)^2(M^2 + M\mathrm{M}' + p\cdot q) + \\
& + \frac{8\mathrm{A}_4\mathrm{A}_5(p\cdot q - Q^2)(M^2 + M\mathrm{M}' + p\cdot q)}{M^2} + 4\mathrm{A}_5^2(M^2 + M\mathrm{M}' + p\cdot q) \\
& + \frac{4\mathrm{C}_3^2}{M^2\mathrm{M}'^2}[M^2\mathrm{M}'^2Q^2 + M^2(p\cdot q)^2 - 2M^2(p\cdot q)Q^2 + M^2Q^4 + M\mathrm{M}'^3Q^2 + \mathrm{M}'^2(p\cdot q)^2 + \\
& + (p\cdot q)^3 - 2(p\cdot q)^2Q^2 + (p\cdot q)Q^4] + \frac{4\mathrm{C}_3\mathrm{C}_4}{M^3\mathrm{M}'}(p\cdot q - Q^2)[M^2(p\cdot q) - M^2Q^2 \\
& - 2M\mathrm{M}'(p\cdot q) + 2M\mathrm{M}'Q^2 + \mathrm{M}'^2(p\cdot q) + (p\cdot q)^2 - (p\cdot q)Q^2] + \frac{4\mathrm{C}_3\mathrm{C}_5}{M^3\mathrm{M}'}p\cdot q \\
& [M^2p\cdot q - M^2Q^2 - 2M\mathrm{M}'p\cdot q + 2M\mathrm{M}'Q^2 + \mathrm{M}'^2p\cdot q + (p\cdot q)^2 - p\cdot qQ^2] + \\
& + \frac{4\mathrm{C}_4^2(p\cdot q - Q^2)^2(M^2 - M\mathrm{M}' + p\cdot q)}{M^4} + \frac{4\mathrm{C}_5^2p\cdot q^2(M^2 - M\mathrm{M}' + p\cdot q)}{M^4} \\
& + \frac{8\mathrm{C}_4\mathrm{C}_5p\cdot q(p\cdot q - Q^2)(M^2 - M\mathrm{M}' + p\cdot q)}{M^4}\,,
\end{aligned}
\tag{C.1}
$$

$$
\begin{aligned}
W_2 = & M^2\Bigg[\frac{4\mathrm{A}_4^2Q^2(M^2 + M\mathrm{M}' + (p\cdot q))}{M^4} + \frac{4\mathrm{A}_5^2(M^2 + M\mathrm{M}' + (p\cdot q))}{\mathrm{M}'^2} + \\
& + \frac{4\mathrm{C}_3^2Q^2(M^2 + \mathrm{M}'^2 + (p\cdot q))}{M^2\mathrm{M}'^2} + \frac{4\mathrm{C}_3\mathrm{C}_4Q^2(M^2 - 2M\mathrm{M}' + \mathrm{M}'^2 + (p\cdot q))}{M^3\mathrm{M}'} + \\
& + \frac{4\mathrm{C}_3\mathrm{C}_5Q^2(M^2 - 2M\mathrm{M}' + \mathrm{M}'^2 + (p\cdot q) + Q^2)}{M^3\mathrm{M}'} + \frac{4\mathrm{C}_4^2Q^2(M^2 - \mathrm{M}' + (p\cdot q))}{M^4} + \\
& + \frac{8\mathrm{C}_4\mathrm{C}_5Q^2(M^2 - M\mathrm{M}' + (p\cdot q))}{M^4} + \frac{4\mathrm{C}_5^2Q^2(\mathrm{M}'^2 + Q^2)(M^2 - M\mathrm{M}' + (p\cdot q))}{M^4\mathrm{M}'^2}\Bigg]\,,
\end{aligned}
\tag{C.2}
$$

$$W_3 = -\frac{8\mathrm{A}_4\mathrm{C}_3((p\cdot q)-Q^2)(-2M\mathrm{M}'-2\mathrm{M}'^2+(p\cdot q)-Q^2)}{M\mathrm{M}'}+ \tag{C.3}$$
$$+\frac{8\mathrm{A}_4\mathrm{C}_4((p\cdot q)-Q^2)^2}{M^2}+\frac{8\mathrm{A}_4\mathrm{C}_5(p\cdot q)((p\cdot q)-Q^2)}{M^2}+$$
$$+\frac{8\mathrm{A}_5\mathrm{C}_3M(2M\mathrm{M}'+2\mathrm{M}'^2-(p\cdot q)+Q^2)}{\mathrm{M}'}+8\mathrm{A}_5\mathrm{C}_4((p\cdot q)-Q^2)+8\mathrm{A}_5\mathrm{C}_5(p\cdot q)\ ,$$

$$W_4 =\frac{4\mathrm{A}_4^2(2(p\cdot q)-Q^2)(M^2+M\mathrm{M}'+(p\cdot q))}{M^2}+8\mathrm{A}_4\mathrm{A}_5(M^2+M\mathrm{M}'+(p\cdot q))+ \tag{C.4}$$
$$-\frac{8\mathrm{A}_4\mathrm{A}_6(p\cdot q)(M^2+M\mathrm{M}'+(p\cdot q))}{M^2}+\frac{4\mathrm{A}_5^2M^2(M^2+M\mathrm{M}'+(p\cdot q))}{\mathrm{M}'^2}+$$
$$-\frac{8\mathrm{A}_5\mathrm{A}_6(M^2+M\mathrm{M}'+(p\cdot q))(\mathrm{M}'^2-(p\cdot q)+Q^2)}{\mathrm{M}'^2}+$$
$$+\frac{4\mathrm{A}_6^2(M^2+M\mathrm{M}'+(p\cdot q))(\mathrm{M}'^2Q^2+(p\cdot q)^2-2(p\cdot q)Q^2+Q^4)}{M^2\mathrm{M}'^2}+$$
$$-\frac{4\mathrm{C}_3^2(M^2\mathrm{M}'^2-2M^2(p\cdot q)+M^2Q^2+M\mathrm{M}'^3-2(p\cdot q)^2+(p\cdot q)Q^2)}{\mathrm{M}'^2}+\frac{4\mathrm{C}_3\mathrm{C}_4}{M\mathrm{M}'}$$
$$(2M^2(p\cdot q)-M^2Q^2-4M\mathrm{M}'(p\cdot q)+2M\mathrm{M}'Q^2+\mathrm{M}'^2(p\cdot q)+2(p\cdot q)^2-(p\cdot q)Q^2)+$$
$$+\frac{4\mathrm{C}_3\mathrm{C}_5(p\cdot q)(M^2-2M\mathrm{M}'+2(p\cdot q))}{M\mathrm{M}'}+\frac{4\mathrm{C}_4^2(2(p\cdot q)-Q^2)(M^2-M\mathrm{M}'+(p\cdot q))}{M^2}+$$
$$+\frac{8\mathrm{C}_4\mathrm{C}_5(p\cdot q)(M^2-M\mathrm{M}'+(p\cdot q))}{M^2}-\frac{4\mathrm{C}_5^2(p\cdot q)^2(-M^2+M\mathrm{M}'-(p\cdot q))}{M^2\mathrm{M}'^2}\ ,$$

$$W_5 =\frac{8\mathrm{A}_4^2(p\cdot q)(M^2+M\mathrm{M}'+(p\cdot q))}{M^2}+8\mathrm{A}_4\mathrm{A}_5(M^2+M\mathrm{M}'+(p\cdot q))- \tag{C.5}$$
$$+\frac{8\mathrm{A}_4\mathrm{A}_6Q^2(M^2+M\mathrm{M}'+(p\cdot q))}{M^2}+\frac{8\mathrm{A}_5^2M^2(M^2+M\mathrm{M}'+(p\cdot q))}{\mathrm{M}'^2}+$$
$$+\frac{8\mathrm{A}_5\mathrm{A}_6((p\cdot q)-Q^2)(M^2+M\mathrm{M}'+(p\cdot q))}{\mathrm{M}'^2}+\frac{8\mathrm{C}_3^2(p\cdot q)(M^2+\mathrm{M}'^2+(p\cdot q))}{\mathrm{M}'^2}+$$
$$+\frac{8\mathrm{C}_3\mathrm{C}_4(p\cdot q)(M^2-2M\mathrm{M}'+\mathrm{M}'^2+(p\cdot q))}{M\mathrm{M}'}+\frac{8\mathrm{C}_4^2(p\cdot q)(M^2-M\mathrm{M}'+(p\cdot q))}{M^2}+$$
$$+\frac{8\mathrm{C}_3\mathrm{C}_5(p\cdot q)(M^2-2M\mathrm{M}'+\mathrm{M}'^2+(p\cdot q)+Q^2)}{M\mathrm{M}'}+$$
$$+\frac{8\mathrm{C}_5^2(p\cdot q)(\mathrm{M}'^2+Q^2)(M^2-M\mathrm{M}'+(p\cdot q))}{M^2\mathrm{M}'^2}$$
$$+\frac{16\mathrm{C}_4\mathrm{C}_5(p\cdot q)(M^2-M\mathrm{M}'+(p\cdot q))}{M^2}\ .$$

Appendix D

Kinematic formulas

The starting point is the reaction

$$\nu_\ell(k) + A(P_0) \to \ell^-(k') + N(p') + M(h') + R(p_R) \ ,$$

where N indicates a general final state of nucleons knocked out from the target A, while M denotes a generic state of mesons, and R is the residual nucleus (see Appendix A). Considering the production of n nucleons and m mesons, the energy and momentum conservation leads to

$$k + P_A = k' + p' + h' + p_R \ , \tag{D.1}$$

$$E_\nu + M_A = E_\ell + E_R + \sum_i^n E_{\mathbf{p}'_i} + \sum_j^m E_{\mathbf{h}'_j} \ , \tag{D.2}$$

$$\mathbf{k} = \mathbf{k}' + \sum_i^n \mathbf{p}'_i + \sum_j^m \mathbf{h}'_j - \mathbf{p} \ . \tag{D.3}$$

We can introduce the invariant hadronic mass of the hadrons produced in the final state, as

$$W^2 = (p' + h')^2 = \left(\sum_i^n E_{\mathbf{p}'_i} + \sum_j^m E_{\mathbf{h}'_j} \right)^2 - \left(\sum_i^n \mathbf{p}'_i + \sum_j^m \mathbf{h}'_j \right)^2 . \tag{D.4}$$

These equations lead to

$$\begin{aligned} &(M_A - E_R)^2 - \mathbf{p}^2 + E_\ell^2 - \mathbf{k}'^2 + 2E_\nu(M_A - E_R) - 2\mathbf{k}\cdot\mathbf{p} - 2E_\ell(M_A - E_R) + \\ &+ 2\mathbf{k}'\cdot\mathbf{p} - 2E_\nu E_\ell + 2\mathbf{k}\cdot\mathbf{k}' = W^2 \ , \\ &E_\nu(2(M_A - E_R) - 2E_\ell + 2|\mathbf{k}'|\cos\theta_\ell - 2|\mathbf{p}|\cos\theta_\mathbf{p}) + m_\ell^2 + ((M_A - E_R)^2 - \mathbf{p}^2) + \\ &- 2E_\ell(M_A - E_R) + 2\mathbf{k}'\cdot\mathbf{p} = W^2 \ . \end{aligned} \tag{D.5}$$

Thus the neutrino energy is given by

$$E_\nu = \frac{W^2 - m_\ell^2 + 2(M_A - E_R)E_\ell - ((M_A - E_R)^2 - \mathbf{p}^2) - 2\mathbf{p}\cdot\mathbf{k}'}{2((M_A - E_R) - E_\ell + |\mathbf{k}'|\cos\theta_\ell - |\mathbf{p}|\cos\theta_\mathbf{p})} \ , \tag{D.6}$$

with m_ℓ the lepton mass, $|\mathbf{p}|\cos\theta_{\mathbf{p}} = \mathbf{p}\cdot\mathbf{k}/E_\nu$ and $|\mathbf{k}'|\cos\theta_\ell = \mathbf{k}'\cdot\mathbf{k}/E_\nu$.
Notice that in the main text the more explicit notation $E_R = E_{A-n}$ is used.

Appendix E

Migration Matrices

In this Appendix we show the migration matrices, discussed in Sec. 4.4. We include here just the set of matrices obtained within the realistic scenario (see Sec. 4.3), comparing the calorimetric and kinematic reconstruction results.
The reconstructed events are generated using GENIE (see Sec. 4.2), for the different interaction channels taken into account, with carbon (^{12}C) as nuclear target. In the Figs. E.1 - E.4 we show the migration matrices obtained for quasi-elastic interaction, $2p2h$ processes, resonance production and deep inelastic scattering, respectively. In the figures the x-axis represents the true neutrino energy and the y-axis the reconstructed neutrino energy. Notice that the color bars in the figures have their maximum chosen between the maximal value among the two compared matrices.
Furthermore, Tab. E.1 represents the format of the migration matrices produced, and available in Refs. [118, 119].

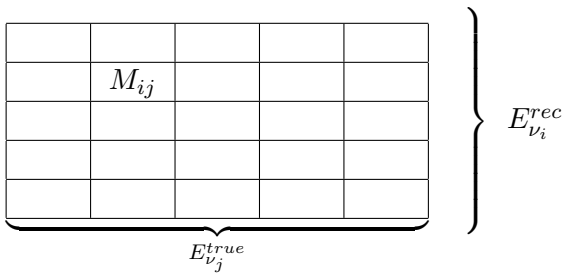

Table E.1: Format of the migration matrix. A migration matrix M_{ij} defines the probability for an event with true neutrino energy $E_{\nu_j}^{true}$ to be reconstructed with an energy $E_{\nu_i}^{rec}$

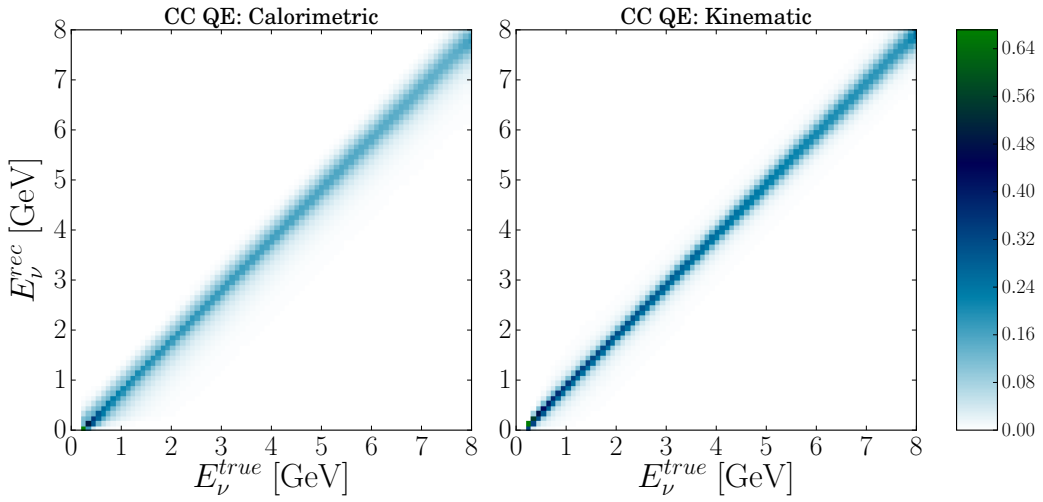

Figure E.1: Migration matrices obtained with calorimetric (left panel) and kinematic (right panel) reconstruction. The events in the QE interaction channel, produced with GENIE, are reconstructed using the realistic scenario.

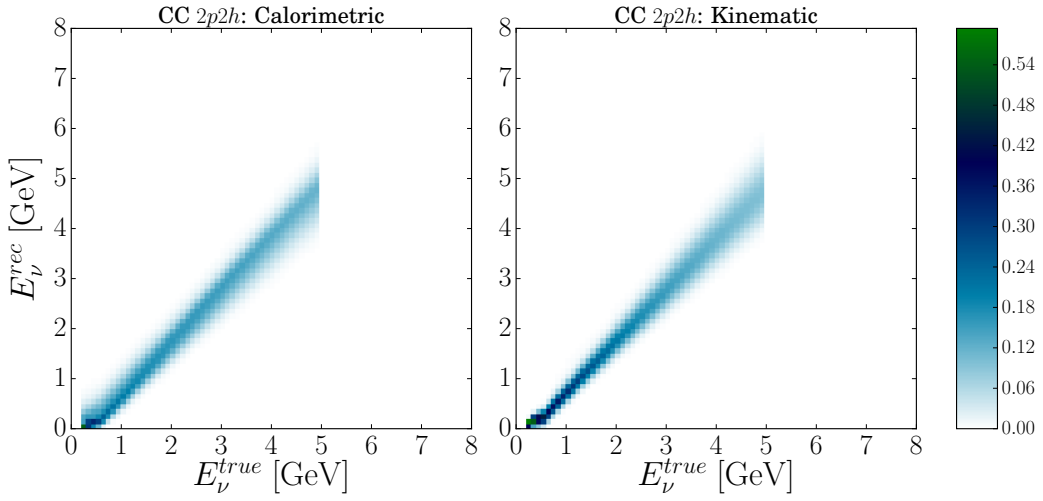

Figure E.2: The same as in Fig. E.1, but for $2p2h$ interactions.

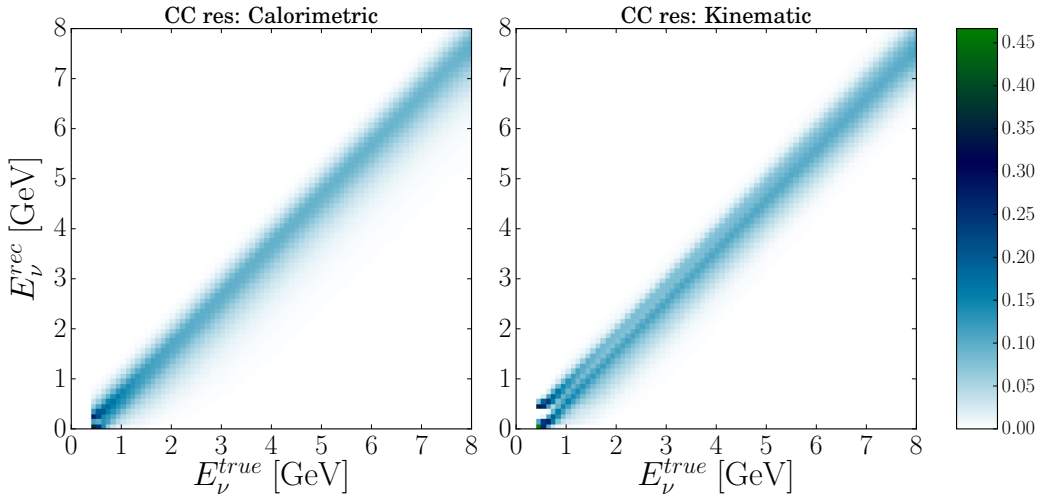

Figure E.3: The same as in Fig. E.1, but for resonance production.

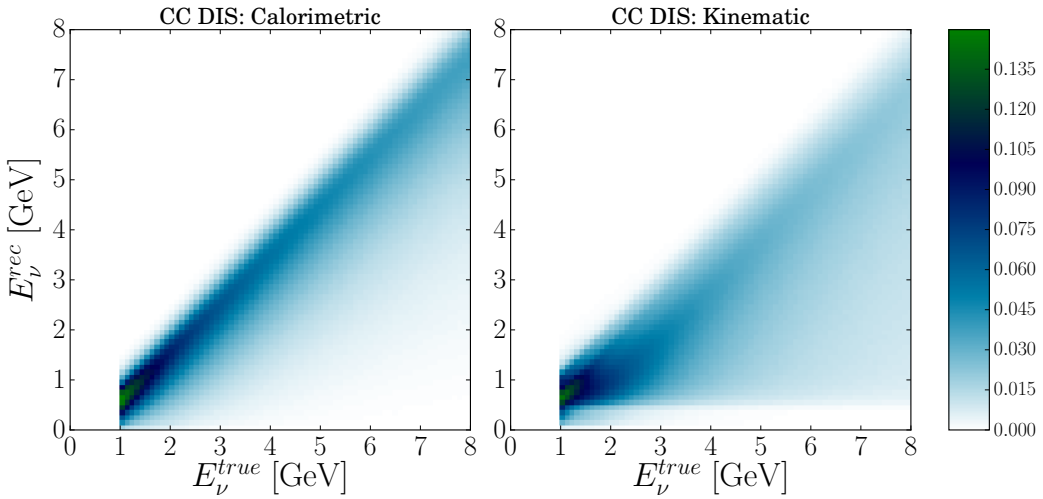

Figure E.4: The same as in Fig. E.1, but for deep inelastic scattering.

Appendix F

χ^2 analysis

The χ^2 analysis is performed to extract the oscillation parameters and relative confidence regions at $1, 2$ and 3σ confidence level (CL). The study follows Refs. [130] and [128], where the χ^2 analysis is reported in their appendix and for completeness, it is also discussed here below.

The χ^2 values, in the energy bin i and for the detector D is calculated as

$$\chi^2_{i,D} = 2\left(T_{i,D}(\theta,\xi) - O_{i,D} + O_{i,D} \ln \frac{O_{i,D}}{T_{i,D}(\theta,\xi)} \right) . \tag{F.1}$$

where D can be the near or the far detector.
The above formula depends on the effective *observed* event number $O_{i,D}$ computed with the assumed *true* oscillation parameters, and on the event number $T_{i,D}$ expected at the detector D and in the $i-$th energy bin, given by

$$T_{i,D}(\theta,\xi) = (1 + \xi_{\phi,i} + \xi_n) N_{i,D}(\theta,\xi) \ , \tag{F.2}$$

which depends on two different nuisance parameters ξ, and on the oscillation parameters θ used as test values. The parameter $\xi_{\phi,i}$ is linked to the flux uncertainties in the energy bin i, and it is bin to bin uncorrelated. The nuisance parameter ξ_n is associated to normalization uncertainties, that are bin to bin correlated. $N_{i,D}$ is the event number for a given energy bin computed with the test values θ for the detector D.
The true event number $O_{i,D}$ depends only on the oscillation values used as *true* input values.
The χ^2 is evaluated also including gaussian priors for each nuisance parameter included in the analysis. The final expression of the χ^2 is then obtained minimizing over the nuisance parameters ξ

$$\chi^2 = \min_{\xi} \left\{ \sum_{i,D} \chi^2_{i,D}(\theta,\xi) + \sum_i \left(\frac{\xi_{\phi_i}}{\sigma_\phi} \right)^2 + \left(\frac{\xi_n}{\sigma_n} \right)^2 \right\} \tag{F.3}$$

where σ_ξ are the gaussian priors uncertainties assumed for each systematic error.

Appendix G

Gaussian smearing

In this Appendix we explain the procedure used for the evaluation of the standard deviations of the gaussian distributions used for the analysis in Sec. 5.2.
The behavior of the standard deviation, as a function of true neutrino energy, can be fitted with a given function. The fitting function chosen is

$$\sigma(E_\nu) = a + b\sqrt{E_\nu} + cE_\nu \ , \quad \text{with} \quad a, b, c > 0 \ , \tag{G.1}$$

and E_ν in GeV. The above expression can be implemented in GLoBES in order to obtain a gaussian smearing for the energy resolution $R(E_\nu, E')$, in the form

$$R(E_\nu, E') = \frac{1}{\sigma(E_\nu)\sqrt{2\pi}} e^{-\dfrac{E_\nu - E'}{2\sigma^2(E_\nu)}} \ . \tag{G.2}$$

The standard deviations of the distributions obtained from the realistic migration matrices have been fitted using the function in Eq. (G.1) to obtain the parameters a, b and c. The results obtained in the different interaction channels, for electron neutrino ($\sigma^{\nu_e}(E_\nu)$) and antineutrino ($\sigma^{\bar{\nu}_e}(E_\nu)$), and E_ν in GeV, are

- Quasi-elastic interaction:

$$\sigma^{\nu_e}_{\mathrm{QE}}(E_\nu) = 0.26\sqrt{E_\nu} + 0.015E_\nu \ ,$$

$$\sigma^{\bar{\nu}_e}_{\mathrm{QE}}(E_\nu) = 0.014 + 0.13\sqrt{E_\nu} + 0.060E_\nu \ .$$

- Resonance production:

$$\sigma^{\nu_e}_{\mathrm{res}}(E_\nu) = 0.31\sqrt{E_\nu} + 0.0029E_\nu \ ,$$

$$\sigma^{\bar{\nu}_e}_{\mathrm{res}}(E_\nu) = 0.068 + 0.15\sqrt{E_\nu} + 0.043E_\nu \ .$$

- Deep inelastic scattering:

$$\sigma^{\nu_e}_{\mathrm{DIS}}(E_\nu) = 0.16 + 0.18E_\nu \ ,$$

$$\sigma^{\bar{\nu}_e}_{\mathrm{DIS}}(E_\nu) = 0.17\sqrt{E_\nu} + 0.10E_\nu \ .$$

- $2p2h$:

$$\sigma^{\nu_e}_{2p2h}(E_\nu) = 0.15 + 0.086 E_\nu \ ,$$
$$\sigma^{\bar{\nu}_e}_{2p2h}(E_\nu) = 0.090 + 0.10 E_\nu \ .$$

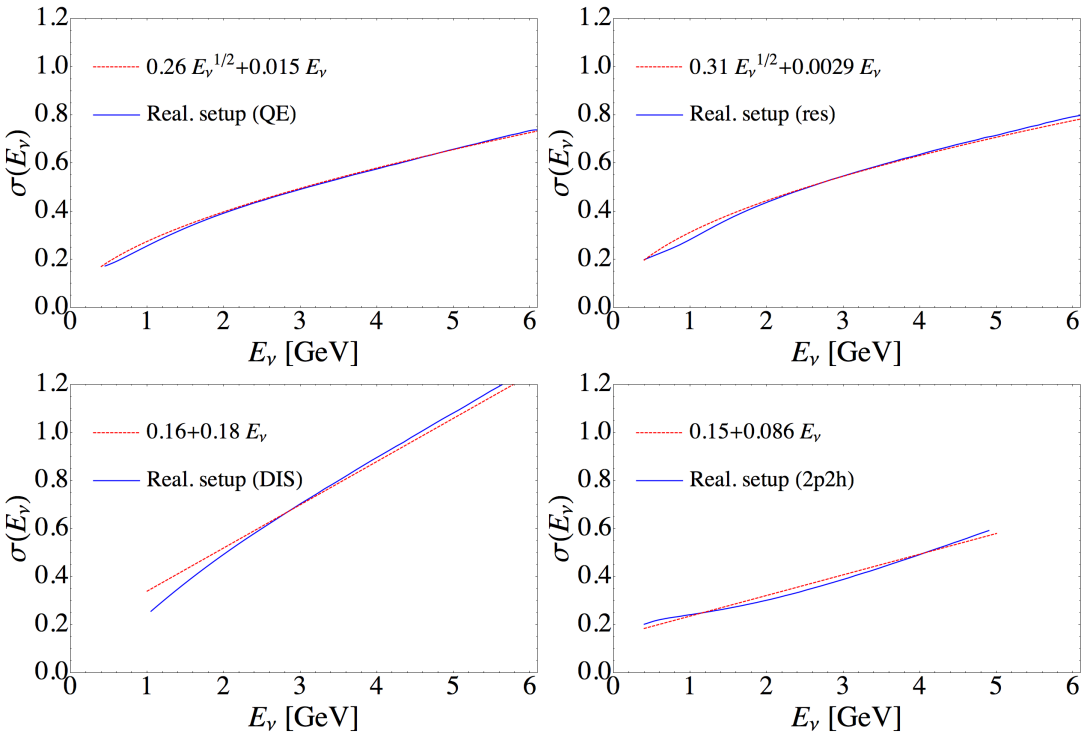

Figure G.1: Fit results for electron neutrino for the different interaction channels. The solid lines represent the standard deviation obtained from the realistic migration matrices, as a function of the neutrino energy. The dashed lines are obtained using Eq. (G.1) as fitting function.

The results of the different fits are shown in Figs. G.1 and G.2, for the different interaction channels, and for electron neutrino and anti-neutrino, respectively. In Fig. G.3, we compare the probability distribution functions for an event to be reconstructed with an energy E_{rec}, in the QE channel for ν_e at fixed true neutrino energy ($E_\nu = 1.45$ GeV). The two distributions are obtained using the migration matrices and a gaussian distribution with the same standard deviation of the matrices but centered around the true neutrino energy.

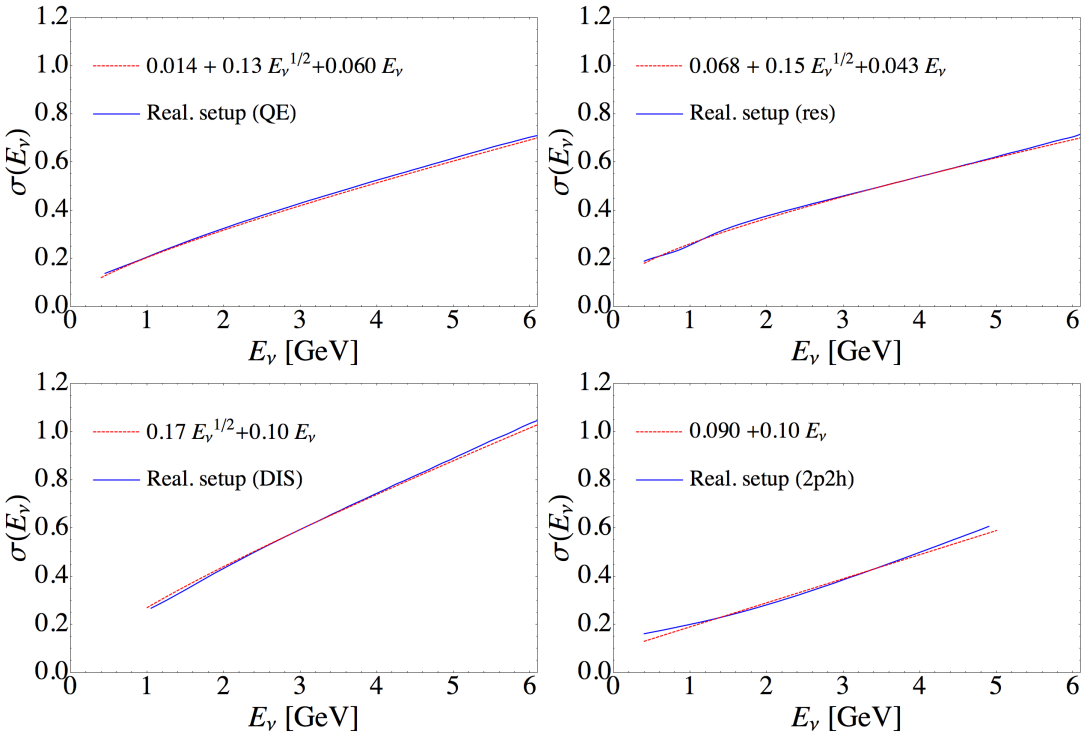

Figure G.2: The same as in Fig. G.1, but for electron anti-neutrino.

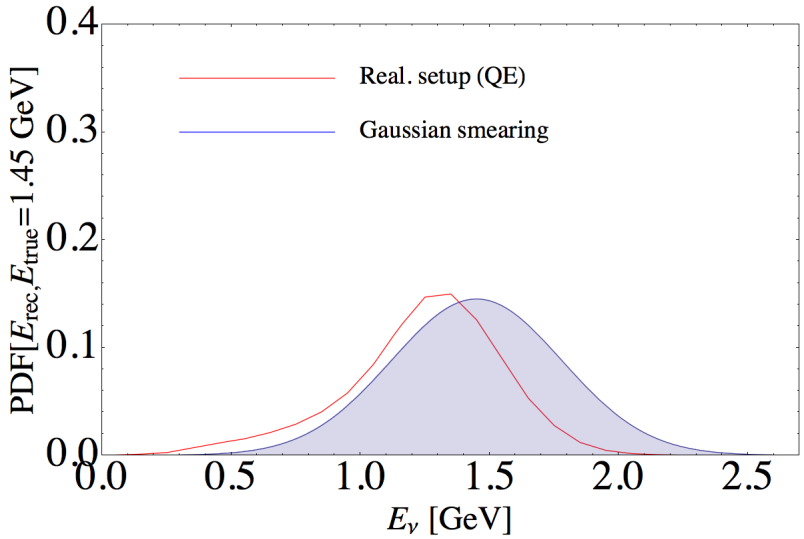

Figure G.3: Probability distribution function for an event to be reconstructed with an energy E_{rec}, given the true neutrino energy E_{true}.

Bibliography

[1] C. H. Llewellyn Smith. *Neutrino reactions at accelerator energies.* Physics Reports **3**, 261 (1972).

[2] O. Benhar and N. Rocco. *Nuclear Effects in Neutrino Interactions and Their Impact on the Determination of Oscillation Parameters.* Adv. High Energy Phys. **2013**, 912702 (2013).

[3] U. Mosel. *Neutrino Interactions with Nucleons and Nuclei: Importance for Long-Baseline Experiments.* Ann. Rev. Nucl. Part. Sci. **66**, 171 (2016).

[4] M. Peskin and D. Schroeder, *An introduction to quantum field theory* (Addison-Wesley Publishing Company, USA, 1995), p. 842.

[5] C. Itzykson and J.-B. Zuber, *Quantum field theory* (Courier Corporation, Mineola (NY), USA, 2006), p. 705.

[6] F. Mandl and G. Shaw, *Quantum field theory* (John Wiley & Sons, West Sussex, UK, 2010), p. 496.

[7] L. Maiani and O. Benhar, *Relativistic Quantum Mechanics: An Introduction to Relativistic Quantum Fields* (CRC Press, Boca Raton (FL), USA, 2015), p. 310.

[8] V. M. Lobashev. *The search for the neutrino mass by direct method in the tritium beta-decay and perspectives of study it in the project KATRIN.* Nucl. Phys. A **719**, 153 (2003).

[9] C. Giunti and C. W. Kim, *Fundamentals of Neutrino Physics and Astrophysics* (Oxford University Press, Oxford, UK, 2007), p. 710.

[10] C. Patrignani and others (Particle Data Group). *Review of Particle Physics.* Chin. Phys. C **40**, 100001 (2016).

[11] E. Majorana. *Teoria simmetrica dell'elettrone e del positrone.* Il Nuovo Cimento (1924-1942) **14**, 171 (1937).

[12] C. Jarlskog. *Commutator of the Quark Mass Matrices in the Standard Electroweak Model and a Measure of Maximal CP Violation.* Phys. Rev. Lett. **55**, 1039 (1985).

[13] L. Wolfenstein. *Neutrino Oscillations in Matter.* Phys. Rev. D **17**, 2369 (1978).

[14] S. P. Mikheev and A. Yu. Smirnov. *Resonance Amplification of Oscillations in Matter and Spectroscopy of Solar Neutrinos.* Sov. J. Nucl. Phys. **42**, 913 (1985).

[15] E. K. Akhmedov, R. Johansson, M. Lindner, T. Ohlsson, and T. Schwetz. *Series expansions for three flavor neutrino oscillation probabilities in matter.* JHEP **04**, 078 (2004).

[16] A. Cervera, A. Donini, M. B. Gavela, J. J. Gomez Cadenas, P. Hernandez, O. Mena, and S. Rigolin. *Golden measurements at a neutrino factory.* Nucl. Phys. B **579**, 17 (2000).

[17] R. Davis Jr, D. S. Harmer, and K. C. Hoffman. *Search for neutrinos from the sun.* Phys. Rev. Lett. **20**, 1205 (1968).

[18] J. Abdurashitov et al. *Measurement of the solar neutrino capture rate with gallium metal. III. Results for the 2002–2007 data-taking period.* Phys. Rev. C **80**, 015807 (2009).

[19] P. Anselmann et al. *Solar neutrinos observed by GALLEX at Gran Sasso.* Phys. Lett. B **285**, 376 (1992).

[20] M. Altmann et al. *Complete results for five years of GNO solar neutrino observations.* Phys. Lett. B **616**, 174 (2005).

[21] K. S. Hirata et al. *Observation of* ^{8}B *solar neutrinos in the Kamiokande-II detector.* Phys. Rev. Lett. **63**, 16 (1989).

[22] K. Eguchi et al. *First results from KamLAND: evidence for reactor antineutrino disappearance.* Phys. Rev. Lett. **90**, 021802 (2003).

[23] Q. R. Ahmad et al. (SNO Collaboration). *Measurement of the rate of* $\nu_e + d \rightarrow p + p + e^-$ *interactions produced by* ^{8}B *solar neutrinos at the Sudbury Neutrino Observatory.* Phys. Rev. Lett. **87**, 071301 (2001).

[24] G. Alimonti et al. (Borexino Collaboration). *The Borexino detector at the Laboratori Nazionali del Gran Sasso.* Nucl. Instrum. Meth. A **600**, 568 (2009).

[25] Y. Fukuda et al. *Evidence for oscillation of atmospheric neutrinos.* Phys. Rev. Lett. **81**, 1562 (1998).

[26] M. Ahn et al. *Indications of neutrino oscillation in a 250 km long-baseline experiment.* Phys. Rev. Lett. **90**, 041801 (2003).

[27] D. Michael et al. *Observation of muon neutrino disappearance with the MINOS detectors in the NuMI neutrino beam.* Phys. Rev. Lett. **97**, 191801 (2006).

[28] K. Abe et al. *First muon-neutrino disappearance study with an off-axis beam.* Phys. Rev. D **85**, 031103 (2012).

[29] R. Acquafredda et al. *First events from the CNGS neutrino beam detected in the OPERA experiment.* New J. Phys. **8**, 303 (2006).

[30] K. Abe et al. *Indication of electron neutrino appearance from an accelerator-produced off-axis muon neutrino beam.* Phys. Rev. Lett. **107**, 041801 (2011).

[31] P. Adamson et al. *Measurements of atmospheric neutrinos and antineutrinos in the MINOS far detector.* Phys. Rev. D **86**, 052007 (2012).

[32] F. An et al. *Observation of electron-antineutrino disappearance at Daya Bay.* Phys. Rev. Lett. **108**, 171803 (2012).

[33] Y. Abe et al. *Indication of reactor* $\overline{\nu}_e$ *disappearance in the Double Chooz experiment.* Phys. Rev. Lett. **108**, 131801 (2012).

[34] J. K. Ahn et al. *Observation of reactor electron antineutrinos disappearance in the RENO experiment.* Phys. Rev. Lett. **108**, 191802 (2012).

[35] M. C. Gonzalez-Garcia, M. Maltoni, and T. Schwetz. *Updated fit to three neutrino mixing: status of leptonic CP violation.* JHEP **11**, 052 (2014).

[36] S. Dell'Oro, S. Marcocci, M. Viel, and F. Vissani. *Neutrinoless Double Beta Decay: 2015 Review.* Adv. High Energy Phys. **2016**, 2162659 (2016).

[37] K. Abe et al. *Measurement of Muon Antineutrino Oscillations with an Accelerator-Produced Off-Axis Beam.* Phys. Rev. Lett. **116**, 181801 (2016).

[38] P. Adamson et al. *First measurement of muon-neutrino disappearance in NO*ν*A.* Phys. Rev. D **93**, 051104 (2016).

[39] A. A. Aguilar-Arevalo et al. (MiniBooNE Collaboration). *Measurement of Muon Neutrino Quasielastic Scattering on Carbon.* Phys. Rev. Lett. **100**, 032301 (2008).

[40] A. A. Aguilar-Arevalo et al. (MiniBooNE Collaboration). *First Measurement of the Muon Neutrino Charged Current Quasielastic Double Differential Cross Section.* Phys. Rev. D **81**, 092005 (2010).

[41] A. A. Aguilar-Arevalo et al. (MiniBooNE Collaboration). *First measurement of the muon antineutrino double-differential charged-current quasielastic cross section.* Phys. Rev. D **88**, 032001 (2013).

[42] A. A. Aguilar-Arevalo et al. (MiniBooNE Collaboration). *Measurement of Neutrino-Induced Charged-Current Charged Pion Production Cross Sections on Mineral Oil at $E_\nu \sim 1$ GeV.* Phys. Rev. D **83**, 052007 (2011).

[43] K. Abe et al. (T2K Collaboration). *Measurement of the inclusive ν_μ charged current cross section on carbon in the near detector of the T2K experiment.* Phys. Rev. D **87**, 092003 (2013).

[44] G. A. Fiorentini et al. (MINERvA Collaboration). *Measurement of Muon Neutrino Quasielastic Scattering on a Hydrocarbon Target at $E_\nu \sim 3.5$ GeV.* Phys. Rev. Lett. **111**, 022502 (2013).

[45] B. Tice et al. *Measurement of Ratios of ν_μ Charged-Current Cross Sections on C, Fe, and Pb to CH at Neutrino Energies 2–20 GeV.* Phys. Rev. Lett. **112**, 231801 (2014).

[46] A. Higuera et al. *Measurement of Coherent Production of $\pi^\pm$ in Neutrino and Antineutrino Beams on Carbon from E_ν of 1.5 to 20 GeV.* Phys. Rev. Lett. **113**, 261802 (2014).

[47] T. Walton et al. *Measurement of muon plus proton final states in ν_μ interactions on hydrocarbon at $<E_\nu>= 4.2$ GeV.* Phys. Rev. D **91**, 071301 (2015).

[48] J. Mousseau et al. *Measurement of partonic nuclear effects in deep-inelastic neutrino scattering using MINERvA.* Phys. Rev. D **93**, 071101 (2016).

[49] Q. Wu et al. (NOMAD Collaboration). *A Precise measurement of the muon neutrino-nucleon inclusive charged current cross-section off an isoscalar target in the energy range $2.5 < E_\nu < 40$ GeV by NOMAD.* Phys. Lett. B **660**, 19 (2008).

[50] Y. Nakajima et al. (SciBooNE Collaboration). *Measurement of inclusive charged current interactions on carbon in a few-GeV neutrino beam.* Phys. Rev. D **83**, 012005 (2011).

[51] P. Adamson et al. (MINOS Collaboration). *Study of quasielastic scattering using charged-current ν_μ-iron interactions in the MINOS near detector.* Phys. Rev. D **91**, 012005 (2015).

[52] R. Acciarri et al. (DUNE Collaboration). *Long-Baseline Neutrino Facility (LBNF) and Deep Underground Neutrino Experiment (DUNE) Conceptual Design Report Volume 1: The LBNF and DUNE Projects.* `arXiv:1601.05471` (2016).

[53] R. Acciarri et al. *First measurement of neutrino and antineutrino coherent charged pion production on Argon.* Phys. Rev. Lett. **113**, 261801 (2014).

[54] O. Benhar and D. Meloni. *Total neutrino and antineutrino nuclear cross sections around 1 GeV.* Nucl. Phys. A **789**, 379 (2007).

[55] O. Benhar, N. Farina, H. Nakamura, M. Sakuda, and R. Seki. *Electron- and neutrino-nucleus scattering in the impulse approximation regime.* Phys. Rev. D **72**, 053005 (2005).

[56] O. Benhar, D. Day, and I. Sick. *Inclusive quasielastic electron-nucleus scattering.* Rev. Mod. Phys. **80**, 189 (2008).

[57] O. Benhar, P. Huber, C. Mariani, and D. Meloni. *Neutrino-nucleus interactions and the determination of oscillation parameters.* `arXiv:1501.06448` (2015).

[58] T. Leitner, O. Buss, L. Alvarez-Ruso, and U. Mosel. *Electron- and neutrino-nucleus scattering from the quasielastic to the resonance region.* Phys. Rev. C **79**, 034601 (2009).

[59] R. Bradford, A. Bodek, H. S. Budd, and J. Arrington. *A New parameterization of the nucleon elastic form-factors.* Nucl. Phys. Proc. Suppl. **159**, 127 (2006).

[60] J. J. Kelly. *Simple parametrization of nucleon form factors.* Phys. Rev. C **70**, 068202 (2004).

[61] W. Rarita and J. Schwinger. *On a theory of particles with half integral spin.* Phys. Rev. **60**, 61 (1941).

[62] O. Lalakulich and E. A. Paschos. *Resonance production by neutrinos: J = 3/2 resonances.* Phys. Rev. D **71**, 074003 (2005).

[63] O. Lalakulich, E. A. Paschos, and G. Piranishvili. *Resonance production by neutrinos: The Second resonance region.* Phys. Rev. D **74**, 014009 (2006).

[64] E. A. Paschos, J.-Y. Yu, and M. Sakuda. *Neutrino production of resonances.* Phys. Rev. D **69**, 014013 (2004).

[65] V. Burkert, R. De Vita, M. Battaglieri, M. Ripani, and V. Mokeev. *Single quark transition model analysis of electromagnetic nucleon resonance excitations in the [70, 1-] supermultiplet.* Phys. Rev. C **67**, 035204 (2003).

[66] I. Aznauryan, V. Burkert, H. Egiyan, K. Joo, R. Minehart, and L. Smith. *Electroexcitation of the P_{33} (1232), P_{11} (1440), D_{13} (1520), and S_{11} (1535) at Q^2= 0.4 and 0.65 $(GeV/c)^2$.* Phys. Rev. C **71**, 015201 (2005).

[67] L. Tiator, D. Drechsel, S. Kamalov, M. Giannini, E. Santopinto, and A. Vassallo. *Electroproduction of nucleon resonances.* Eur. Phys. Jour. A **19**, 55 (2004).

[68] M. Gorchtein, D. Drechsel, M. Giannini, E. Santopinto, and L. Tiator. *Generalized sum rules of the nucleon in the constituent quark model.* Phys. Rev. C **70**, 055202 (2004).

[69] R. G. Roberts, *The structure of the proton: deep inelastic scattering* (Cambridge University Press, Cambridge (NY), USA, 1990), p. 196.

[70] P. Renton, *Electroweak Interactions: An introduction to the Physics of quarks and leptons* (Cambridge University Press, Cambridge (NY), USA, 1999), p. 596.

[71] F. Halzen and A. D. Martin, *Quarks and leptons: An introduction course in modern particle Physics* (John Wiley & Sons, New York, USA, 1984), p. 396.

[72] A. Bodek et al. *Experimental Studies of the Neutron and Proton Electromagnetic Structure Functions.* Phys. Rev. **D20**, 1471 (1979).

[73] M. Glück, E. Reya, and A. Vogt. *Dynamical parton distributions revisited.* Eur. Phys. J. C **5**, 461 (1998).

[74] A. Bodek and J. Ritchie. *Fermi-motion effects in deep-inelastic lepton scattering from nuclear targets.* Phys. Rev. D **23**, 1070 (1981).

[75] W. B. Atwood and G. B. West. *Extraction of asymptotic nucleon cross sections from deuterium data.* Phys. Rev. D **7**, 773 (1973).

[76] S. Stein, W. B. Atwood, E. D. Bloom, R. L. A. Cottrell, H. DeStaebler, C. L. Jordan, H. G. Piel, C. Y. Prescott, R. Siemann, and R. E. Taylor. *Electron scattering at 4° with energies of 4.5-20 GeV.* Phys. Rev. D **12**, 1884 (1975).

[77] C. Adloff et al. *A measurement of the proton structure function $F_2(x, Q^2)$ at low x and low Q^2 at HERA.* Nucl. Phys. B **497**, 3 (1997).

[78] M. Derrick et al. *Measurement of the F_2 structure function in deep inelastic e^+p scattering using 1994 data from the ZEUS detector at HERA.* Zeitschrift für Physik C: Particles and Fields **72**, 399 (1996).

[79] E. Vagnoni, O. Benhar and D. Meloni. *Inelastic Neutrino-Nucleus Interactions within the Spectral Function Formalism.* `arXiv:1701.01718` (2017). Submitted to Physical Review Letters.

[80] H. Yukawa. *On the interaction of elementary particles. I.* Nippon Sugaku-Buturigakkwai Kizi Dai 3 Ki **17**, 48 (1935).

[81] A. L. Fetter and J. D. Walecka, *Quantum theory of many-particle systems* (Dover Publications, Inc., Mineola (NY), USA, 2003), p. 640.

[82] O. Benhar, A. Fabrocini, and S. Fantoni. *Nuclear-matter green functions in correlated-basis theory.* Nucl. Phys. A **550**, 201 (1992).

[83] O. Benhar, A. Fabrocini, and S. Fantoni. *The nucleon spectral function in nuclear matter.* Nucl. Phys. A **505**, 267 (1989).

[84] C. C. Degli Atti, E. Pace, and G. Salmè. *Realistic nucleon-nucleon interactions and the three-body electrodisintegration of* ^3H. Phys. Rev. C **21**, 805 (1980).

[85] A. Dieperink, T. De Forest, I. Sick, and R. Brandenburg. *Quasi-elastic electron scattering on* ^3He. Phys. Lett. B **63**, 261 (1976).

[86] H. Meier-Hajduk, C. Hajduk, P. Sauer, and W. Theis. *Quasi-elastic electron scattering from* ^3He. Nucl. Phys. A **395**, 332 (1983).

[87] A. Polls, M. Radici, S. Boffi, W. Dickhoff, and H. Müther. *High-momentum proton removal from* ^{16}O *and the (e, e' p) cross section.* Phys. Rev. C **55**, 810 (1997).

[88] A. Ramos, A. Polls, and W. Dickhoff. *Single-particle properties and short-range correlations in nuclear matter.* Nucl. Phys. A **503**, 1 (1989).

[89] O. Benhar, A. Fabrocini, S. Fantoni, G. A. Miller, V. R. Pandharipande, and I. Sick. *Scattering of GeV electrons by nuclear matter.* Phys. Rev. C **44**, 2328 (1991).

[90] A. M. Ankowski, O. Benhar, and M. Sakuda. *Improving the accuracy of neutrino energy reconstruction in charged-current quasielastic scattering off nuclear targets.* Phys. Rev. D **91**, 033005 (2015).

[91] P. Barreau et al. *Deep-inelastic electron scattering from carbon.* Nucl. Phys. A **402**, 515 (1983).

[92] D. Baran et al. Δ *electroproduction and inelastic charge scattering from carbon and iron.* Phys. Rev. Lett. **61**, 400 (1988).

[93] R. Whitney, I. Sick, J. Ficenec, R. Kephart, and W. Trower. *Quasielastic electron scattering.* Phys. Rev. C **9**, 2230 (1974).

[94] O. Benhar. *Final-state interactions in the nuclear response at large momentum transfer.* Phys. Rev. C **87**, 024606 (2013).

[95] O. Benhar, A. Fabrocini, S. Fantoni, and I. Sick. *Spectral function of finite nuclei and scattering of GeV electrons.* Nucl. Phys. A **579**, 493 (1994).

[96] F. Coppini and O. Benhar. *Electron Scattering off Proton and Deuteron in the Resonace Production and Deep Inelastic Regions.* In preparation.

[97] K. Abe et al. (T2K Collaboration). *The T2K Experiment.* Nucl. Instrum. Meth. A **659**, 106 (2011).

[98] A. A. Aguilar-Arevalo et al. (MiniBooNE Collaboration). *The MiniBooNE Detector.* Nucl. Instrum. Meth. A **599**, 28 (2009).

[99] D. G. Michael et al. (MINOS Collaboration). *The Magnetized steel and scintillator calorimeters of the MINOS experiment.* Nucl. Instrum. Meth. **A596**, 190 (2008).

[100] D. S. Ayres et al. (NOvA Collaboration). *NOvA: Proposal to build a 30 kiloton off-axis detector to study* $\nu_\mu \to \nu_e$ *oscillations in the NuMI beamline.* hep-ex/0503053 (2004).

[101] C. Andreopoulos et al. *The GENIE Neutrino Monte Carlo Generator.* Nucl. Instrum. Meth. A **614**, 87 (2010).

[102] T. Leitner and U. Mosel. *Neutrino-nucleus scattering reexamined: Quasielastic scattering and pion production entanglement and implications for neutrino energy reconstruction.* Phys. Rev. C **81**, 064614 (2010).

[103] V. Lyubushkin et al. (NOMAD Collaboration). *A Study of quasi-elastic muon neutrino and antineutrino scattering in the NOMAD experiment.* Eur. Phys. J. C **63**, 355 (2009).

[104] S. Dytman. *Monte Carlo event generators.* AIP Conf. Proc. **1382**, 156 (2011).

[105] P. Coloma and P. Huber. *Impact of nuclear effects on the extraction of neutrino oscillation parameters.* Phys. Rev. Lett. **111**, 221802 (2013).

[106] C. M. Jen, A. Ankowski, O. Benhar, A. P. Furmanski, L. N. Kalousis, and C. Mariani. *Numerical Implementation of lepton-nucleus interactions and its effect on neutrino oscillation analysis.* Phys. Rev. D **90**, 093004 (2014).

[107] D. Rein and L. M. Sehgal. *Neutrino-excitation of baryon resonances and single pion production.* Annals of Physics **133**, 79 (1981).

[108] A. Bodek and U. Yang. *Higher twist, ξ_w scaling, and effective LO PDFs for lepton scattering in the few GeV region.* J. Phys. G **29**, 1899 (2003).

[109] T. Katori. *Meson Exchange Current (MEC) Models in Neutrino Interaction Generators.* AIP Conf. Proc. **1663**, 030001 (2015).

[110] J. W. Lightbody Jr. and J. S. O'Connell. *Modeling single arm electron scattering and nucleon production from nuclei by GeV electrons.* Comput. Phys. **2**, 57 (1988).

[111] K. Abe et al. (T2K Collaboration). *Measurement of the inclusive ν_μ charged current cross section on iron and hydrocarbon in the T2K on-axis neutrino beam.* Phys. Rev. D **90**, 052010 (2014).

[112] V. Lyubushkin et al. *A study of quasi-elastic muon neutrino and antineutrino scattering in the NOMAD experiment.* Eur. Phys. J. C **63**, 355 (2009).

[113] V. Barger et al. *Report of the US long baseline neutrino experiment study.* `arXiv:0705.4396` (2007).

[114] B. Eberly (MINERvA Collaboration). *Muon Neutrino Charged Current Inclusive Charged Pion ($CC\pi^{\pm}$) Production in MINERvA.* AIP Conf. Proc. **1663**, 070006 (2015).

[115] S. Short (Imperial College London). *Study of neutrino-induced neutral current neutral pion production in the T2K near detector.* Ph.D. Thesis (2013).

[116] L. Aliaga et al. (MINERvA Collaboration). *Design, Calibration, and Performance of the MINERvA Detector.* Nucl. Instrum. Meth. A **743**, 130 (2014).

[117] A. A. Aguilar-Arevalo et al. (MiniBooNE Collaboration). *Search for Electron Neutrino Appearance at the $\Delta m^2 \sim 1$ eV^2 Scale.* Phys. Rev. Lett. **98**, 231801 (2007).

[118] A. M. Ankowski, O. Benhar, P. Coloma, P. Huber, C.-M. Jen, C. Mariani, D. Meloni, and E. Vagnoni. *Comparison of the calorimetric and kinematic methods of neutrino energy reconstruction in disappearance experiments.* Phys. Rev. D **92**, 073014 (2015).

[119] Website: http://chimera.roma1.infn.it/OMAR/Erica/.

[120] C. Adams et al. (LBNE Collaboration). *The Long-Baseline Neutrino Experiment: Exploring Fundamental Symmetries of the Universe.* `arXiv:1307.7335` (2013).

[121] S. K. Agarwalla, S. Prakash, S. K. Raut, and S. U. Sankar. *Potential of optimized NOvA for large θ_{13} & combined performance with a LArTPC & T2K.* JHEP **12**, 075 (2012).

[122] S. K. Agarwalla, S. Prakash, and W. Wang. *High-precision measurement of atmospheric mass-squared splitting with T2K and NOvA.* `arXiv:1312.1477` (2013).

[123] S. K. Agarwalla, T. Li, and A. Rubbia. *An Incremental approach to unravel the neutrino mass hierarchy and CP violation with a long-baseline Superbeam for large θ_{13}.* JHEP **05**, 154 (2012).

[124] A. M. Ankowski, P. Coloma, P. Huber, C. Mariani, and E. Vagnoni. *Missing energy and the measurement of the CP-violating phase in neutrino oscillations.* Phys. Rev. D **92**, 091301 (2015).

[125] A. M. Ankowski, O. Benhar, C. Mariani, and E. Vagnoni. *Effect of the 2p2h cross-section uncertainties on an analysis of neutrino oscillations.* Phys. Rev. D **93**, 113004 (2016).

[126] P. Huber, M. Lindner, and W. Winter. *Simulation of long-baseline neutrino oscillation experiments with GLoBES (General Long Baseline Experiment Simulator).* Comput. Phys. Commun. **167**, 195 (2005).

[127] P. Huber, J. Kopp, M. Lindner, M. Rolinec, and W. Winter. *New features in the simulation of neutrino oscillation experiments with GLoBES 3.0: General Long Baseline Experiment Simulator.* Comput. Phys. Commun. **177**, 432 (2007).

[128] P. Coloma, P. Huber, J. Kopp, and W. Winter. *Systematic uncertainties in long-baseline neutrino oscillations for large θ_{13}.* Phys. Rev. D **87**, 033004 (2013).

[129] A. M. Dziewonski and D. L. Anderson. *Preliminary reference earth model.* Physics of the earth and planetary interiors **25**, 297 (1981).

[130] P. Coloma, P. Huber, C.-M. Jen, and C. Mariani. *Neutrino-nucleus interaction models and their impact on oscillation analyses.* Phys. Rev. D **89**, 073015 (2014).

[131] Letter of Intent Submitted to the Fermilab PAC P-1062 `https://indico.fnal.gov/getFile.py/access?resId=0&materialId=0&confId=9214`.

[132] V. Barger et al. *Report of the US long baseline neutrino experiment study.* `arXiv:0705.4396` (2007).

[133] A. Stahl et al. *Expression of Interest for a very Long Baseline Neutrino Oscillation experiment (LBNO).* CERN-SPSC-2012-021 (2012).

[134] L. A. Ahrens et al. *Determination of the Neutrino Fluxes in the Brookhaven Wide Band Beams.* Phys. Rev. D **34**, 75 (1986).

[135] S. Boyd, S. Dytman, E. Hernandez, J. Sobczyk, and R. Tacik. *Comparison of models of neutrino-nucleus interactions.* AIP Conf. Proc. **1189**, 60 (2009).

[136] O. Benhar, A. Lovato, and N. Rocco. *Contribution of two particle-two hole final states to the nuclear response.* Phys. Rev. C **92**, 024602 (2015).

[137] R. Gran et al. (K2K Collaboration). *Measurement of the quasi-elastic axial vector mass in neutrino-oxygen interactions.* Phys. Rev. D **74**, 052002 (2006).

[138] C. Mariani (K2K Collaboration). *K2K recent results.* AIP Conf. Proc. **981**, 247 (2008).

[139] K. Abe et al. (T2K Collaboration). *Measurement of the ν_μ charged-current quasielastic cross section on carbon with the ND280 detector at T2K.* Phys. Rev. D **92**, 112003 (2015).

[140] V. Bernard, L. Elouadrhiri, and U.-G. Meissner. *Axial structure of the nucleon: Topical Review.* J. Phys. G **28**, R1 (2002).

[141] P. Huber, M. Lindner, T. Schwetz, and W. Winter. *First hint for CP violation in neutrino oscillations from upcoming superbeam and reactor experiments.* J. High Energy Phys. **11**, 044 (2009).

[142] L. Fields et al. (MINERvA Collaboration). *Measurement of Muon Antineutrino Quasielastic Scattering on a Hydrocarbon Target at $E_\nu \sim 3.5$ GeV.* Phys. Rev. Lett. **111**, 022501 (2013).

[143] K. Abe et al. (T2K Collaboration). *Measurement of the ν_μ charged current quasielastic cross section on carbon with the T2K on-axis neutrino beam.* Phys. Rev. D **91**, 112002 (2015).

[144] K. Abe et al. (Hyper-Kamiokande Proto-Collaboration). *Physics potential of a long-baseline neutrino oscillation experiment using a J-PARC neutrino beam and Hyper-Kamiokande.* Prog. Theor. Exp. Phys. **2015**, 053C02 (2015).

[145] M. Martini, M. Ericson, G. Chanfray, and J. Marteau. *A Unified approach for nucleon knock-out, coherent and incoherent pion production in neutrino interactions with nuclei.* Phys. Rev. C **80**, 065501 (2009).

[146] M. Martini, M. Ericson, G. Chanfray, and J. Marteau. *Neutrino and antineutrino quasielastic interactions with nuclei.* Phys. Rev. C **81**, 045502 (2010).

[147] M. Martini, M. Ericson, and G. Chanfray. *Neutrino quasielastic interaction and nuclear dynamics.* Phys. Rev. C **84**, 055502 (2011).

[148] M. Martini and M. Ericson. *Quasielastic and multinucleon excitations in antineutrino-nucleus interactions.* Phys. Rev. C **87**, 065501 (2013).

[149] W. M. Alberico, M. Ericson, and A. Molinari. *The Role of Two Particles - Two Holes Excitations in the Spin - Isospin Nuclear Response.* Annals Phys. **154**, 356 (1984).

[150] J. Nieves, I. Ruiz Simo, and M. J. Vicente Vacas. *Inclusive Charged–Current Neutrino–Nucleus Reactions.* Phys. Rev. C **83**, 045501 (2011).

[151] J. Nieves, I. Ruiz Simo, and M. J. Vicente Vacas. *The nucleon axial mass and the MiniBooNE Quasielastic Neutrino-Nucleus Scattering problem.* Phys. Lett. B **707**, 72 (2012).

[152] J. Nieves, I. Ruiz Simo, and M. J. Vicente Vacas. *Two Particle-Hole Excitations in Charged Current Quasielastic Antineutrino–Nucleus Scattering.* Phys. Lett. B **721**, 90 (2013).

[153] R. Gran, J. Nieves, F. Sanchez, and M. J. Vicente Vacas. *Neutrino-nucleus quasi-elastic and 2p2h interactions up to 10 GeV.* Phys. Rev. D **88**, 113007 (2013).

[154] J. E. Amaro, M. B. Barbaro, J. A. Caballero, T. W. Donnelly, and C. F. Williamson. *Meson-exchange currents and quasielastic neutrino cross sections in the SuperScaling Approximation model.* Phys. Lett. B **696**, 151 (2011).

[155] J. E. Amaro, M. B. Barbaro, J. A. Caballero, and T. W. Donnelly. *Meson-exchange currents and quasielastic antineutrino cross sections in the SuperScaling Approximation.* Phys. Rev. Lett. **108**, 152501 (2012).

[156] G. D. Megias, J. E. Amaro, M. B. Barbaro, J. A. Caballero, and T. W. Donnelly. *Neutrino and antineutrino CCQE scattering in the SuperScaling Approximation from MiniBooNE to NOMAD energies.* Phys. Lett. B **725**, 170 (2013).

[157] G. D. Megias et al. *Meson-exchange currents and quasielastic predictions for charged-current neutrino-^{12}C scattering in the superscaling approach.* Phys. Rev. D **91**, 073004 (2015).

[158] O. Lalakulich, K. Gallmeister, and U. Mosel. *Many-Body Interactions of Neutrinos with Nuclei - Observables.* Phys. Rev. C **86**, 014614 (2012).

[159] A. M. Ankowski. *Consistent analysis of neutral- and charged-current neutrino scattering off carbon.* Phys. Rev. C **86**, 024616 (2012).

[160] O. Benhar, P. Coletti, and D. Meloni. *Electroweak nuclear response in quasi-elastic regime.* Phys. Rev. Lett. **105**, 132301 (2010).

[161] N. Rocco, A. Lovato, and O. Benhar. *Unified description of electron-nucleus scattering within the spectral function formalism.* Phys. Rev. Lett. **116**, 192501 (2016).

[162] V. Shtabovenko, R. Mertig, and F. Orellana. *New developments in feyncalc 9.0.* Comput. Phys. Commun. **207**, 432 (2016).

[163] R. Mertig, M. Böhm, and A. Denner. *Feyn Calc - Computer-algebraic calculation of Feynman amplitudes.* Comput. Phys. Commun. **64**, 345 (1991).

[164] Wolfram Research, Inc., Mathematica, Version 10.0, Champaign, IL (2014).